acta mechanica et automatica

CONTENTS

COMBINED BENDING WITH TENSION OF ISOTROPIC PLATE WITH CRACK CONSIDERING CRACK BANKS CONTACT AND PLASTIC ZONES AT ITS TOPS

Heorgij SULYM[*], Viktor OPANASOVYCH[**], Mykola SLOBODIAN[**], Oksana BILASH[***]

[*]Department of Mechanics and Applied Computer Science Application, Faculty of Mechanical Engineering,
Bialystok University of Technology, ul. Wiejska 45 C, 15-351 Bialystok, Poland
[**]Faculty of Mechanics and Mathematics, Department of Mechanics, The Ivan Franko National University of Lviv,
Universytetska Street, 1, Lviv, 79000, Ukraine
[***]Faculty Training Specialists Battle (Operational) Software, Department of Engineering Mechanics (Weapons and Equipment of Military
Engineering Forces), Hetman Petro Sahaidachnyi National Army Academy, Heroes of Maidan Street, 32, Lviv, Ukraine

sulym@pb.edu.pl, viktor.opanasovych@lnu.edu.ua, slobkolia@gmail.com, oksana.opanasovych@gmail.com

Abstract: Stress-strain state of isotropic plate with rectilinear through-crack at combined action of bending and tension, realized by applying distributed forces and bending moments at infinity, the vectors of which are parallel and perpendicular to the crack, is investigated. Under the influence of the internal stress the crack faces contacts on area of constant width near the upper base of plate, and plastic zones forms in its tips. Using methods of the theory of complex variables, complex potentials plane problem of elasticity theory and the classical theory of plates bending, solving of the problem is reduced to the set of linear conjugation problems and their analytical solution is built in a class of functions of limited plastic zones in the crack tips. The conditions of existence of the solution of the problem in these terms are determined. Using Treska plasticity conditions in the form of surface layer or the plastic hinge, the length of plastic zone and crack opening displacement are found analytically. Their numerical analysis for various parameters of the problem is conducted.

Key words: Isotropic Plate, Bending, Tension, Crack, Treska Plasticity Conditions

1. INTRODUCTION

The problems of bending and tension of plates with cracks are very common. In the article of Chen et al. (2005) the problems of periodic system of cracks in an infinite plate are investigated. For solving of the problems singular integral equation is used. In the article of Shi (2015) a high-accurate solving procedure that describes the effect of interacting of double-periodic rectangular systems of cracks is proposed. The bending of a thin infinite plate with a linear crack and a rigid inclusion of random shape is analyzed in the work of Wang et al. (2000). The solution is obtained in integral form by using the Green function of a singular dislocation. In the work of Boukellif et al. (2014) the method for cracks detection in plates is presented. This method allows determining parameters of crack, such as length, location and angles relatively to a reference coordinate system as so as calculation of stress intensity factors (SIF).

In the article of Prawoto (2012) classical fracture mechanics approach is used for calculation of the plastic zones that appears near cracks in heterogeneous or composite materials. In research of Unger D.J. (2007) instead of Tresca plasticity theory the Dugdale model of plasticity is used for a static crack. In the work of García-Collado et al. (2017) a numerical analysis of influence of plasticity, caused by crack closure, that uses the method of crack propagation in combination with cyclic plasticity in the crack tip. The Reissner's problems of bend of plates with cracks are given in the works of Guimaraes et al. (2009), Samaan et al. (2015), Sulym et al. (2011).

Research of stress-strain state at biaxial bending or combined bending and tension of isotropic plate with through-crack considering crack faces contact both on the crack line and in the region of constant width near one of the basis of the plate, without considering the plastic zones in the crack tip are represented in the works of Shackyj et al. (1989, 1995, 2004a, 2004b), Slepyan et al. (1995), Papargyri-Pegiou et al. (1995), Opanasovych (2007, 2008), excluding papers of Alfavicka (2015) and Opanasovych et al. (2015), where such consideration is done. In this article is studied the case of combined bending and tension of isotropic plate with through crack, faces of which are in contact on the area of constant width under the action of distributed forces and bending moments, applied at infinity, the vectors of which, are parallel and perpendicular to the crack faces, and considering plastic zones in the crack tip, where Treska plasticity conditions in the form of surface layer or the plastic hinge are satisfied. Using the method of complex potentials the solving of the problem is reduced to linear conjugation problems and the explicit expressions for complex potentials of plane problem of elasticity theory and the classical theory of bending of plates in the class of functions of limited plastic zones at the crack tips are found. The length of the plastic zone and crack opening displacement is found analytically and its numerical analysis with various parameters is done. In the particular case the known results are obtained.

2. FORMULATION OF THE PROBLEM

Let us consider an infinite isotropic plate of thickness $2h$, weakened by rectilinear through-crack of length $2l$. Crack faces

Heorgij Sulym,, Viktor Opanasovych, Mykola Slobodian, Oksana Bilash
Combined Bending with Tension of Isotropic Plate with Crack Considering Crack Banks Contact and Plastic Zones at its Tops

DOI 10.2478/ama-2018-0014

and the front surface are free from external loads. At infinity the plate is subjected to bending moments M_x^∞, M_y^∞ and tension forces p and q, applied symmetrically to the crack (see Fig. 1). The crack faces under the action of external loads are in smooth contact on area of constant width h_1 near the upper base of the plate (Opanasovych et al., 2008) and in the tips of crack strip-like plastic zones are forming, where Treska plasticity conditions are satisfied in the form of surface layer or the plastic hinge (Kushnir et al., 2003, Kyrjan et al. 2007).

We now introduce a Cartesian coordinate system $Oxy\tilde{z}$ with the origin in the center of crack, so the middle surface of the plate coincides with Oxy coordinate plane and Ox axis coincides with the crack line. We denote the crack length with plastic zones of length b as $2d$, the crack contour as L, and plastic zones as L_1, so $\tilde{L} = L + L_1$.
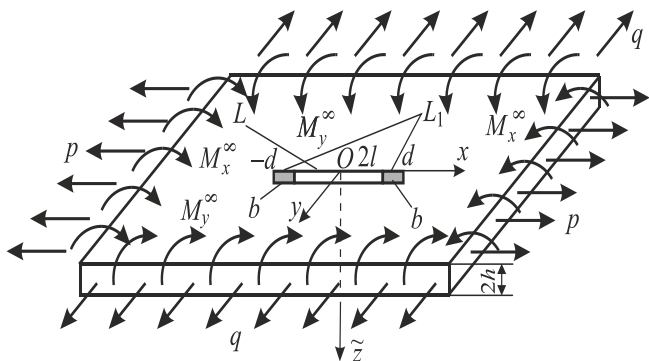

Fig. 1. Loading scheme of a plate and location of a crack with plastic zones

Since the crack faces are in contact, the solution of the problem can be divided into two: the plane problem of elasticity theory with unknown normal stresses, applied to crack faces, and the problem of bend with unknown bending moments applied to crack faces. In case of plane problem the constant normal stress σ_0 is acting in the plastic zones and in case of the problem of bend bending moment M_0 is acting. To describe bend we use the technical theory of bend of plates. For the crack faces in the plastic zones we have following boundary conditions:

$$\sigma_{yy}^\pm = \sigma_{yy}, \sigma_{xy}^\pm = 0, x \in L, \tag{1}$$

$$M_y^\pm = M_y, P_{yy}^\pm = 0, x \in L, \tag{2}$$

$$M_y = \beta N, \partial_x[v] + \alpha[\partial_{xy}^2 w] = 0, x \in L, \tag{3}$$

$$\sigma_{yy}^\pm = \sigma_0, \sigma_{xy}^\pm = 0, x \in L_1, \tag{4}$$

$$M_y^\pm = M_0, P_y^\pm = 0, x \in L_1, \tag{5}$$

where: $N = -2h\sigma_{yy}$, $N -$ crack faces contact force ($N > 0$); $\sigma_{yy}, \sigma_{xy} -$ stress tensor components; $u,v -$ displacement vector components at the plane problem (Musheviashvili, 1966); $P_y -$ generalized Kirchhoff cross-force; $M_y -$ bending moment; $w -$ deflection of the plate (Prusov, 1975); in the second formula (3) we introduce the notation $[\rho(x)] = \rho^+(x) - \rho^-(x)$, "+" and "−" signs correspond to limit value of an appropriate value at $y \to \pm 0$; $[f] = f^+ - f^-$; α and $\beta -$ constant, which are determined by the formula (Opanasovych, 2007):

$$\beta = 1 - \gamma/3, \alpha = 0.5[1 + (1-\gamma)^2], \gamma = h_1/h. \tag{6}$$

3. CONSTRUCTION OF THE SOLUTION OF THE PROBLEM

Let us introduce the complex potentials $\Phi(z)$ and $\Omega(z)$ (Musheviashvili, 1966) for plane problem and $\Phi_*(z)$ and $\Omega_*(z)$ (Prusov, 1975) – for bend, and then use the dependencies

$$\sigma_{yy} - i\sigma_{xy} = \Phi(z) + \Omega(\bar{z}) + (z - \bar{z})\overline{\Phi'(z)},$$

$$2\mu\partial_x(u + iv) = \kappa\Phi(z) - \Omega(\bar{z}) - (z - \bar{z})\overline{\Phi'(z)}, \tag{7}$$

$$\partial_x g = \Phi_*(z) - \Omega_*(\bar{z}) + (z - \bar{z})\overline{\Phi_*'(z)},$$

$$f = \tilde{\kappa}\Phi_*(z) + \Omega_*(\bar{z}) - (z - \bar{z})\overline{\Phi_*'(z)}. \tag{8}$$

where: $\mu = E[2(1 + \upsilon)]^{-1} -$ shear module, $E -$ Young's module, $\upsilon -$ Poisson's ratio of the material of the plate, $i = \sqrt{-1}$, $\kappa = (3 - \upsilon)/(1 + \upsilon)$, $\tilde{\kappa} = (3 + \upsilon)/(1 - \upsilon)$, $z = x + iy$, $g = \partial_x w + i \partial_y w$, $f = (M_y + ic' + i\int_0^x P(\varepsilon)d\varepsilon)/m$, $m = -D(1 - \upsilon)$, $c' -$ unknown real constant, $D = \frac{2Eh^3}{3(1-\upsilon^2)} -$ cylindrical rigidity of plate.

Complex potential for large $|z|$ can be represented as (Musheviashvili, 1966, Prusov, 1975):

$$\Phi(z) = \Gamma + O(1/z^2), \Omega(z) = \Gamma + \Gamma' + O(1/z^2),$$

$$\Phi_*(z) = \tilde{\Gamma} + O(1/z^2), \Omega_*(z) = -\tilde{\Gamma} - \tilde{\Gamma}' + O(1/z^2), \tag{9}$$

where: $\Gamma = \frac{1}{4}(q + p), \Gamma' = \frac{1}{2}(q - p), \tilde{\Gamma} = -\frac{M_x^\infty + M_y^\infty}{4D(1+\upsilon)}$, $\tilde{\Gamma}' = -\frac{M_y^\infty - M_x^\infty}{2m}$.

From boundary conditions (1), (2), (4), (5) and the first equation (7) and the second (8), we will get:

$$(\sigma_{yy} - i\sigma_{xy})^+ - (\sigma_{yy} - i\sigma_{xy})^- == (\Phi(x) - \Omega(x))^+ - (\Phi(x) - \Omega(x))^- = 0, x \in \tilde{L}, \tag{10}$$

$$f^+(x) - f^-(x) = (\tilde{\kappa}\Phi_*(x) - \Omega_*(x))^+ - (\tilde{\kappa}\Phi_*(x) - \Omega_*(x))^- = 0.$$

By solving the linear conjugation (10) and considering the expression (9), we will have:

$$\Omega(z) = \Phi(z) + \Gamma', \Omega_*(z) = \tilde{\kappa}\Phi_*(z) - (\tilde{\kappa} + 1)\tilde{\Gamma} - \tilde{\Gamma}', \tag{11}$$

If we introduce the function:

$$F(z) = -2\beta h^2\Phi(z) - m\tilde{\kappa}\Phi_*(z) - \beta h^2\Gamma' + + \frac{1}{2}\{ic' + m[(\tilde{\kappa} + 1)\tilde{\Gamma} - \tilde{\Gamma}']\}, \tag{12}$$

then, as can be seen from the first condition (3) and (5), considering the first expressions (7) and (8), and (11), it will satisfy the boundary conditions:

$$F^+(x) + F^-(x) = \begin{cases} \sigma_1, x \in L_1, \\ 0, x \in L, \end{cases} \tag{13}$$

where:

$$\sigma_1 = -2h^2\beta\sigma_0 - M_0. \tag{14}$$

Solution of the problem of linear conjugation (13) in the class of functions of limited plastic zones in the crack tips has the form:

$$F(z) = \frac{\sigma_1 X_1(z)}{2\pi i} \int_{L_1} \frac{dt}{X^+_1(t)(t-z)} =$$

$$= \frac{\sigma_1}{\pi i} \ln \frac{d\sqrt{l^2-z^2}}{z\sqrt{d^2-l^2}+l\sqrt{d^2-z^2}} \tag{15}$$

where:

$$X_1(z) = \sqrt{z^2 - d^2}.$$

Taking into account (9), for a function $F(z)$ (12) at large $|z|$ we will have the expansion:

$$F(z) = \frac{1}{2}(ic' - M_y^\infty) - \beta h^2 q + O\left(\frac{1}{z^2}\right). \tag{16}$$

Having converted the right part of (15) into a series at large $|z|$ and taking into account (16), we will get:

$$c' = 0, \tag{17}$$

$$-\frac{(M_y^\infty + 2\beta h^2 q)}{2\sigma_1} = \arccos \frac{l}{d}. \tag{18}$$

From dependence (18) we determine length of the plastic zone b.

From boundary conditions:

$$\sigma_{xy}^+ + \sigma_{xy}^- = 0, P^+ + P^- = 0, x \in \tilde{L},$$

considering (7), (8), (11), (17), we obtain a problem of linear conjugation:

$$\left(\Phi(x) - \bar{\Phi}(x)\right)^+ + \left(\Phi(x) - \bar{\Phi}(x)\right)^- = 0, x \in \tilde{L},$$

$$\left(\Phi_*(x) - \bar{\Phi}_*(x)\right)^+ + \left(\Phi_*(x) - \bar{\Phi}_*(x)\right)^- = 0, x \in \tilde{L},$$

solving which in the class of functions of limited plastic zones at the crack tips, we will get:

$$\bar{\Phi}(z) = \Phi(z), \Phi_*(z) = \bar{\Phi}_*(z), \tag{19}$$

Considering (8), (11), (17), (19), the second condition (3) and the first condition (4) and (5), will have

$$\left(\delta\Phi(x) + 2\Phi_*(x) - \frac{A}{2}\right)^+ - \left(\delta\Phi(x) + 2\Phi_*(x) - \frac{A}{2}\right)^-$$

$$= 0, x \in L, \left(\delta\Phi(x) + 2\Phi_*(x) - \frac{A}{2}\right)^+ +$$

$$+ \left(\delta\Phi(x) + 2\Phi_*(x) - \frac{A}{2}\right)^- = 0, x \in L_1, \tag{20}$$

where:

$$A = \delta\sigma_0 - \delta\Gamma' + 2\tilde{\kappa}^{-1}\left(M_0 m^{-1} + (\tilde{\kappa}+1)\tilde{\Gamma} + \tilde{\Gamma}'\right), \delta = \frac{2(1-\nu)}{E\alpha h}, \tag{21}$$

Having solved the problem of linear conjugation (20) in the class of functions limited plastic zones at the crack tips, we get:

$$\delta\Phi(z) + 2\Phi_*(z) - \frac{A}{2} = 0. \tag{22}$$

Taking into account the expansion (9), based on (22) we will have:

$$A = 2(\delta\Gamma + 2\tilde{\Gamma}), \tag{23}$$

or

$$-\frac{h^2}{3}\tilde{\gamma}\sigma_0 + 2M_0 = 2M_y^\infty - \frac{h^2}{3}\tilde{\gamma}q, \tag{24}$$

where: $\tilde{\gamma} = 4\gamma_1, \gamma_1 = 3 + \nu/(\alpha(1+\nu))$,

To find σ_0 and M_0 firstly let us use Treska plasticity condition in the form of surface layer on the bottom base of the plate (Kushnir et al., 2003, Kyrjan et al. 2007):

$$\sigma_0 + 3M_0/(2h^2) = \sigma_y, \tag{25}$$

where σ_y — yield stress of the material of the plate.

Having solved the system of equations (24) and (25) for σ_0 and M_0, we will get:

$$\tilde{\sigma}_0 = \sigma_0/\sigma_y = 4(1 + 0.25\tilde{\gamma}\tilde{q} - \tilde{\sigma})/(4+\tilde{\gamma}), \tag{26}$$

$$\widetilde{M}_0 = 3M_0/(2h^2\sigma_y) = \left(4\tilde{\sigma} + \tilde{\gamma}(1-\tilde{q})\right)/(4+\tilde{\gamma}),$$

where:

$$\tilde{\sigma} = \sigma_\infty/\sigma_y, \sigma_\infty = 3M_y^\infty/(2h^2), \tilde{q} = q/\sigma_y. \tag{27}$$

If we use plastic hinge condition (Kushnir et al., 2003, Kyrjan et al. 2007):

$$\left(\frac{\sigma_0}{\sigma_y}\right) + \frac{M_0}{h^2\sigma_y} = 1, \tag{28}$$

and solve the system of equations (24) and (28) for the same variables, we will get:

$$\tilde{\sigma}_0 = \sqrt{\left(\tilde{\gamma}/_{12}\right)^2 + 1 - 2\tilde{\sigma}/3 + \tilde{q}/6} - \tilde{\gamma}/_{12},$$

$$\widetilde{M}_0 = \tilde{\sigma} + 0.25(\tilde{\gamma}\tilde{\sigma}_0 - \tilde{q}). \tag{29}$$

If we solve the system of equations (12) and (22) for $\Phi(z)$ and $\Phi_*(z)$, then we will get:

$$\Phi(z) = C_5 + C_6 F(z), \Phi_*(z) = C_7 + C_8 F(z), \tag{30}$$

where:

$$C_5 = C_6(Am\tilde{\kappa} - 4B), C_6 = 2(\delta m\tilde{\kappa} - 4\beta h^2)^{-1}, C_7 = 0.5C_6(B\delta - A\beta h^2), C_8 = -0.5\delta C_6, B = -\beta h^2\Gamma' + m((\tilde{\kappa}+1)\tilde{\Gamma} + \tilde{\Gamma}')/2.$$

To determine the contact force N between the crack banks we take into account formulas (6), (7), (11) and (30). After the appropriate transformations we will get:

$$N = \frac{M_y^\infty - 2h^2 q\gamma_1/3}{h(\beta + \gamma_1/3)}. \tag{31}$$

As so as $N > 0$, such formulation of the problem exists when the following inequality is satisfied:

$$q \le \sigma_\infty/\gamma_1, \tag{32}$$

which takes place, as shown in publications of Opanasovych et al. (2008, 2015) in a case, when there are no plastic zones in the crack tips.

Crack opening displacement δ in the crack tips on the lower base of the plate we will find by the formula:

$$\delta = \int_d^l \partial_x \left([\upsilon] - h[\partial_y w]\right) \partial x. \tag{33}$$

If we take into account (7), (8), (11), (19), (30), then after transformations from (33) we will get:

$$\delta^* = \frac{\delta E}{\sigma_y l} = R\ln \frac{l}{d}, \tag{34}$$

where:

$$R = 32R_1(1 + \alpha)/\big(\pi\alpha(\tilde{\gamma} + 12\beta)\big) \; R_1 = \widetilde{M}_0 + 3\beta\tilde{\sigma}_0.$$

If we introduce the relative length of plastic zone as $\varepsilon = b/l$, then formulas (18) and (34) will take forms

$$\varepsilon = \sec\big(\pi(\tilde{\sigma} + 3\beta\tilde{q})/(2R_1)\big) - 1, \; \delta^* = R\ln(1 + \varepsilon).$$

Let us assume that parameter γ linearly depends on q, that means it changes according to the law

$$\gamma = \tilde{\gamma}_1(1 - \alpha\gamma_1\tilde{q}/\tilde{\sigma}),$$

where $\tilde{\gamma}_1$ is the width of crack banks contact area at $p = q = 0$ (Slepyan, 1995; Opanasovych, 2015).

It should be noted that for the case when we have only biaxial bending, i.e. $p = q = 0$, we will get the results obtained in the article (Opanasovych, 2015).

4. NUMERICAL ANALYSIS OF THE PROBLEM

Numerical analysis of the problem was conducted for $\upsilon = 0.3$ and $\tilde{\gamma}_1 = 0.13$, and is presented in Fig. 2 and Fig. 3, where the solid lines represent the results obtained at Treska plasticity conditions in the form of surface layer, and dash lines – obtained with the use of plastic hinge conditions.
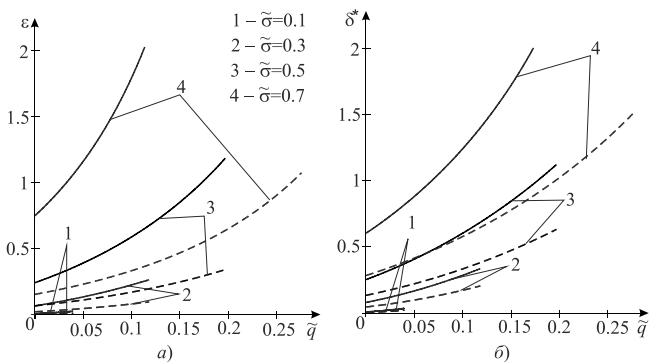

Fig. 2. Graphical dependences of relative length of plastic zone $\varepsilon = b/l$ and dimensionless crack opening displacement $\delta^* = E\delta/(\sigma_Y l)$ on $\tilde{q} = q/\sigma_Y$
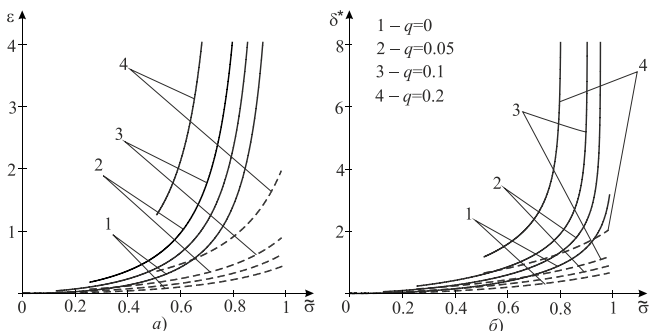

Fig. 3. Graphical dependences of relative length of plastic zone $\varepsilon = b/l$ and dimensionless crack opening displacement $\delta^* = E\delta/(\sigma_Y l)$ on $\tilde{\sigma} = \sigma_\infty/\sigma_Y$

On Fig. 2 the graphical dependences of relative length of plastic zone $\varepsilon = b/l$ (Fig. 2a) and dimensionless crack opening displacement $\delta^* = E\delta/(\sigma_Y l)$ (Fig. 2 b) on $\tilde{q} = q/\sigma_Y$ are built.

Curve 1 is built at $\tilde{\sigma} = \sigma_\infty/\sigma_Y = 0.1$ ($0 \le \tilde{q} \le 0.0394$), curve 2 – at $\tilde{\sigma} = 0.3$ ($0 \le \tilde{q} \le 0.1182$), curve 3 – at $\tilde{\sigma} = 0.5$ ($0 \le \tilde{q} \le 0.197$), curve 4 – at $\tilde{\sigma} = 0.7$ ($0 \le \tilde{q} \le 0.2758$).

On Fig. 3 the graphical dependences of relative length of plastic zone $\varepsilon = b/l$ (Fig.3a) and dimensionless crack opening displacement $\delta^* = E\delta/(\sigma_Y l)$ (Fig.3 b) on $\tilde{\sigma} = \sigma_\infty/\sigma_Y$ are represented. Curve 1 is built at $\tilde{q} = q/\sigma_Y = 0$ ($0 \le \tilde{\sigma} \le 1$), curve 2 – at $\tilde{q} = 0.05$ ($0.1269 \le \tilde{\sigma} \le 1$), curve 3 – at $\tilde{q} = 0.1$ ($0.2538 \le \tilde{\sigma} \le 1$), curve 4 – at $\tilde{q} = 0.2$ ($0.5077 \le \tilde{\sigma} \le 1$).

5. CONCLUSIONS

From the figures we can see, that with the increase of the external loads $\tilde{q} = q/\sigma_Y$ and $\tilde{\sigma} = \sigma_\infty/\sigma_Y$ length of plastic zone in the crack tips and crack opening displacement increases. Also, this parameters, determined with the use of plasticity conditions in the form of surface layer, are higher than obtained by using plasticity condition in the form of plastic hinge. At $\tilde{\sigma} \to 1$ a significant increase ε and δ^* regardless on $\tilde{q}$, is observed in case of using Treska plasticity condition in the form of surface layer, and it is not observed in the case of plastic hinge conditions. Our research shows, that the distributed bending moment at infinity when its vector is perpendicular to the crack, as well as the distributed force at infinity, does not affect length of the plastic zones and crack opening displacement.

REFERENCES

1. **Alfavicka S.O.** (2015), Bend of a plate with a through straight crack with plastic zones in its tip taking into account the crack faces contact and cold-hardening of material, *Bulletin of Kyiv National Taras Shevchenko University*. Series Sci. Vol. Special, 21-26
2. **Boukellif R., Ricoeur A.** (2014), Parameter identification for cracks in elastic plate structures based on remote strain fields, *International Journal of Solids and Structures,* 51 (11–12), 2123-2132.
3. **Chen Y.Z., Lin X.Y.** (2005), Periodic group crack problems in an infinite plate, *International Journal of Solids and Structures*, 42 (9–10), 2837-2850.
4. **García-Collado A., Vasco-Olmo J.M., Díaz F.A.** (2017), Numerical analysis of plasticity induced crack closure based on an irreversible cohesive zone model, *Theoretical and Applied Fracture Mechanics*, 89, 52-62.
5. **Guimaraes S., Telles J.C.F.** (2009), The method of fundamental solutions for fracture mechanics — Reissner's *plate* application, *Engineering Analysis with Boundary Elements*, 33 (10), 1152-1160.
6. **Kushnir R.M., Nykolyshyn M.M., Osadchyk V.A.** (2003), Elastic and elastic-plastic boundary state of membranes with defects, SPOLOM, Lviv.
7. **Kyrjan V.I., Osadchuk V.A. Nykolyshyn M.M.** (2007), *Fracture mechanics of metal welded joints*, SPOLOM, Lviv.
8. **Musheviashvili N.I.** (1966), *Some basic problems of the mathematical elasticity theory*, Science, Moscow.
9. **Opanasovych V.K.** (2007), Bend of plates with a through rectilinear crack taking into account the width of crack faces contact area, *Scientific notes of the Lutsk Technical University: Interuniversity collection (on topic "Mechanical Engineering")*, 20(2), 123–127.
10. **Opanasovych V.K., Dorosh M.** (2008), Combined bend with tension of plates weakened by two collinear cracks with contact of their faces, *Bulletin of Lviv. Univ. Series meh.-mate*, 68, 194-206.
11. **Opanasovych V.K., Slobodjan M.S.** (2015), Biaxial bending of isotropic plate with a through linear crack considering the width of the crack faces contact area and the presence of plastic zones in its tips, *Mathematical methods and physico-mechanical fields*, 58(4), 128–135.

12. **Papargyri-Pegiou S., Theofanidis D., Webb T.W., Aifantis E.C.** (1995), A simple approach for modelling the heterogeneity of crack tip plastic zones, *Mechanics Research Communications,* 22(3), 263-269.

13. **Prawoto Y.** (2012), How to compute plastic zones of heterogeneous materials: A simple approach using classical continuum and fracture mechanics, *International Journal of Solids and Structures*, 49 (15–16), 2195-2201.

14. **Prusov I.A.** (1975), *The method of conjugation in the theory of plates*, Publication Belarusian, University, Minsk.

15. **Samaan M.F., Nassar M.E., Rashed Y.F.** (2015), Taylor series fast multipole boundary element method for solution of Reissner's shear deformable plate bending problems, *Engineering Analysis* with *Boundary Elements*, 59, 23-35.

16. **Shackyj I.P.** (1989), On the contact of notch faces in plate at combined tension with bending, *Physico-chemical Mechanics of materials*, 25(2), 46-50.

17. **Shackyj I.P.** (1995), Boundary-equilibrium state of plates with collinear cracks at combined tension and bending, *Reports of the NAS of Ukraine*, 10, 62-64.

18. **Shackyj I.P., Makovijchuk M.V.** (2004), Interaction of cracks faces at the combined tension with bending of plate on elastic base, *Mashinoznavstvo*, 10, 62-68.

19. **Shackyj I.P., Perepichka V.V.** (2004), Boundary state of semi-infinite plate with edge crack at bend with tension, *Physico-chemical Mechanics of materials*, 40(2), 73-77.

20. **Shi P.P.** (2015), On the plastic zone size of solids containing doubly periodic rectangular-shaped arrays of cracks under longitudinal shear, *Mechanics Research Communications*, 67, 39-46.

21. **Slepyan L.I. Dempsey J.P., Shekhtman I.I.** (1995), Asymptotic solutions for crack closure in an elastic plate under combined extension and bending, *Journal of the Mechanics and Physics of Solids.* 43, 1727-1749.

22. **Sulym H., Opanasowych W., Jacyk I.** (2011), Bending of Reissner's plate containing cracks with the account of their faces contact zone width, *Acta Mechanica et Automatica*, 5(1), 85-93.

23. **Unger D.J.** (2007), Numerical plane stress elastic–perfectly plastic crack analysis under Tresca yield condition with comparison to Dugdale plastic strip model, *Mechanics Research Communications*, 34(4), 325-330.

24. **Wang X.-F., Hasebe N.** (2000), Bending of a thin plate containing a rigid inclusion and a crack, *Engineering Analysis with Boundary Elements*, 24(2), 145-153.

MAGNETORHEOLOGICAL SELF-POWERED VIBRATION REDUCTION SYSTEM WITH CURRENT CUT-OFF: EXPERIMENTAL INVESTIGATION

Łukasz JASTRZĘBSKI*, Bogdan SAPIŃSKI*

*AGH University of Science and Technology, Mechanical Engineering and Robotics, Department of Process Control,
Al. Adama Mickiewicza 30, 30-059 Kraków, Poland

lukasz.jastrzebski83@gmail.com, deep@agh.edu.pl

Abstract: The paper summarises the results of laboratory testing of an energy harvesting vibration reduction system based on a magnetorheological (MR) damper whose control circuit incorporates a battery of bipolar electrolytic capacitors (current cut-off circuit). It is designed to reduce the undesired effects in vibration reduction systems of this type, associated with the increasing amplitude of the sprung mass vibration under the excitation inputs whose frequency should exceed the resonance frequency of the entire system. Results have demonstrated that incorporating a current cut-off circuit results in a significant decrease of sprung mass vibration amplitudes when the frequency of acting excitation inputs is higher than the resonance frequency.

Key words: MR Damper, Vibration, Energy Harvesting, Current Cut-Off Circuit

1. INTRODUCTION

One of the first studies on MR-damper based vibration reduction systems with energy harvesting capability was the work (Choi et al., 2007) investigating the performance of an electromagnetic energy harvester converting the energy of vibration into electric power supplying the control coil in an MR damper. The harvester was able to generate sufficiently high energy to power-supply the RD-1097-01 damper (Lord Co) in the analysed system. Further works provide information about other design versions of electromagnetic harvesters, methods of their integration with MR dampers and suggested implementations in vibration reduction systems. For example, Chen and Liao (2012) presents theoretical and experimental studies of an MR damper prototype which had self-powered and self-sensing capabilities. The work (Choi and Werely, 2009) investigates experimentally a smart passive control system comprising an MR damper and an electromagnetic induction device to generate electrical power. The studies: Sapiński, (2008) and Sapiński (2010) concern design considerations, calculations of magnetic field and experimental tests of the electromagnetic induction devices, that could be integrated with an MR damper. The reports (Wang et al., 2009) and (Wang and Bai, 2013) demonstrate the idea of an integrated relative displacement self-sensing MR damper and also designing, fabrication and experimental testing of its prototype. The study (Xinchun et al., 2015) presents a novel self-powered MR damper focusing on its theoretical and experimental analysis. The work (Zhu et al., 2012) describes self-powered and sensor-based MR damper systems and its usefulness in large-scale civil constructions where the power supply is impractical.

It is worthwhile to mention that such harvesters can act not only as power generators, but as velocity sensors as well. A comprehensive review of literature on the subject of energy harvesting and recent advancements in MR dampers is provided in Ahmed et al. (2016).

Research data demonstrate that MR damper-based vibration reduction systems with energy harvesting capability are able to effectively reduce the amplitude of the sprung mass vibration in the neighbourhood of the resonance frequency. However, because the harvester and a MR damper are connected in between the sprung mass and the source of vibration, the amplitude of the sprung mass vibrations will significantly increase when the excitation frequency becomes higher than the resonance frequency of the system (Sapiński, 2011; Sapiński et al., 2011). This undesired effect is attributed to the increased amount of energy generated by the harvester (increasing the relative velocity), hence the amount of energy supplied to power the MR damper control coil has to rise, which in consequence leads to an increase of dissipated energy. This problem can be overcome by incorporating a passive (Jastrzębski and Sapiński, 2016) or controlled electric circuit connected in between the harvester coil and the MR damper control coil (Sapiński et al., 2011; 2016).
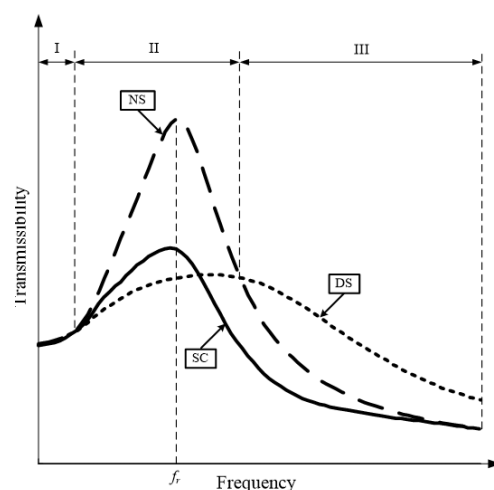

Fig. 1. Frequency response of the vibration reduction system

Fig. 1 shows vibration transmissibility of a 1 DOF system, for three variants of the damper coil supply type (NS – no power supply, DS – directly supplied from the harvester, SC – supplied from the harvester via a battery of capacitors. Three characteristics frequency ranges are designated as I, II, III.

In the low frequency range I ($f \ll f_r$), vibration amplitudes are similar in all three investigated cases. In the frequency range II ($f \approx f_r$) in the DS case the vibration amplitude tends to decrease in relation to that registered in the NS case. In the frequency range III ($f \gg f_r$) the amplitude of vibrations in the case DS increases when compared to NS. This undesired effect is not observed in the SC case.

It is suggested, therefore, that a battery of capacitors comprising a current cut-off circuit should be connected in between the harvester coil and the MR damper coil. Consequently, at frequencies in excess of f_r, the current in the damper coil will be cut–off, thus enabling the amplitudes of the sprung mass vibrations to be effectively reduced.

2. CURRENT CUT-OFF CIRCUIT

Fig. 2 shows the schematic diagram of the electric circuit comprising the harvester coil (R_h, L_h), capacitor batteries (C_1, ..., C_n) and the damper coil (R_d, L_d). It is worthwhile to mention that at frequency $f \ll f_r$, reactance of the condenser battery $X_c \rightarrow \infty$, hence $i_h \approx i_d$. At frequency $f \gg f_r$, reactance $X_c \rightarrow 0$ and hence the current $i_d \rightarrow 0$ ($i_h \approx i_c$). Accordingly, the capacitance of the capacitors' battery has to be precisely controlled in relation to the resonance frequency f_r. Thus, the effects of the capacitors' capacitance on frequency characteristics of the current cut-off circuit and the vibration reduction system are analysed and comparison is made of the system's performance in the NS, DS, SC cases. The battery comprised 2, 4, 6, 8 capacitors connected in parallel, each having the capacitance 4700 µF and voltage rating 35 V, the total capacitance of the battery being 9.4 mF (variant SC1), 18.8 mF (variant SC2), 28.2 mF (variant SC3) and 37.6 mF (variant SC4).
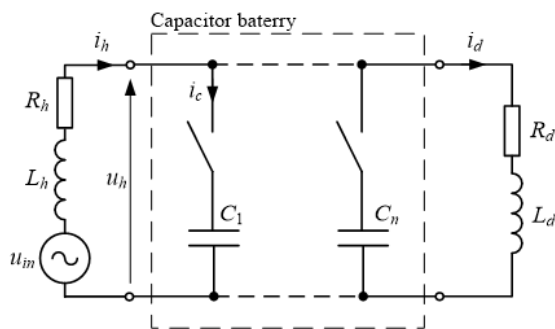

Fig. 2. Schematic of the electric circuit: harvester coil, capacitors, damper coil

In the first stage the relationship was established between the impedance of the system and frequency, and the effectiveness of current cut-off in the damper coil was investigated. The diagram of the measurement system is shown in Fig. 3 The hardware includes a power supply, a power amplifier (based on an operational amplifier OPA549 and integrated circuits for output current and voltage measurements), a PC with an AD/DA card and current-to-voltage converters. The software is supported by the MATLAB/Simulink environment. The excitation signal applied was a sinusoidal current i_h with amplitude 0.5 A and frequency f from the range 0.1 – 10 Hz, varied with the step 0.1 Hz (current mode of the amplifier operation).
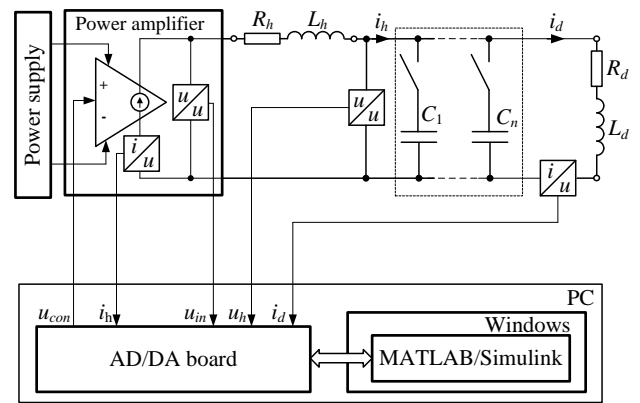
Fig. 3. Diagram of the measurement system for current cut-off circuit

Fig. 4 – 6 summarise the test results presented as impedance vs frequency plots. The modulus of total impedance of the system $\left|Z_c\right|$ (see Fig. 2) is derived from formulas (1), likewise the impedance $\left|Z\right|$ is expressed as U_h/I_h.

$$|Z_c| = \frac{U_{in}}{I_h} = \frac{\sqrt{\frac{1}{T}\int_t^{t+T} u_{in}(t)^2 dt}}{\sqrt{\frac{1}{T}\int_t^{t+T} i_h(t)^2 dt}} \tag{1}$$

Fig. 4. Module of total impedance |Zc| vs. frequency f

Fig. 5. Module of impedance |Z| vs. frequency f

Łukasz Jastrzębski, Bogdan Sapiński
Magnetorheological Self-Powered Vibration Reduction System with Current Cut-Off: Experimental Investigation

DOI 10.2478/ama-2018-0015

Fig. 6. Current ratio I_d/I_h vs. frequency f

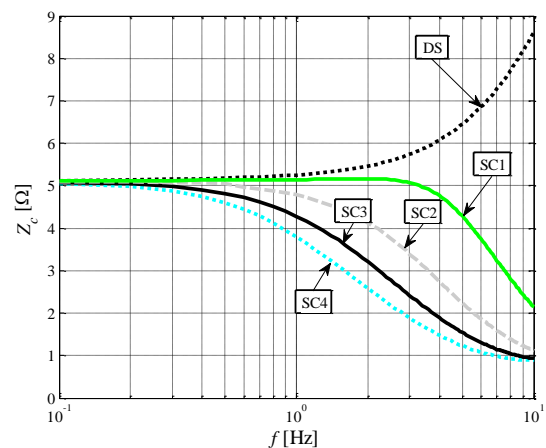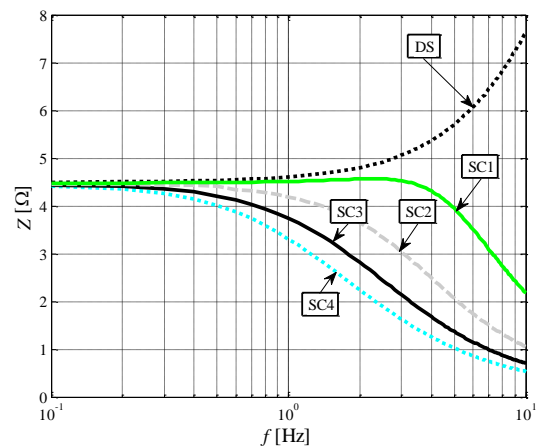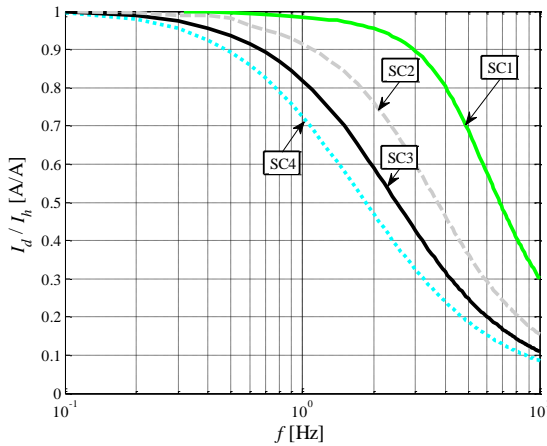It appears that at frequency f=0.1 Hz, the difference between $|Z_c|$ and $|Z|$ is equal to the internal impedance of the harvester, which is 0.65 Ω (compare Figs. 4 and 5). In the case DS, an increase in frequency gives rise to increase of both $|Z_c|$ and $|Z|$, which is revealed when f >1 Hz (the circuit behaviour becomes resistive and inductive). In the case SC a reverse effect is observed, i.e. $|Z_c|$ and $|Z|$ tend to decrease whilst the circuit behaves like a resistive-capacitive one. The impedance modulus $|Z_c|$ decreases √2- fold, respectively at f >6.4 Hz (SC1), f >2.8 Hz (SC2), f > 1.7 Hz (SC3) and f >1.2 Hz. At frequency f=0.1 Hz, I_h=I_d, due to a large impedance of capacitors (see Fig. 6). When frequency f increases, the current in capacitors increases too because their impedance will go down, causing the current I_d in the damper coil to decrease (current cut-off). Current I_d is √2- fold lower than I_h at frequencies f > 4.8 Hz (SC1), f >2.3 Hz (SC2), f >1.5 Hz (SC3), f >1.1 Hz (SC4).

3. MR SELF-POWERED VIBRATION REDUCTION SYSTEM WITH CURRENT CUT-OFF

The current cut-off circuit outlined in the previous section has been implemented in a MR damper-based vibration reduction system with energy harvesting capability (1 DOF system). Tests were performed to investigate how the capacitors' capacitance should affect the frequency characteristics of the system. Thus obtained results were compared with those obtained when investigating NS and DS cases.

The experimental set-up (Fig. 7) described in more detail in Sapiński et al. (2010) consisted of the electro-dynamic shaker (model V780 manufactured by the LDS Company), a mobile platform (sprung mass) with the mass 100 kg, a vibration reduction system (electromagnetic harvester (Sapiński, 2010) and a Lord Co. RD-1005-3 series MR damper), a spring with the stiffness coefficient k=105 N/m and sensors S_1-S_3. The sprung mass, damper, a harvester and springs comprise a 1 DOF system whose natural frequency equals f_0=5 Hz. Displacements of the shaker core $z(t)$ and of the platform $x(t)$ were measured with laser sensors (S_1, S_2). Measurements of the damper force F_d (S_3) were taken with a force sensor. Current levels in the harvester coil i_h and in the damper coil i_d were measured using current-to-voltage converters.

Experiments were conducted under the applied sine excitations $z(t)$ with the amplitude 3.5 mm and frequency varied in the range

2 – 10 Hz, with the step 0.1 Hz. Measurements signals were registered within the time period 20 s, the sampling frequency being 1 kHz.

Figs 8–13 show the frequency characteristics obtained in the NS, DS, SC cases. The displacement transmissibility coefficient T_{xz} is derived from formula (2). Frequency characteristics provided in further sections involve the rms values of investigated quantities.
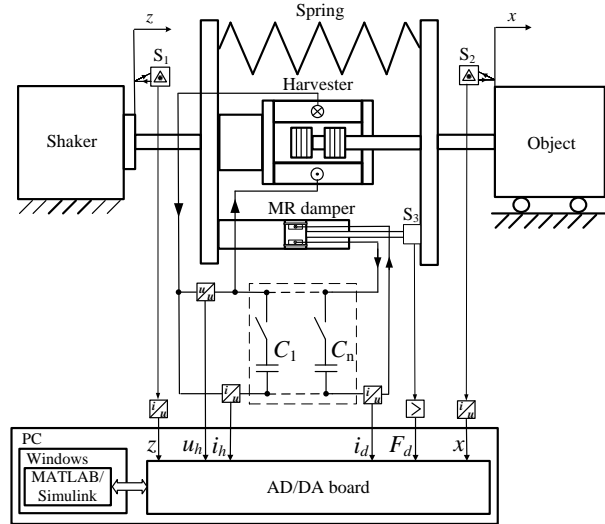
Fig. 7. Schematic diagram of the experimental set-up

$$T_{xz} = \frac{X}{Z} = \frac{\sqrt{\frac{1}{T}\int_t^{t+T} x(t)^2 dt}}{\sqrt{\frac{1}{T}\int_t^{t+T} z(t)^2 dt}} \tag{2}$$
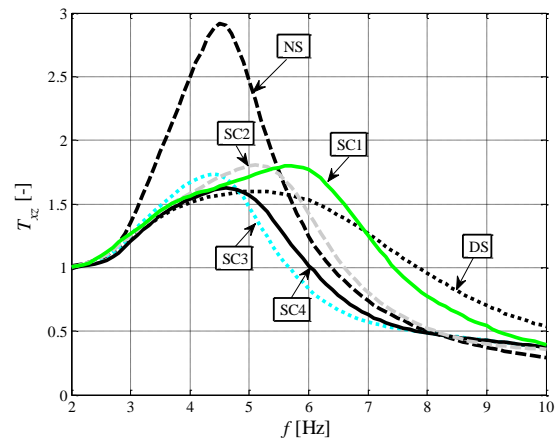
Fig. 8. Transmissibility coefficient T_{xz} vs. frequency f

The maximal value of T_{xz} (Fig. 8) is 2.92 (NS case) and 1.6 (DS case), obtained at respective frequencies f=4.5 Hz and f=5 Hz. It appears that the maximal amplitude of vibration registered in the DS case is nearly 1.8-fold lower than in the NS case. Interestingly, at frequency f=10 Hz, the amplitude of vibrations in the DS case is found to be 1.8-fold higher than in the NS case.

In the frequency range (2, 8) Hz in which the values of T_{xz} tend to decrease in relation to the NS case, the variants SC3 and SC4 appear to be most favourable. Further, in the entire frequency range the amplitude of vibrations in the variant SC4 was lower

when compared to DS. At frequency f=10 Hz, T_{xz} in the SC case was found to be 1.4-fold lower in relation to DS case and 1.3-fold higher than in the NS case.

Fig. 9. Relative velocity V_{xz} vs. frequency f

The highest rms values of relative velocity V_{xz} are registered in the case NS, in the frequency range (3, 8) Hz, and in the DS case at frequencies f > 8 Hz (see Fig. 9). In the frequency range (2, 3) Hz the values of V_{xz} registered in the cases NS, DS, SC are found to be similar.

Fig. 10. RMS harvester voltage U_h vs. frequency f

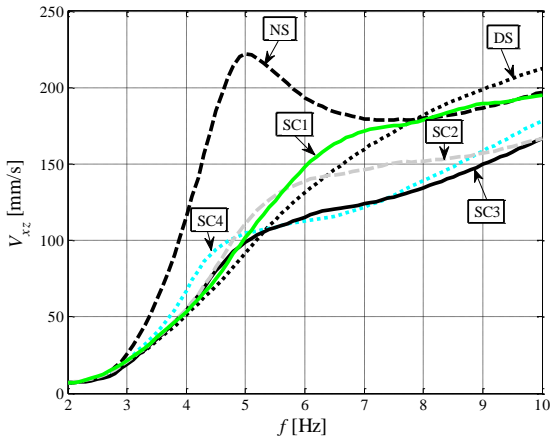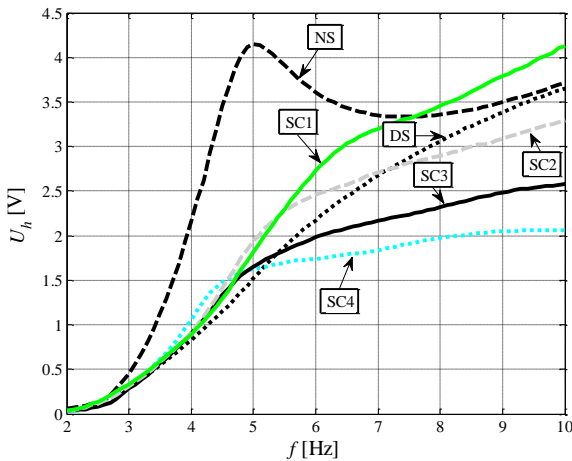When comparing plots in Figs. 9 and 10, it is apparent that the rms value of U_h in the NS case is proportional to relative velocity V_{xz}, reaching its maximal value at frequency f=5 Hz. In the DS and SC cases, voltage U_h tends to increase with frequency f. It appears that for the same velocity V_{xz}, the voltage U_h registered in the variant SC4 is lower than in the variant SC3, which is attributable to higher currents I_h in the circuit.

It is readily apparent (see plots in Fig. 11) that rms value of current I_h tends to increase with increasing capacitance of the condenser battery. At frequency f=10 Hz, the current output I_h in the variant SC is 5 times as high as that registered in the variant SC1 and that registered in the variant SC4 is 9 times higher than in the DS case.
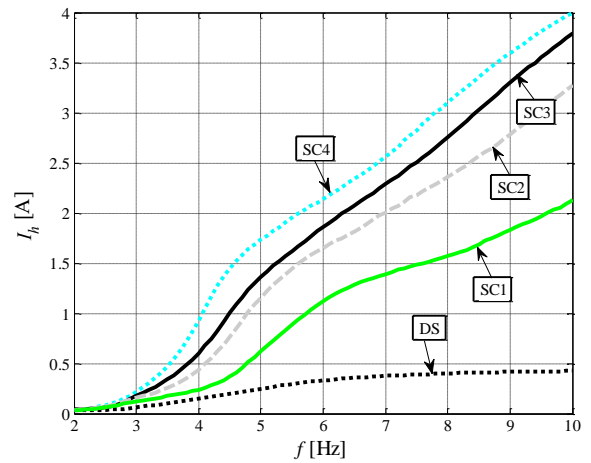
Fig. 11. RMS harvester current I_h vs. frequency f
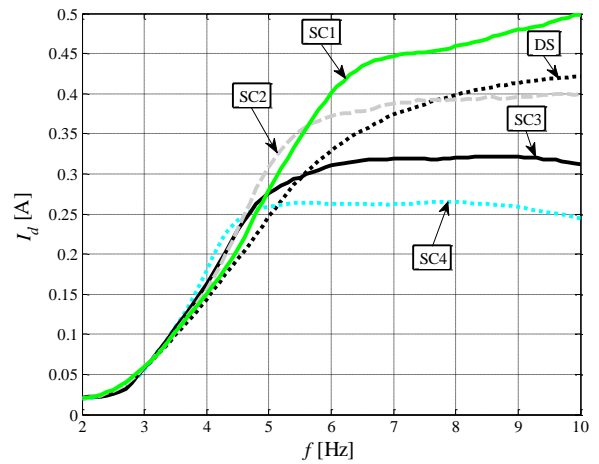
Fig. 12. RMS damper current I_d vs. frequency f
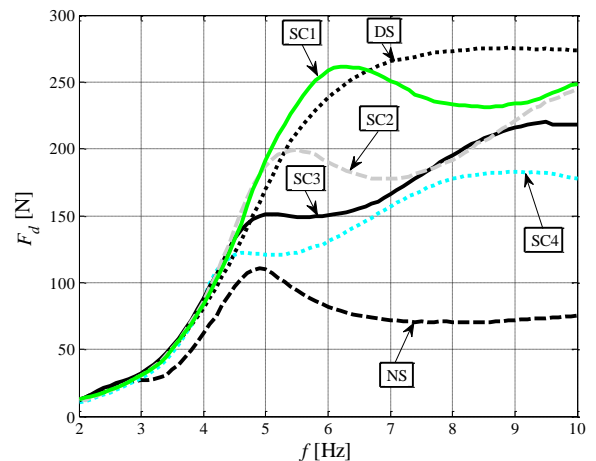
Fig. 13. RMS damper force F_d vs. frequency f

In the DS case an increase in frequency f results in an increase of the current rms value I_d (Fig. 12). In the variants SC2, SC3, SC4 no significant increase of the current I_d is registered at frequencies f > 6 Hz, which is attributed to a slower rate of voltage increase U_h (see Fig. 10) and a higher reactance X_c of the condenser battery. Actually, the higher the capacitance of the condenser battery, the lower current I_d at the frequency f > 6 Hz.

The lowest rms values of the damping force F_d (Fig. 13) are registered in the NS case. The maximal value of the force F_d is

Łukasz Jastrzębski, Bogdan Sapiński
Magnetorheological Self-Powered Vibration Reduction System with Current Cut-Off: Experimental Investigation

DOI 10.2478/ama-2018-0015

attained at the frequency f=4.9 Hz, coinciding with the maximal velocity V_{xz} (see Fig. 9). In the case DS, force F_d tends to increase with frequencies, at frequencies $f < 8$ Hz. For frequencies in excess of 8 Hz, the force F_d remains constant. In the SC case, at frequencies $f > 7$ Hz, the force F_d has lower values when compared to the DS case, which can be attributed to decrease in current I_d (see Fig. 12) and velocity V_{xz} (see Fig. 9).

4. SUMMARY

Investigations of a MR damper-based vibration reduction system with energy harvesting capability clearly demonstrate that at frequencies in excess of the resonance frequency, the increase of the vibration amplitude can be limited through the use of a current cut-off circuit (consisting of a battery of bipolar electrolytic capacitors). Results show that the system performance in the variant SC3 and SC4 is most satisfactory in terms of effective reduction of the sprung mass vibration amplitudes. Comparison of vibration amplitudes registered in those two variants and in the DS case reveals their decrease in the entire frequency range. As regards the NS case, however, amplitudes tend to decrease in the frequency range (2, 8) Hz only.

In particular, at frequency 10 Hz the vibrations amplitude in the variants SC3 and SC4 is higher by 30% than that registered in the NS case, whilst in the DS case, there is an amplitude increase by nearly 80%.

Further research efforts will focus on investigations of passive circuits utilising the voltage resonance effects, in order to improve the overall performance of a MR damper-based vibration reduction system with energy harvesting capability.

REFERENCES

1. **Ahamed R., Ferdaus Md. M., Li Y**. (2016), Advancement in energy harvesting magneto-rheological fluid damper: A review, *Korea-Australia Rheology Journal*, 28(4), 355−379.
2. **Chen C.**, **Liao W.H.** (2012), A self-sensing magnetorheological damper with power generation, *Smart Materials and Structures*, 21, 025014.
3. **Choi K.M., Jung H. J., Lee H. J, Cho S.W.** (2007), Feasibility study of smart passive control system equipped with electromagnetic induction device, *Smart Materials and Structures*, 16, 2323-2329.
4. **Choi Y.T., Werely N.M** (2009), Self-powered magnetorhelogical dampers, *Journal of Vibration and Acoustics*, 131, 44−50.
5. **Jastrzębski Ł., Sapiński B.** (2016), Electrical interface for a self-powered MR damper-based vibration reduction system, *Acta Mechanica et Automatica*, 10(3), 165−172.
6. **Sapiński B., Snamina J., Jastrzębski Ł., Staśkiewicz A.,** (2011), Laboratory stand for testing of self-powered vibration reduction systems, *Journal of Theoretical and Applied Mechanics*, 49(4), 1169–1181.
7. **Sapiński B.** (2008), An experimental electromagnetic induction device for a magnetorheological damper, *Journal of Theoretical and Applied Mechanics*, 46(4), 933−947.
8. **Sapiński B.** (2010), Vibration power generator for a linear MR damper, *Smart Materials and Structures,* 19, 105012.
9. **Sapiński B.** (2011), Experimental study of a self-powered and sensing MR damper-based vibration control system, *Smart Materials and Structures*, 20, 105007.
10. **Sapiński B., Rosół M., Jastrzębski Ł.** (2011), Charakterystyki semiaktywnego układu redukcji drgań z odzyskiem energii, *Pomiary, Automatyka, Kontrola*, 57(5), 502−506.
11. **Sapiński B., Rosół M., Węgrzynowski M.** (2016), Investigation of an energy harvesting MR damper in a vibration control system, *Smart Materials and Structures*, 25, 125017.
12. **Wang D.H.**, **Bai X.X.** (2013), A magnetorheological damper with an integrated self-powered displacement sensor, *Smart Materials and Structures*, 22, 075001.
13. **Wang D.H., Bai X.X., Liao W.H.** (2009), Principle, design and modeling of an integrated relative displacement magnetorheological damper based on electromagnetic induction, *Smart Materials and Structures*, 18, 095025.
14. **Xinchun G., Yonghu H., Yi R., Hui L., Jinping O.** (2015), A novel self-powered MR damper: Theoretical and experimental analysis, *Smart Materials and Structures*, 24, 105033.
15. **Zhu S.Y.**, **Shen W.A.**, **Xu Y.L.**, **Lee W.C.** (2012), Linear electromagnetic devices for vibration damping and energy harvesting: Modeling and testing, *Engineering Structures*, 34, 198−212.

DIGITAL IMAGE CORRELATION TECHNIQUE AS A TOOL
FOR KINEMATICS ASSESSMENT OF STRUCTURAL COMPONENTS

Adam BRODECKI*, Tadeusz SZYMCZAK*, Zbigniew KOWALEWSKI**

*Centre for Material Testing, Motor Transport Institute, ul. Jagiellońska 80, 03-301 Warszawa, Poland
**Department of Experimental Mechanics, Institute of Fundamental Technological Research, ul. Pawińskiego 5B, 02-106 Warszawa, Poland

adam.brodecki@its.waw.pl, tadeusz.szymczak@its.waw.pl, zkowalew@ippt.pan.pl

Abstract: The paper reports the results of tests carried out for kinematic properties determination of components under cyclic loading. DIC system called 5M PONTOS was employed to follow variations of displacement versus time. It was conducted by the use of markers stuck on selected sections of components tested. The results are presented in 2D and 3D coordinate systems expressing behaviour of such elements as: mechanical coupling device, boat frame and car engine. These data enabled to capture weak and strong sections of the component examined at various loading conditions.

Key words: Digital Image Correlation System, Cyclic Loading, PONTOS, Motion, Displacement, 3D Coordinate System

1. INTRODUCTION

Digital Image Correlation (DIC) method is the contactless technique, which has been developed in the last 15 years. Application of new mathematical algorithms and great progress in CCD (Charge-Coupled Device) cameras quality have enabled designing the effective DIC systems. Equations for determination of solid bodies deformation have been employed to follow differences on a sprayed grey background having black dots stochastically arranged (Chu et al., 1985; Bornert et al., 2009; Long et al., 2012). On the basis of these data the components of displacement can be calculated directly, and subsequently, the full-field strain maps elaborated. As it is noticed by many research groups, this method can be applied for examination of various types of specimens such as: flat (Toussaint et al., 2008), tubular and hourglass (Kamaya and Kawakubo, 2011) and CT.

2. SELECTED ACHIEVEMENTS IN DIC APPLICATION

DIC technique can be used to measure strain distribution on flat specimen under biaxial stress state, even for unidirectional carbon fibre-reinforced epoxy composite [+45°/0°/-45°/90°]2s (Gower and Shaw, 2006). As it was investigated by the authors the DIC results are similar to data from FEA (Finite Element Analysis) and strain gauge measurements, Fig. 1a.

DIC method enables to follow evaluation of the strain distribution close to various types of defects (natural and artificial) and capturing important features appearing before material fracture (Szymczak et al., 2016a, b). Young's modulus (E), yield point (YP) and ultimate tensile strength (UTS) can be determined by means of DIC method (Szymczak et al., 2016b). It was also confirmed later for a high-strength steel called the S700 MC, Fig. 1b.

DIC technique can be also used for determination of the kinematic properties of various elements. In this case, DIC uses markers stuck on selected zones of components tested, Fig. 2. They are in the form of white-black dots covered very often by reflected layer. Their arrangement is usually formulated on the basis of geometrical axes of the object examined.
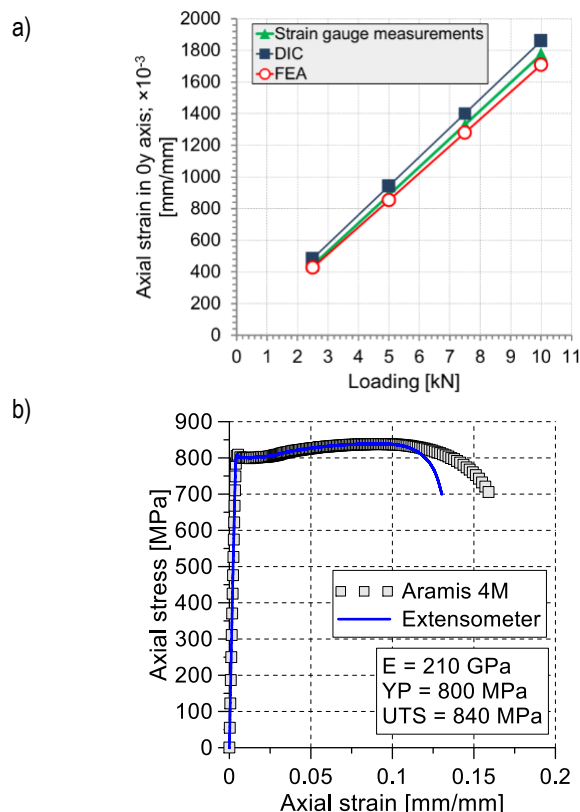
a)

b)

Fig. 1. Comparison of the results obtained using various measurement techniques: (a) strain gauge measurements, DIC and FEA (Gower and Shaw, 2006); (b) DIC and extensometer for the S700 MC steel

Dimensions of markers (GOM) are within a range from 0.4 mm to 25 mm. They can be calculated using geometrical features of DIC system and test details like a dimension of the measurement zone in the 0x axis direction and a value of coefficient depending on the system applied: 0.0004 (4 and 5M PONTOS), 0.002 (12M PONTOS) and 0.4 mm (for high speed cameras). Typical DIC system contains two cameras (stereo device), working stations and calibration equipment (Fig. 3).
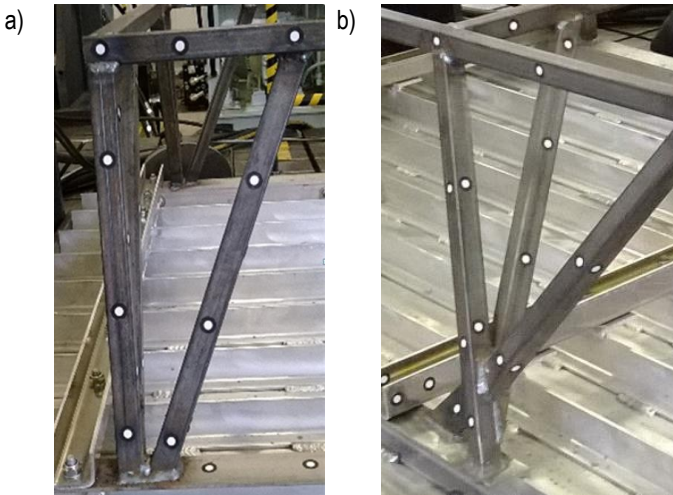

Fig. 2. Distribution of markers for measurements in: (a) 2D; and (b) 3D coordinate systems

Fig. 3. The 5M PONTOS calibration devices: (a) cross; (b) plate

Application of the 5M PONTOS requires calibration stage, which should be directly conducted before the main test. This part of experimental procedure employs cross (Fig. 3a) or plate (Fig. 3b) having measurements dots located at various orientation in 3D coordinate system. The smallest sensor is called CQ 10×8

[mm] and enables observation of the measuring zone from 9×7 [mm] up to 12×10 [mm]. The biggest one is signed as CC20 2000×1600 [mm] and it is used for the measuring volume of 1600/1300 [mm] × 2300/1900 [mm]. These zones are followed by the use of CCD camera chip at resolution of 2448×2050 pixels. Maximum sampling rate at typical configuration is equal to 15 Hz and 29 Hz with binning. The equipment is positioned in the centre of the measurement zone, and it is subjected to movements and rotations reflecting possible location of the object (www.gom.com).

In the case of 5M PONTOS two kinds of markers can be applied. Typically, when lightening conditions are acceptable, black dots on a white background can be used. In the opposite case the markers with a fluorescence layer are recommended. Their diameters can be equal to: 0.4 mm, 0.8 mm, 1.5 mm, 3 mm, 5 mm, 8 mm, 12 mm, 18 mm and 25 mm. They are selected applying multiplication of length of measuring volume and coefficient, which is equal to 0.004 for the 5M PONTOS (www.gom.com).

A number of data in the form displacement versus time is limited by the number of photos for recording. Therefore, all tests under cyclic loading should have clearly selected stages for displacement analysis.

The 5M PONTOS device was used to determine deformation and vibration of a large-volume tractor tyre during dynamic test (Brinkmann et al., 2007). Vertical mode shape on the top reversal point of the tyre was elaborated on the basis of directions and magnitude of displacement determined for each measuring point.

An analysis of the airplane wing under cyclic loading is another external application of DIC system (Berger et al., 2010). Variations of displacement in 3D coordinate system versus frequency were presented and compared with data recorded using accelerometer. Differences between the results captured by both techniques were significant. They were within a range from 0% to 7.38% for seven measurement points taken into account. It has to be mentioned however, that for some other points it was much higher.

The DIC technique was also successfully applied for identification of a shape mode of the wind turbine blade (Bagersada et al., 2012). The results of the wind parameters analysis at the beginning and subsequent stages enabled identification of free vibration. Two modes of shape were extracted and compared with their form before excitation.

DIC was also used for capturing of kinematic parameters of the NASA vehicle conception called The Scarab (Creager et al., 2015). Tracking of each wheel was executed by means of the PONTOS system.

This work supplements in a certain way the previous knowledge regarding the research possibilities of DIC.

3. EXPERIMENTAL PROCEDURE

Testing procedure was designed to check suitability of the 5M PONTOS for detection of displacement components in 2D and 3D measurements of various structural elements such as: mechanical coupling device, car engine, and boat frame. Various types of loading were applied to enforce a movement of structural elements tested.

Symmetrical signal of cyclic force was applied for examination of the coupling device up to 2×10^6 cycles, Fig. 4. An amplitude of the force signal was calculated using the following relationship:

$$F_{hs\,res} = \pm 0.6\, D, \qquad\qquad (1)$$

where: D – force declared by the producer. According to the standard (Regulation No 55) its magnitude is defined by the following expression:

$$D = \frac{m_C m_T}{m_C + m_T} \cdot g, \qquad\qquad (2)$$

where: m_C – vehicle mass, m_T – trailer mass; g – acceleration due to gravity. Parameters of the coupling device are detailed on its technical specification.

A frequency of the cyclic force is determined on the basis of working conditions of structural components taken into account. Here, it was equal to 10 Hz. According to the standard (Regulation No 55) the maximum frequency should be lower than 35 Hz. An angle of the force is determined by the relationship between a centre of the coupling ball and a horizontal line passing through the fixing point of the coupling device which is the highest of the nearest. If the line is above the ball centre, the test shall be conducted at an angle +15°±1° (Fig. 4), otherwise –15°±1°. Deformation and cracks are the basis for recognizing the inherent quality of the product tested.

Among the most important features of the experimental procedure one can indicate a mounting of the equipment in the same position as it appears during exploitation. The coupling device was tested to check whether it could be mounted in the Sports Utility Vehicle (in this case Hyundai Tucson). Markers were used to capture displacement in 3D coordinate system, Fig. 4. They were stuck along the major axis of the coupling device.

The boat frame was examined using displacement control. Symmetrical signals were applied to load a beam. An induction sensor was used to measure a movement in the selected single direction. Markers for DIC analysis were located along major axes of the frame components tested. The basic coordinate system was attributed to the anti-vibration platform. The main aim of the experiment was to examine the frame resistance under fatigue conditions.

DIC system was also used to investigate vibration of 3.0 diesel engine of Porsche Cayenne (SUV) after exploitation. In this case markers were arranged on the engine cover and bumper of the car. The major engine axis was rotated under rotational velocity up to 2500 RPM. The aim of this experiment was to identify vibrations of the car engine with respect to exhaustion of the gum-metal absorbers.

The PONTOS 5M was applied in all stages of the experimental procedure to capture variations of displacement as a function of time. It enabled to determine distribution of displacement vectors in 2D and 3D coordinate systems. The results were analysed in order to indicate a characteristic features of the objects examined.

4. RESULTS

Data showing variations of displacement for the structural components tested are presented in Figs.4÷6. Looking at the results a distribution of displacement vectors can be easily studied.

In the case of coupling device this data were represented by displacement in the 0x direction, because such data are very important from engineering point of view. The results necessary for designing of this element can be easily deduced basing on DIC's data. They can be presented in the form of digital files including 3D displacement components versus time. On the basis

of these data a location and deflection of major axis of the coupling device can be established. Such results also enable identification of the weak and strong zones under the cyclic loading. More importantly, a movement of elements in the mounting zone can be evaluated.
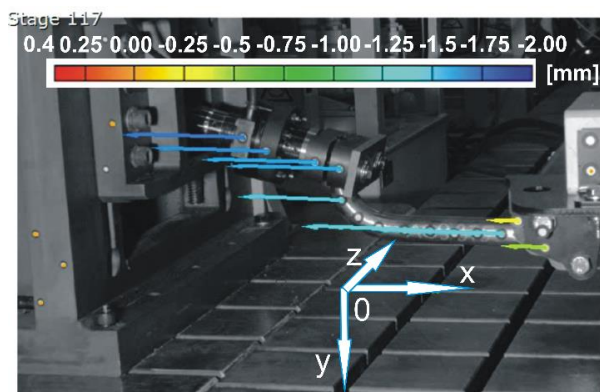
Fig. 4. Distribution of displacement in 0x axis direction for mechanical coupling device examined under cyclic loading
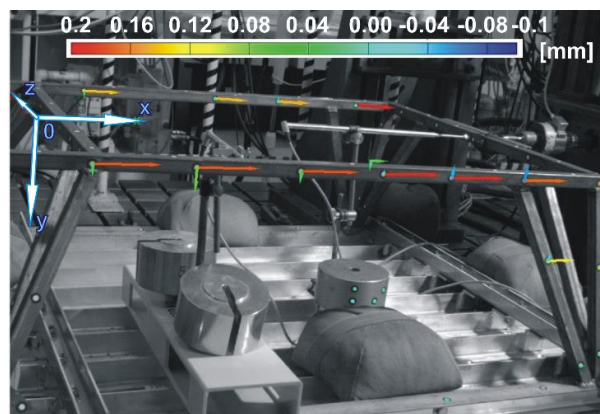
Fig. 5. Components of displacement in 3D coordinate system determined in fatigue test of the boat frame at 1×10^6 cycles
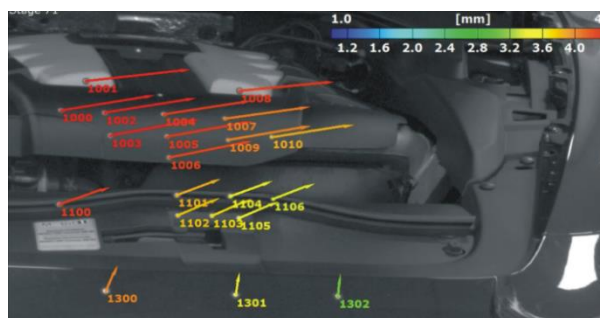
Fig. 6. Distribution of resultant displacement vector in 3D coordinate system for selected rotational velocity of the car engine of Porsche Cayenne
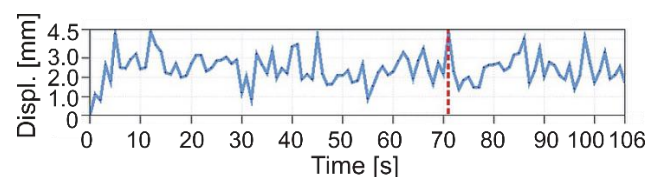
Fig. 7. Magnitudes of the displacement vector in 3D coordinate system for the 3.0 diesel car engine of Porsche Cayenne after exploitation (results representing point 1004 in Fig. 6)

The results representing boat frame investigation are illustrated in the form of displacement vector components, Fig. 5. They enable to distinguish differences between movement of beams and bracket. Also a behaviour of the weld zones can be characterised (appeared in the lowest part of the structural component), Fig. 5. The weakest regions can be easily identified, since they are represented by a low stiffness or damage zones that correspond to the displacement increase.

Car engine was studied on the basis of variations of displacement resultant vector serving as the effective indicator of vibrations, Fig. 6. In the analysis an orientation of the vectors was considered. The vectors were determined for different values of rotational velocity. The results showed a single direction of displacement vector. It was observed for the entire range of rotational velocity applied (up to 2 500 RPM). In comparison to the typical behaviour of car engine the vectors length and direction well identify a difference in mechanical properties of the gummetal absorber. It is clearly illustrated in Fig. 7. The resultant vector achieved the maximum value equal to 4.5 mm. On the basis of these data engineers are able to estimate exhaustion of the anti-vibration components.

5. SUMMARY

DIC method enables capturing the results in 2D and 3D coordinates systems for various types of loading (static or cyclic).

It can be used for determination of the full-field strain maps, stress-strain characteristics and such mechanical properties as: Young's modulus, yield point and ultimate tensile strength. The results can be elaborated in the form of maps representing distribution of: strain components, major and minor strain, and equivalent strain.

In the case of structural components their kinematic quantities, like a displacement, velocity and acceleration, can be determined as a function of time. Each of them can be represented by vectors, and variations of their magnitudes versus time. On the basis of DIC results a deflection together with detection of the strong and soft zones located on the structural components can be effectively identified.

REFERENCES

1. **Baqersada J., Carra J., Lundstroma T., Niezrecki Ch., Avitabilea P., Slattery M.,** (2012), Dynamic characteristics of a wind turbine blade using 3D digital image correlation, Health Monitoring of Structural and Biological Systems 2012, edited by Tribikram Kundu, *Proc. of SPIE*, 8348.
2. **Berger H., Klein M., Lambert F., Levadoux B.,** (2010), Optical Vibration Measurement and Frequency Response Analysis on Large Structures under Multiple Excitation Load Conditions, *Proceedings of ISMA2010 including USD2010*, 1693–1702.
3. **Bornert M., Brémand F., Doumalin P., Dupré J.-C., Fazzini M., Grédiac M., Hild F., Mistou S., Molimard J., Orteu J.-J., Robert L., Surrel Y., Vacher P., Wattrisse B.,** (2009), Assessment of Digital Image Correlation Measurement Errors: Methodology and Results, *Experimental Mechanics*, 49, 353–370.
4. **Brinkmann Ch., Haberland J., Böttinger S., Erne O., Sanow G.,** (2007), Optical 3D Measuring System for Investigating Tyre Deformations, *Tractor Technology*, 62(5), 326–327.
5. **Chu T.C., Ranson W.F., Sutton M.A., Peters W.H.,** (1985), Applications of digital-image-correlation techniques to experimental mechanics, *Experimental Mechanics*, 232–244.
6. **Creager C., Johnson K., Plant M., Moreland S., Skonieczny K.,** (2015), Push–pull locomotion for vehicle extrication, *Journal of Terramechanics*, 57, 71–80.
7. **Gower M.R., Shaw R.M.,** (2006), Towards a planar cruciform specimen for biaxial characterization of polymer matrix composites, *Applied Mechanics and Materials*, 24–25, 115–120.
8. **Kamaya M., Kawakubo M.,** (2011), A procedure for determining the true stress–strain curve over a large range of strains using digital image correlation and finite element analysis, *Mechanics of Materials*, 43, 243–253.
9. **Long X., Fu S., Qi Z., Yang X., Yu Q.,** (2012), Digital image correlation using stochastic parallel-gradient-descent algorithm, *Experimental Mechanics*, DOI 10.1007/s11340-012-9667-4.
10. **Szymczak T.**, **Kowalewski Z.L., Brodecki A.,** (2016a), Determination of artificial defects in material under monotonic tension by the use of FEM and DIC methods, *Materials Today: Proceedings*, 3, 3, 1171–1176.
11. **Szymczak T., Kowalewski Z.L., Brodecki A.,** (2016b), Digital Image Correlation method for investigations of materials and engineering structures, *Technical Suspervision (Dozór Techniczny)*, 4, 22–3 (in Polish).
12. **Toussaint F., Tabourot I., Vacher P.,** (2008), Experimental study with a Digital Image Correlation (DIC) method and numerical simulation of an anisotropic elastic-plastic commercially pure titanium, *Archives of Civil and Mechanical Engineering*, VIII, 3, 131–143.
13. **Regulation No 55** of the Economic Commission for Europe of the United Nations (UN/ECE) — Uniform provisions concerning the approval of mechanical coupling components of combinations of vehicles, 28.08.2010.
14. www.gom.com

MECHANICAL BEHAVIOUR AND PHASE TRANSITION MECHANISMS OF A SHAPE MEMORY ALLOY BY MEANS OF A NOVEL ANALYTICAL MODEL

Andrea CARPINTERI*, Vittorio DI COCCO, Giovanni FORTESE*, Francesco IACOVIELLO**, Stefano NATALI***,
Camilla RONCHEI*, Daniela SCORZA*, Sabrina VANTADORI*, Andrea ZANICHELLI***

* Department of Engineering and Architecture, University of Parma, Parco Area delle Scienze 181/A, 43124 Parma, Italy
** Department of Civil and Mechanical Engineering University of Cassino and Lazio Meridionale, Via G. Di Biasio 43, 03043 Cassino (FR), Italy
*** Department Chemical Engineering Materials Environment, University of Roma "La Sapienza", via Eudossiana 18, 00184 Rome, Italy

andrea.carpinteri@unipr.it, v.dicocco@unicas.it, giovanni.fortese@studenti.unipr.it, iacoviello@unicas, stefano.natali@uniroma1.it,
camilla.ronchei@nemo.unipr.it, daniela.scorza@unipr.it, sabrina.vandatori@unipr.it, andrea.zanichelli1@studenti.unipr.it

received 19 April 2017, revised 6 June 2018, accepted 8 June 2018

Abstract: The aim of the present paper is to examine both the fatigue behaviour and the phase transition mechanisms of an equiatomic pseudo-elastic NiTi Shape Memory Alloy through cyclic tests (up to 100 loading cycles). More precisely, miniaturised dog-bone specimens are tested by using a customised testing machine and the contents of both austenite and martensite phase are experimentally measured by means of X-Ray diffraction (XRD) analyses. On the basis of such experimental results in terms of martensite content, an analytical model is here formulated to correlate the stress-strain relationship to the phase transition mechanisms. Finally, a validation of the present model by means of experimental data pertaining the stress-strain relationship is performed.

Key words: Fatigue Behaviour, Phase Transition Mechanisms, Shape Memory Alloy, Tensile Cyclic Test, X-Ray Diffraction Analyses

1. INTRODUCTION

Shape memory alloys (SMAs) are an important class of materials since they are able to recover the initial shape thanks to reversible phase transition mechanisms, even after severe deformations.

The near equiatomic Nickel-Titanium binary system (NiTi) belongs to the class of SMAs (Shimamoto et al., 2004; Otuska and Ren, 2005; Li et al., 2009). Large deformations induced in such alloys are perfectly recovered by two possible paths:

– such alloys spontaneously return to the original pre-deformation appearance when heated at a characteristic temperature (shape memory effect);
– such alloys recover the original pre-deformation appearance by simply removing the mechanical load (pseudoelasticity or superelasticity).

The explanation of these peculiar behaviours can be found in the crystallography and thermodynamics of SMAs (Li et al., 2009).

Due to the above unique features, NiTi alloys are currently used in mechanical, civil and medical field(Kuribayashi et al., 2006), and the use of NiTi alloys is expected to rise due to a continuous improvement (Bujoreanu, 2008).

In last decades, several experimental tests have been performed in order to better understand the thermo-mechanical properties of such alloys, and some analytical and numerical models have been developed to describe their mechanical and functional behaviour (that is, the microstructural transition from austenite to martensite and vice-versa). In particular, the scientific community has agreed that crack initiation and propagation are significantly affected by the phase transition mechanisms and, consequently, NiTi alloys exhibit unusual fatigue and fracture responses with respect to common alloys (Shimamoto et al., 2004). Experimental

studies have recently been performed for both static (Maletta et al., 2013) and cyclic loading conditions (Robertson et al., 2007; Gall et al., 2008). Furthermore, numerical studies have been carried out by using both standard finite element codes (Maletta et al., 2009) and special constitutive models for SMAs (Freed and Banks-Sills, 2001). Finally, many analytical models have been proposed (Maletta and Furgiuele, 2010; Baxevanis and Lagoudas, 2012; Malett, 2012).

The aim of the present paper is to examine both the fatigue behaviour and the phase transition mechanisms of an equiatomic pseudo-elastic NiTi Shape Memory Alloy through cyclic tests (up to 100 loading cycles). Miniaturised dog-bone specimens are tested by using a customised testing machine, and the contents of both austenite and martensite phase are experimentally measured by means of X-Ray diffraction (XRD) analyses.

On the basis of such experimental results, an analytical model is here formulated to correlate the stress-strain relationship to the phase transition mechanisms. The model assumes that the fatigue behaviour of the system (that is, phases and test machine) can be schematised as that of one spring, or two springs arranged in series or in parallel. Finally, a validation of the present model by means of experimental data pertaining the stress-strain relationship is performed.

2. EXPERIMENTAL CAMPAIGN

An equiatomic pseudo-elastic NiTi alloy, which exhibits a pseudo elastic behaviour, is made in the laboratory by using a vacuum furnace. The miniaturised specimens are characterised by a flat dog-bone shape and the geometrical sizes are reported in Fig. 1.

The tensile cyclic tests are performed by means of a custom-

ised testing machine, which allows in situ XRD measurements (details can be found in Di Cocco et al. (2014a, b).
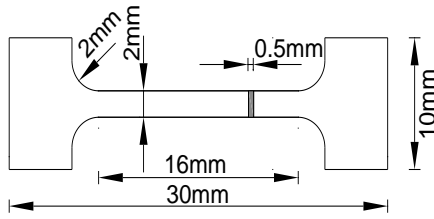

Fig. 1. Geometry miniaturised flat dog-bone specimen.

In particular, a diffractometer equipped with a vertical powder goniometer is employed in order to perform the XRD analyses. Moreover, the PowderCell software allows to determine both the theoretical diffractograms and the structure models (details on the XRD analyses are provided in Di Cocco et al. (2014a).

In order to carry out the XRD analyses at fixed values of the applied deformation, the testing machine is equipped with a re-movable loading frame and two load cells Leane FGP 1000. Since no strain gauges are used, a linear variable differential transducer is employed in order to measure the whole elongation of the specimen.
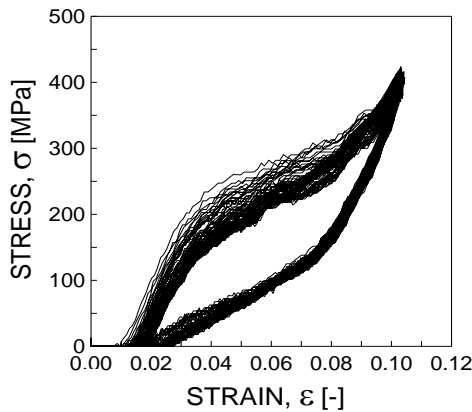

Fig. 2. Experimental fatigue behaviour: stress- strain relationship

Each tensile cyclic test is performed step by step under displacement control of the crosshead until a number of loading cycles equal to 100 cycles is reached.

For each cycle, the phases content is experimentally determined at ten fixed values of strain (named strain steps in the following) by means of XRD analyses.

The experimental relationship between stress, σ, and strain, ε, is reported in Fig. 2.

For each of the aforementioned steps, the XRD analyses allow to quantify the phase transition mechanisms through the diffraction spectra. For instance, considering the initial loading condition ($\varepsilon = 0$), the diffraction spectrum corresponds to the austenite phase (cubic lattice cell), whereas the diffraction spectrum related to $\varepsilon = 0.1$ corresponds to the martensite phase (monocline lattice cell). Moreover, from the experimental results, it is in general observed that both the austenite-martensite transition in the loading condition and the martensite-austenite transition in the unloading condition are not characterised by a linear trend.

The intensity of austenitic and martensitic peaks allows to quantify the contents of both austenite and martensite. For a given

value of strain ε, the content of austenite is proportional to the maximum amplitude of austenite peak in undeformed initial condition, corresponding to fully austenitic structure.

3. ANALYTICAL MODEL

The fatigue behaviour of the NiTi SMA tested under tensile cyclic loading is hereafter described by means of a novel analytical model. In particular, the stress-strain relationship is defined in an analytical way as a function of the phase transition mechanisms (from austenite to martensite and vice-versa).
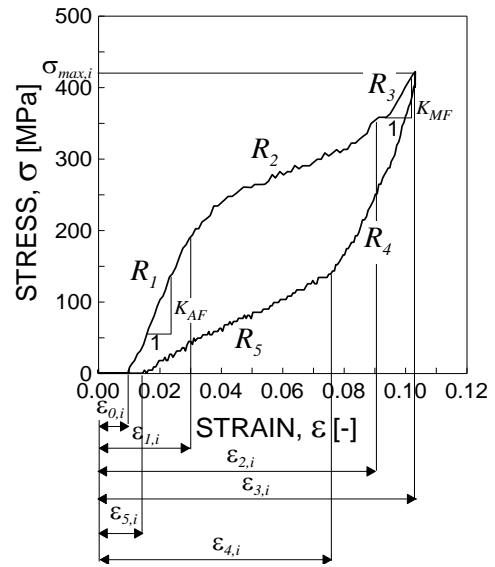
Fig. 3. Five regions characterised by different contents of austenite and martensite in the stress-strain diagram of the i-th loading cycle

On the basis of the experimental results presented in Section 2, it is possible to define five regions, characterised by different contents of austenite and martensite, in the stress-strain diagram (Fig. 2). For the i-th cycle (with $i = 1, \ldots, 100$), the following five regions can be identified (see Fig. 3):

1. Region 1 ($\varepsilon_{0,i} \leq \varepsilon \leq \varepsilon_{1,i}$, R_1 in Fig. 3): the content of the austenite phase is predominant and approximately constant with increasing ε;
2. Region 2 ($\varepsilon_{1,i} \leq \varepsilon \leq \varepsilon_{2,i}$, R_2 in Fig. 3): the content of austenite phase decreases while the content of martensite phase increases with increasing ε;
3. Region 3 ($\varepsilon_{2,i} \leq \varepsilon \leq \varepsilon_{3,i}$ R_3 in Fig. 3): the content of the martensite phase is predominant and approximately constant with increasing ε;
4. Region 4 ($\varepsilon_{4,i} \leq \varepsilon \leq \varepsilon_{3,i}$ R_4 in Fig. 3): the content of the martensite phase is predominant and approximately constant with decreasing ε;
5. Region 5 ($\varepsilon_{5,i} \leq \varepsilon \leq \varepsilon_{4,i}$ R_5 in Fig. 3): the content of martensite phase decreases while the content of austenite phase increases with decreasing ε.

Since the values of austenite and martensite are experimentally measured only at 1, 50 and 100 loading cycles, a diffusion model is here employed to estimate the phase content as a function of the strain ε, for each i-th cycle. The content of martensite, M, is given by the following expression:

$$M(\%) = \frac{100}{1+a\cdot\exp(-b\cdot\varepsilon)} \tag{1}$$

where a is equal to 700 and 70 for loading and unloading condition, respectively. Moreover, b is a parameter depending on the number i of cycles (with $i \geq 1$), defined as follows:

$$b = -\ 4.2\ln(i) + 1 \tag{2}$$

The content of austenite phase, A, is computed by using the following equation:

$$A(\%) = 100 - M(\%) \tag{3}$$

The aforementioned five regions are characterised by different limit values of ε, which are defined for the i-th cycle as follows:

1. $\varepsilon_{0,i}$ is computed according to the following expression, obtained from a best-fit procedure by considering the experimental values of $\varepsilon_{0,i}$ for $i = 1.50$ and 100 loading cycles:

$$\varepsilon_{0,i} = 0.009763 \cdot (i)^{0.1525} \tag{4}$$

2. $\varepsilon_{1,i}$ is determined recalling Eqs (1) and (2) and assuming $a = 700$, $i = 1$ and $M = 3\%$, being $\varepsilon_{1,i}$ almost independent of the number i of cycles (Figs. 2 and 3): $\varepsilon_{1,i} = \varepsilon_1 = 0.030750$;
3. $\varepsilon_{2,i}$ is determined recalling Eqs (1) and (2) and assuming $a = 700$, $i = 1$ and $M = 95\%$, being $\varepsilon_{2,i}$ almost independent of the number i of cycles (Figs 2 and 3): $\varepsilon_{2,i} = \varepsilon_2 = 0.094955$;
4. $\varepsilon_{3,i}$ is determined recalling Eqs (1) and (2) and assuming $a = 700$, $i = 1$ and $M = 98\%$, being $\varepsilon_{3,i}$ almost independent of the number i of cycles (see Figs 2 and 3): $\varepsilon_{3,i} = \varepsilon_3 = 0.104429$;
5. $\varepsilon_{4,i}$ is determined recalling Eqs (1) and (2) and assuming $a = 70$, $i = 1$ and $M = 98\%$, being $\varepsilon_{4,i}$ almost independent of the number i of cycles (Figs 2 and 3): $\varepsilon_{4,i} = \varepsilon_4 = 0.081280$;
6. $\varepsilon_{5,i}$ is computed according to the following expression, obtained from a best-fit procedure by considering the experimental values of $\varepsilon_{5,i}$ for $i = 1.50$ and 100 loading cycles:

$$\varepsilon_{5,i} = 0.000158 \cdot (i) + 0.010990 \tag{5}$$

Considering the above limit values of ε, an analytical model is hereafter formulated in order to describe the relationship between stress and strain of the NiTi SMA. In particular, the fatigue behaviour is analytically interpreted as a system of springs characterised by a stiffnesses depending on the phase transition mechanism, and more precisely:

a) Region 1 (loading condition). The stress-strain relationship is characterised by a linear trend and the fatigue behaviour of the system is schematised as that of one spring with a stiffness equal to K_{AF}:

$$\sigma_{1,i}(\varepsilon) = K_{AF} \cdot \left(\varepsilon - \varepsilon_{0,i}\right) \tag{6}$$

where $\varepsilon_{0,i}$ is computed through Eq. (4). The stiffness K_{AF} is experimentally measured (Fig. 3), and corresponds to that offered by the austenite phase, being the content of martensite approximately equal to zero in this region;

b) Region 3 (loading condition). The stress-strain relationship is characterised by a linear trend and the fatigue behaviour of the system is schematised as that of one spring with a stiff-

ness equal to K_{MF}:

$$\sigma_{3,i}(\varepsilon) = K_{MF} \cdot (\varepsilon - \varepsilon_3) + \sigma_{\max,i} \tag{7}$$

where the dependence of $\sigma_{\max,i}$ from i is obtained by means of a best-fit procedure, by considering the experimental values of $\sigma_{\max,i}$ for $i = 1.50$ and 100 loading cycles:

$$\sigma_{\max,i} = 421.92 \cdot (i)^{-0.0088} \tag{8}$$

The stiffness K_{MF} is experimentally measured (Fig. 3), and corresponds to that offered by the martensite phase, being the content of austenite approximately equal to zero in this region;

c) Region 2 (loading condition). The stress-strain relationship is characterised by a non-linear trend and the fatigue behaviour of the system is schematised as that of two springs in series with stiffness depending on both ε and the number i of loading cycles:

$$\sigma_{2,i}(\varepsilon) = \frac{1}{\dfrac{1}{K_{AF,i}(\varepsilon)} + \dfrac{1}{K_{MF,i}(\varepsilon)}} \cdot \varepsilon + D_i =$$

$$[A_i\varepsilon^2 + B_i\varepsilon + C_i] \cdot \varepsilon + D_i \tag{9}$$

where the dependence of A_i and B_i on i are obtained through a best-fit procedure by considering the experimental values of A_i and B_i, for $i = 1.50$ and 100 loading cycles:

$$A_i = 390.625 \cdot (i)^2 - 36719.659 \cdot (i) + 1829350.489 \tag{10a}$$

$$B_i = -72.773 \cdot (i)^2 + 6975.84 \cdot (i) - 343752.288 \tag{10b}$$

Moreover, the crossing conditions of $\sigma_{2,i}$ by the two points $\left(\varepsilon_1, \sigma_{1,i}(\varepsilon_1)\right)$ and $\left(\varepsilon_2, \sigma_{3,i}(\varepsilon_2)\right)$ are employed in order to determine the coefficients C_i and D_i;

d) Region 4 (unloading condition). The stress-strain relationship is characterised by a linear trend and the fatigue behaviour of the system is schematised as that of two springs in parallel with constant stiffness:

$$\sigma_{4,i}(\varepsilon) = (K_{MF} + K_m) \cdot \varepsilon + F_i \tag{11}$$

where K_m is the testing machine stiffness, experimentally measured and equal to 6227.57 MPa. Moreover, the crossing condition of $\sigma_{4,i}$ by the point $\left(\varepsilon_3, \sigma_{\max,i}\right)$ is employed in order to determine the coefficient F_i;

e) Region 5 (unloading condition). The stress-strain relationship is characterised by a linear trend and the fatigue behaviour of the system is schematised as that of two springs in series with stiffness depending on both ε and the number i of loading cycles:

$$\sigma_{5,i}(\varepsilon) = \frac{1}{\dfrac{1}{K_{AF,i}(\varepsilon)} + \dfrac{1}{K_{MF,i}(\varepsilon)}} \cdot \varepsilon + H_i = G_i \cdot \varepsilon + H_i \tag{12}$$

where the coefficients G_i and H_i are determined through crossing conditions of $\sigma_{5,i}$ by the two points $\left(\varepsilon_4, \sigma_{4,i}(\varepsilon_4)\right)$ and $\left(\varepsilon_{5,i}, 0\right)$.

Finally, the relationship between stress and strain for each value of i (that is, for $i = 1,\ldots,100$ cycles) is computed through Eqs (1) – (12), where the strain limit values of the five above regions are computed according to Eqs (1),(2) for each cycle.
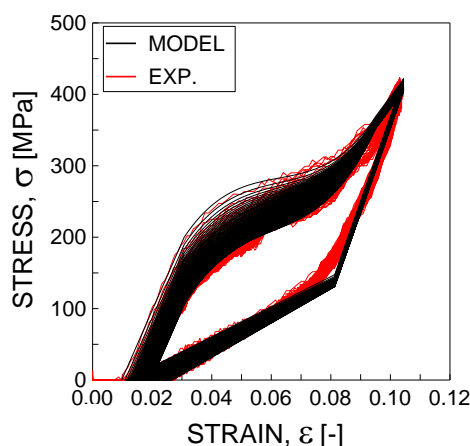
REFERENCES

1. **Baxevanis T., Lagoudas D.** (2012), A mode I fracture analysis of a center-cracked in niti shape memory alloy panel under plane stress, *International Journal of Fracture*, 175, 151–166.
2. **Bujoreanu L.G.** (2008), On the influence of austenitization on the morphology of alfa-phase in tempered Cu–Zn–Al shape memory alloys, *Materials Science and Engineering A*, 481, 395–403.
3. **Di Cocco V., Iacoviello F., Maletta C., Natali S.** (2014a), Cyclic microstructural transitions and fracture micromechanisms in a near equiatomic NiTi alloy, *International Journal of Fatigue,* 58, 136–143.
4. **Di Cocco V., Iacoviello F., Natali S., Volpe V.** (2014b), Fatigue crack behavior on a Cu-Zn-Al SMA, *Frattura ed Integrità Strutturale*, 30, 454–461.
5. **Freed Y., Banks-Sills L.** (2001), Crack growth resistance of shape memory alloys by means of a cohesive zone model, *Journal of the Mechanics and Physics of Solids*, 55, 2157–2180.
6. **Gall K., Tyber J., Wilkesanders G., Robertson S.W., Ritchie R.O., Maier H.J.** (2008), Effect of microstructure on the fatigue of hot-rolled and cold-drawn NiTi shape memory alloys, *Materials Science and Engineering A*, 486, 389–403.
7. **Kuribayashi K., Tsuchiya K., You Z., Tomus D., Umemoto M., Ito T., Sasaki M.** (2006), Self-deployable origami stent grafts as a biomedical application of Ni-rich TiNi shape memory alloy foil, *Materials Science and Engineering A*, 419, 131–137.
8. **Li Y.F., Mi X.J., Tan J., Gao B.D.** (2009), Thermo-mechanical cyclic transformation behavior of Ti–Ni shape memory alloy wire, *Materials Science and Engineering A*, 509, 8–13.
9. **Maletta C.** (2012), A novel fracture mechanics approach for shape memory alloys with trilinear stress-strain behavior, *International Journal of Fracture*, 177, 39–51.
10. **Maletta C., Falvo A., Furgiuele F., Leonardi A.** (2009), Stress induced martensitic transformation in the crack tip region of a NiTi alloy, *Journal of Materials Engineering and Performance*, 18, 679–685.
11. **Maletta C., Furgiuele F.** (2010), Analytical modeling of stress induced martensitic transformation in the crack tip region of nickeltitanium alloys, *Acta Materialia*, 58, 92–101.
12. **Maletta C., Furgiuele F., Sgambitterra E.** (2013), Crack tip stress distribution and stress intensity factor in shape memory alloys, *Fatigue and Fracture of Engineering Materials and Structures*, 36, 903–912.
13. **Otsuka K., Ren X.** (2005), Physical metallurgy of Ti-Ni-based shape memory alloys, *Progress in Materials Science*, 50, 511–678.
14. **Robertson S.W., Mehta A., Pelton A.R., Ritchie R.O.** (2007), Evolution of crack-tip transformation zones in superelastic Nitinol subjected to in situ fatigue: a fracture mechanics and synchrotron X-ray microdiffraction analysis, *Acta Materialia*, 55, 6198–6207.
15. **Shimamoto A., Zhao H.Y., Abe H.** (2004), Fatigue crack propagation and local crack-tip strain behavior in TiNi shape memory fiber reinforced composite, *International Journal of Fatigue*, 26, 533–542.

Fig. 4. Analytical and experimental results in terms of stress- strain relationship

In Fig. 4, the analytical stress-strain relationship is plotted together with the experimental stress-strain results. The analysis of the results indicates that the agreement between experimental and theoretical stress-strain relationship is satisfactory,

On the basis of such encouraging results, we can remark that the present model seems to be a promising engineering tool, able to describe the relationship between the fatigue behaviour and the transition phase mechanisms of SMAs with an adequate accuracy.

4. CONCLUSIONS

In the present paper, the fatigue behaviour and the phase transition mechanisms of a NiTi SMA have been examined by means of cyclic tests (up to 100 loading cycles). Miniaturised dog-bone specimens have been tested by using a customised testing machine, and the contents of both austenite and martensite phase have been experimentally measured by means of X-Ray diffraction (XRD) analyses.

On the basis of such experimental results in terms of martensite content, an analytical model has been formulated to correlate the stress-strain relationship to the phase transition mechanisms (in terms of martensite content). Five regions, characterised by different contents of austenite and martensite phase, have been identified in the stress-strain curve, for each cycle. For each of such regions, the stress – strain relationship has analytically been formulated, and the fatigue behaviour of the NiTi SMA has been evaluated.

Although the agreement between analytical and experimental results in term of stress-strain relationship has been satisfactory, further experimental tests need to be performed in order to develop a robust procedure appropriate for practical applications.

ON 3D ANTICRACK PROBLEM OF THERMOELECTROELASTICITY

Andrzej KACZYŃSKI

Faculty of Mathematics and Information Science, Warsaw University of Technology, Koszykowa 75, 00-662 Warsaw

akacz@mini.pw.edu.pl

Abstract: A solution is presented for the static problem of thermoelectroelasticity involving a transversely isotropic space with a heat-insulated rigid sheet-like inclusion (anticrack) located in the isotropy plane. It is assumed that far from this defect the body is in a uniform heat flow perpendicular to the inclusion plane. Besides, considered is the case where the electric potential on the anticrack faces is equal to zero. Accurate results are obtained by constructing suitable potential solutions and reducing the thermoelectromechanical problem to its thermomechanical counterpart. The governing boundary integral equation for a planar anticrack of arbitrary shape is obtained in terms of a normal stress discontinuity. As an illustration, a closed-form solution is given and discussed for a circular rigid inclusion.

Key words: Thermoelectroelasticity, Heat Flow, Anticrack, Singular Integral Equation, Thermal Stress Singularities

1. INTRODUCTION

Thermopiezoelectric materials are in the focus of special attention because of their potential use as functional components in many engineering applications such as sensors, actuators, smart structures, etc. (see, for instance: Rao and Sunar,1994). The main disadvantage of these materials, however, is their inherent brittleness and low fracture toughness. To promote structural mechanical reliability and lengthen service period of piezoelectric devices, thermal stress analysis is a major concern in critical design and fabrication. In particular, the presence of some original defects in structures, e.g. cracks, inclusions and voids, gives rise to high thermal stress concentration, which leads to failure of components.

Cracks (with the displacement discontinuity) and rigid lamellar inclusions called anticracks (with the traction discontinuity) represent two extreme cases of inhomogeneities that influence significantly the local fields and the overall property of the heterogeneous materials. Therefore research on these defects has great importance for structural integrity assessments.

This contribution may be treated as an extension of earlier papers (Kaczyński and Kozłowski, 2009; Kaczyński, 2014; see also extensive references therein) to the transversely isotropic thermo-piezoelectric medium. A three-dimensional problem of the determination of thermal-electric-stress state in an infinite transversely isotropic solid containing an absolutely rigid sheet-like inclusion (anticrack) in the plane of isotropy under a remote vertically uniform heat flow is considered (Fig. 1). Thermally insulated anticrack surface assumption is adopted. Moreover, the electric potential is assumed to be zero. Note that a different electric condition of electrically impermeable anticrack faces was applied in the last study by Kaczyński and Kaczyński (2017).

Problems pertinent to the present study but concerned with penny-shaped or elliptical cracks were investigated by Wang and Noda (2004), Yang et al. (2014) and Podil'chuk and Morgado (2000).

The objective of this paper is to present a general procedure for solving the posed problem and to derive the governing integral equations. Following this brief introduction, the basic equations and the potential representation of their solution are outlined in Section 2. Formulation and solution to the considered problem is given in Section 3. By using appropriate harmonic potentials, the resulting boundary-value problems involving the temperature field and induced thermal stresses are reduced to classical mixed problems of potential theory. The integro-differential and integral equations derived in the present study are, respectively, similar to the governing equations for crack and punch problems in pure elasticity. Hence, these equations can be solved by directly employing the results available in the literature. As an illustration, a complete solution expressed in elementary functions is given and discussed in Section 4 for the circularly (penny-shaped) rigid inclusion. In Section 5, the conclusions are stated.
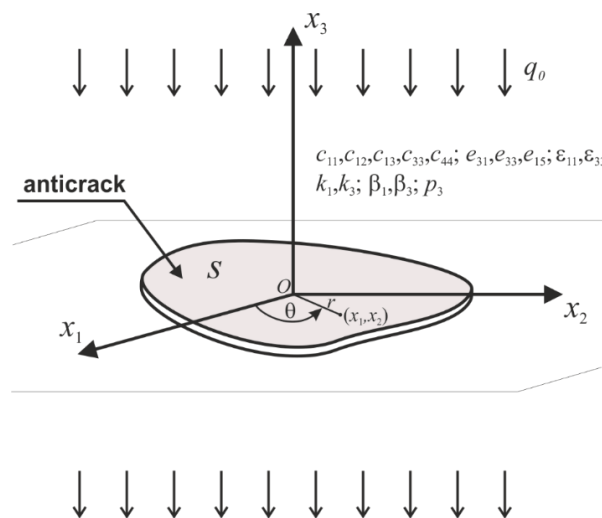

Fig. 1. An anticrack in an infinite piezoelectric medium under uniform thermal flow

2. BASIC EQUATIONS AND POTENTIAL SOLUTIONS

Let us recall the fundamental equations of piezothermoelasticity for transversely isotropic bodies of the 6mm class (the axis x_3 is directed along the axis of anisotropy, and the x_1- and x_2- axes are arbitrary oriented in the plane of isotropy) in an uncoupled static setting (Chen, 2000).

Throughout the paper, the Latin subscripts i, j are related to the Cartesian coordinates and run over 1, 2, 3, while the Greek subscripts α, γ run over 1, 2. Repeated indices imply summation and a comma denotes partial differentiation.

The constitutive relations are given by:

$$
\begin{aligned}
&\sigma_{3\alpha} = c_{44}\left(u_{\alpha,3} + u_{3,\alpha}\right) + e_{15}\,\Phi_{,\alpha}, \quad \forall \alpha \in \{1,2\} \\
&\sigma_{33} = c_{13}\,u_{\gamma,\gamma} + c_{33}\,u_{3,3} + e_{33}\,\Phi_{,3} - \beta_3\,T \\
&\sigma_{12} = c_{66}\left(u_{1,2} + u_{2,1}\right) \\
&\sigma_{11} = c_{1\gamma}\,u_{\gamma,\gamma} + c_{13}\,u_{3,3} + e_{31}\,\Phi_{,3} - \beta_1\,T \\
&\sigma_{22} = c_{1\,3-\gamma}\,u_{\gamma,\gamma} + c_{13}\,u_{3,3} + e_{31}\,\Phi_{,3} - \beta_1\,T \\
&D_\alpha = e_{15}\left(u_{\alpha,3} + u_{3,\alpha}\right) - \varepsilon_{11}\,\Phi_{,\alpha}, \quad \forall \alpha \in \{1,2\} \\
&D_3 = e_{31}\,u_{\gamma,\gamma} + e_{33}\,u_{3,3} - \varepsilon_{33}\,\Phi_{,3} + p_3\,T \\
&q_\alpha = -k_1\,T_{,\alpha}, \quad \forall \alpha \in \{1,2\}, \quad q_3 = -k_3\,T_{,3}
\end{aligned}
\tag{1}
$$

where u_i, D_i, and σ_{ij}, q_i are components of the mechanical displacement, electric displacement, and stress, heat flux, respectively; Φ is the electric potential; T is the temperature variation with $T = 0$ corresponding to a traction/electric displacement-free state; $c_{11}, c_{12}, c_{13}, c_{33}, c_{44}, c_{66} = (c_{11} - c_{12})/2$ are the elastic constants, e_{31}, e_{33}, e_{15} are the piezoelectric constants; ε_{11}, ε_{33} are the dielectric permittivities; p_3 is a pyroelectric constant in the-$x_3$direction; k_1, k_3 and β_1, β_3 are the thermal conductivity and stress-temperature coefficients, respectively.

The basic equations for thermopiezoelectricity in a stationary case without the body forces, electric charges and heat sources include the equilibrium equations, the electric equation and the heat conduction equation as follows:

$$
\sigma_{ij,j} = 0, \quad D_{i,i} = 0, \quad q_{i,i} = 0
\tag{2}
$$

Substitution of the constitutive relations (1) into (2) gives rise to a governing system of five differential equations written in the following form:

$$
\begin{aligned}
&c_{00}\,u_{\gamma,\gamma\alpha} + c_{66}\,u_{\alpha,\gamma\gamma} + c_{44}\,u_{\alpha,33} + c\,u_{3,3\alpha} + \\
&e\,\Phi_{,3\,\alpha} = \beta_1\,T_{,\alpha}, \quad \forall \alpha \in \{1,2\}
\end{aligned}
$$

$$
\begin{aligned}
&c\,u_{\gamma,\gamma3} + c_{44}\,u_{3,\gamma\gamma} + c_{33}\,u_{3,33} + e_{15}\,\Phi_{,\gamma\gamma} + \\
&e_{33}\,\Phi_{,33} = \beta_3\,T_{,3}
\end{aligned}
\tag{3a}
$$

$$
\begin{aligned}
&e\,u_{\gamma,\gamma3} + e_{15}\,u_{3,\gamma\gamma} + e_{33}\,u_{3,33} - \varepsilon_{11}\,\Phi_{,\gamma\gamma} - \\
&\varepsilon_{33}\,\Phi_{,33} = -p_3\,T_{,3}
\end{aligned}
$$

$$
T_{,\gamma\gamma} + k_0^{-2}\,T_{,33} = 0
\tag{3b}
$$

The notation for some combinations of material constants has been introduced:

$$
\begin{aligned}
&c_{00} = (c_{11} + c_{12})/2, \quad c = c_{13} + c_{44}, \quad e = e_{15} + e_{31}, \\
&k_0 = \sqrt{k_1/k_3}, \quad C^2 = c_{11}c_{33} - c_{13}(c_{13} + 2c_{44})
\end{aligned}
\tag{4}
$$

The general potential solutions to Eqs. (3b) and (3a) proposed by Kaczyński and Kaczyński (2017) are (see Appendix A):

$$
T(x_1, x_2, x_3) = -\left.\frac{\partial^2 \omega(x_1, x_2, z_0)}{\partial z_0^2}\right|_{z_0 = k_0 x_3} \equiv -\omega_{,z_0 z_0}
\tag{5}
$$

$$
u_\alpha = (\psi_1 + \psi_2 + \psi_3)_{,\alpha} + (-1)^\alpha\,\psi_{,3-\alpha} + c_1\,\omega_{,\alpha},
$$
$$
\forall \alpha \in \{1,2\}
\tag{6a}
$$

$$
u_3 = m_i\,s_i\,\psi_{i,z_i} - c_2 k_0\,\omega_{,z_0}
$$

$$
\Phi = l_i s_i\,\psi_{i,z_i} - c_3 k_0\,\omega_{,z_0}
\tag{6b}
$$

where ω, ψ_i $(i \in \{1,2,3\})$, ψ are five harmonic functions in the corresponding coordinate systems (x_1, x_2, z_k), $z_k = s_k x_3$, i.e.,

$$
\nabla_{z_0}^2 \omega = 0, \quad \nabla_{z_i}^2 \psi_i = 0, \quad \forall i \in \{1,2,3\}, \quad \nabla_{z_4}^2 \psi = 0
$$

$$
\left(\begin{array}{c}
\nabla_{z_k}^2(\cdot) \equiv (\cdot)_{,\gamma\gamma} + (\cdot)_{,z_k z_k} = \Delta(\cdot) + (\cdot)_{,z_k z_k}, \\
\forall k \in \{0,1,2,3,4\}
\end{array}\right),
\tag{7}
$$

$s_0 = k_0$, $s_4 = \sqrt{c_{66}/c_{44}}$, s_1, s_2, s_3 are the roots with the positive real part of the following algebraic equation:

$$
a_0\,s^6 - b_0\,s^4 + c_0 s^2 - d_0 = 0
\tag{8}
$$

Substituting Eqs. (5) and (6a-b) into (1), one can derive the potential expressions for the components of stress and electric displacement as follows:

$$
\begin{aligned}
\sigma_{3\alpha} &= a_i s_i\,\psi_{i,z_i\alpha} + \delta_1\,\omega_{,z_0\,\alpha} + \\
&\quad + (-1)^\alpha s_4\,c_{44}\,\psi_{,z_4\,3-\alpha}, \quad \forall \alpha \in \{1,2\} \\
\sigma_{33} &= a_i\,\psi_{i,z_i z_i} - \delta_3\,\omega_{,z_0 z_0} \\
\sigma_{12} &= c_{66}\big[2(\psi_1 + \psi_2 + \psi_3 + c_1\,\omega)_{,12} + \psi_{,11} - \psi_{,22}\big] \\
\sigma_{11} &= -a_i s_i^2\,\psi_{i,z_i z_i} - \delta_0\,\omega_{,z_0 z_0} + \\
&\quad -2c_{66}\big[(\psi_1 + \psi_2 + \psi_3)_{,22} + \psi_{,12} + c_1\,\omega_{,22}\big] \\
\sigma_{22} &= -a_i s_i^2\,\psi_{i,z_i z_i} - \delta_0\,\omega_{,z_0 z_0} + \\
&\quad -2c_{66}\big[(\psi_1 + \psi_2 + \psi_3)_{,11} - \psi_{,12} + c_1\,\omega_{,11}\big] \\
D_\alpha &= d_i s_i\,\psi_{i,z_i\alpha} + \tau_1\,\omega_{,z_0\,\alpha} + \\
&\quad + (-1)^\alpha s_4\,e_{15}\,\psi_{,z_4\,3-\alpha}, \quad \forall \alpha \in \{1,2\} \\
D_3 &= d_i\,\psi_{i,z_i z_i} - \tau_3\,\omega_{,z_0 z_0}
\end{aligned}
\tag{9}
$$

It is noted that the above general potential representation is valid only in the case of distinct material eigenvalues s_k ($k \in \{0,1,2,3,4\}$).

3. PROBLEM FORMULATION AND SOLUTION

Consider an infinite transversely isotropic thermopiezoelectric body that is weakened by a heat-insulated rigid inclusion (anticrack), which occupies a bounded plane area S with a smooth profile in the isotropy plane $x_3 = 0$. There is a constant heat flux $q(\infty) = [0,0,-q_0]$, $q_0 > 0$ in the direction of the negative x_3 – symmetry axis (Fig. 1).

We deal with the boundary-value problem: find fields T and u_i suitable smooth on $\mathrm{R}^3 - S$ such that Eqs. (3b), (3a) and (9) hold, subject to the following global boundary conditions:

– thermal conditions at infinity (perpendicular flow of uniform heat)

$$
q_1 = q_2 = 0, \quad q_3 = -k_3\,T_{,3} = -q_0
\tag{10}
$$

– stress and electric-free state at infinity

$$
\sigma_{ij} = 0, \quad D_i = 0
\tag{11}
$$

− mechanical conditions on S (displacement free surfaces with a small vertical rigid-body translation ε)

$$u_1 = u_2 = 0, \quad u_3 = \varepsilon \tag{12}$$

− thermally insulated surfaces of S

$$q_3 = -k_3\, T_{,3} = 0 \tag{13}$$

− vanishing of electric potential on S

$$\Phi = 0 \tag{14}$$

Moreover, the parameter ε will be found in solving the problem from the equilibrium condition:

$$\iint_S [\sigma_{33}(x_1, x_2, 0^+) - \sigma_{33}(x_1, x_2, 0^-)]\ dx_1\, dx_2 = 0 \tag{15}$$

Making use of the superposition principle, we construct the solution of the above anticrack boundary-value problem as a sum of two components, namely:

$$T = \overset{0}{T} + \tilde{T}, \quad u_i = \overset{0}{u_i} + \tilde{u}_i, \quad \sigma_{ij} = \overset{0}{\sigma_{ij}} + \tilde{\sigma}_{ij},$$
$$\Phi = \overset{0}{\Phi} + \tilde{\Phi}, \quad D_i = \overset{0}{D_i} + \tilde{D}_i \tag{16}$$

where the components attached by 0 describe the basic state of defect-free solid, and the components with the tilde represent the perturbations due to the anticrack.

The results for the first 0-problem are found to be given by:

$$\overset{0}{T}(x_1, x_2, x_3) = \frac{q_0}{k_3}$$
$$\overset{0}{u_\alpha} = \frac{q_0}{k_3} n_\alpha x_\alpha x_3, \ \forall\, \alpha \in \{1,2\}$$
$$\overset{0}{u_3} = \frac{q_0}{2k_3}[n_2 x_3^2 - n_1(x_1^2 + x_2^2)] \tag{17}$$
$$\overset{0}{\sigma_{ij}} = 0, \quad \overset{0}{\Phi} = -\frac{q_0}{2k_3} n_3 x_3^2, \quad \overset{0}{D_i} = 0$$

where the constants n_i are determined from the following linear system of equations:

$$\begin{bmatrix} 2c_{00} & c_{13} & -e_{31} \\ 2c_{13} & c_{33} & -e_{33} \\ 2e_{31} & e_{33} & \varepsilon_{33} \end{bmatrix} \begin{bmatrix} n_1 \\ n_2 \\ n_3 \end{bmatrix} = \begin{bmatrix} \beta_1 \\ \beta_3 \\ -p_3 \end{bmatrix} \tag{18}$$

Attention will be drawn next on the corrective solution of the perturbed problem.

The disturbing thermal field $\tilde{T}$, which is odd in x_3 and vanishes at infinity, is determined by solving Eq. (3b) in the half-space $x_3 \geq 0$ with the following boundary conditions:

$$\tilde{T}_{,3} = -\frac{q_0}{k_3}, \quad \forall (x_1, x_2, x_3 = 0^+) \in S$$
$$\tilde{T} = 0, \quad \forall (x_1, x_2, x_3 = 0^+) \in R^2 - S \tag{19}$$

According to (5) and using the potential theory (Kellogg, 1953), the solution is written via the thermal potential $\tilde{\omega}(x_1, x_2, z_0)$ as $\tilde{T}(x_1, x_2, x_3) = -\tilde{\omega}_{,z_0 z_0}$, $z_0 = k_0 x_3$ by assuming that:

$$\tilde{\omega}(x_1, x_2, z_0) = \iint_S \ln(R_0 + z_0)\, \gamma(\xi_1, \xi_2)\ d\xi_1\, d\xi_2$$
$$\left(R_0 = |\mathbf{x}_0 - \boldsymbol{\xi}| = \sqrt{(x_1 - \xi_1)^2 + (x_2 - \xi_2)^2 + z_0^2}\right)$$
$$\tilde{T}(x_1, x_2, x_3) = -\frac{\partial}{\partial z_0} \iint_S \frac{\gamma(\xi_1, \xi_2)\ d\xi_1\, d\xi_2}{R_0} \tag{20}$$
$$\tilde{T}_{,3} = -k_0 \frac{\partial^2}{\partial z_0^2} \iint_S \frac{\gamma(\xi_1, \xi_2)\ d\xi_1\, d\xi_2}{R_0} = k_0\, \Delta \iint_S \frac{\gamma(\xi_1, \xi_2)\ d\xi_1\, d\xi_2}{R_0}$$

and the unknown density γ, in view of Eq. (19)$_1$, satisfies the integro-differential singular equation of Newton's potential type:

$$\Delta \iint_S \frac{\gamma(\xi_1, \xi_2)\ d\xi_1\, d\xi_2}{\sqrt{(x_1 - \xi_1)^2 + (x_2 - \xi_2)^2}} = -\frac{q_0}{\sqrt{k_1 k_3}} \tag{21}$$

It is interesting to note that this equation has a similar form as that arising in Mode I crack problem. Moreover, the desired temperature has a jump on S:

$$\tilde{T}(x_1, x_2, 0^+) - \tilde{T}(x_1, x_2, 0^-) = 4\pi\, \gamma(x_1, x_2),$$
$$(x_1, x_2) \in S \tag{22}$$

We proceed now to the associated problem of electroelasticity that is governed by Eqs. (3a) and (9) with the unknown quantities marked by the tilde. Because of the anti-symmetry of the temperature and stress system, and bearing in mind Eqs. (16),(17),(12),(14) and the resulting conditions for the displacements and electric potential (i.e., $\tilde{u}_1$, $\tilde{u}_2$, $\tilde{D}_3$ are odd in x_3, and $\tilde{u}_3$, $\tilde{\Phi}$ are even in x_3), the anticrack perturbed problem may be formulated as a mixed problem over a half-space $x_3 \geq 0$ with the following boundary conditions:

$$\tilde{u}_\alpha(x_1, x_2, x_3 = 0^+) = 0, \quad \forall (x_1, x_2) \in R^2 \quad (\alpha = 1,\ 2)$$
$$\tilde{u}_3(x_1, x_2, x_3 = 0^+) = \frac{q_0\, n_1}{2k_3}(x_1^2 + x_2^2) + \varepsilon, \ \forall (x_1, x_2) \in S$$
$$\tilde{\sigma}_{33}(x_1, x_2, x_3 = 0^+) = 0, \quad \forall (x_1, x_2) \in R^2 - S$$
$$\tilde{\Phi}(x_1, x_2, x_3 = 0^+) = 0, \quad \forall (x_1, x_2) \in S \tag{23}$$
$$\tilde{u}_i = O\left(|x|^{-1}\right) \ as \ |x| = \sqrt{x_1^2 + x_2^2 + x_3^2} \to \infty$$

For the solution of this boundary-value problem we use the potential function approach based on the construction of the potentials in the general solution (6) and (9) with the knowledge of the thermal potential $\tilde{\omega}(x_1, x_2, z_0)$ well suited to the boundary conditions (23). It is expedient to make the assumptions:

$$\psi_i(x_1, x_2, z_i) = \tilde{b}_i\, \tilde{f}(x_1, x_2, z_i) + \tilde{A}_i\, \tilde{\omega}(x_1, x_2, z_i),$$
$$\forall\, i \in \{1,2,3\} \tag{24}$$
$$\psi(x_1, x_2, z_4) \equiv 0$$

with

$$\tilde{b}_1 = l_3 s_3 - l_2 s_2, \quad \tilde{b}_2 = l_1 s_1 - l_3 s_3,$$
$$\tilde{b}_3 = l_2 s_2 - l_1 s_1 \tag{25}$$

Here, $\tilde{f}(x_1, x_2, x_3)$ is an unknown harmonic function and $\tilde{A}_1$, $\tilde{A}_2$, $\tilde{A}_3$ are constants to be determined.

Making use of equations (9) and (6b), the desired field components become:

$$\tilde{u}_\alpha = \tilde{b}_i\left[\tilde{f}(x_1, x_2, z_i)\right]_{,\alpha} + \tilde{A}_i[\tilde{\omega}(x_1, x_2, z_i)]_{,\alpha}$$
$$\quad + c_1\left[\tilde{\omega}(x_1, x_2, z_0)\right]_{,\alpha}, \ \forall\, \alpha \in \{1,2\}$$
$$\tilde{u}_3 = m_i s_i \tilde{b}_i\left[\tilde{f}(x_1, x_2, z_i)\right]_{,z_i} + m_i s_i \tilde{A}_i[\tilde{\omega}(x_1, x_2, z_i)]_{,z_i}$$
$$\quad - c_2 k_0\left[\tilde{\omega}(x_1, x_2, z_0)\right]_{,z_0}$$
$$\tilde{\Phi} = l_i s_i \tilde{b}_i\left[\tilde{f}(x_1, x_2, z_i)\right]_{,z_i} + l_i s_i \tilde{A}_i[\tilde{\omega}(x_1, x_2, z_i)]_{,z_i}$$
$$\quad - c_3 k_0\left[\tilde{\omega}(x_1, x_2, z_0)\right]_{,z_0} \tag{26}$$
$$\tilde{\sigma}_{3\alpha} = a_i s_i \tilde{b}_i\left[\tilde{f}(x_1, x_2, z_i)\right]_{,z_i \alpha} + a_i s_i \tilde{A}_i\left[\tilde{\omega}(x_1, x_2, z_i)\right]_{,z_i \alpha}$$
$$\quad + \delta_1\left[\tilde{\omega}(x_1, x_2, z_0)\right]_{,z_0 \alpha}, \quad \forall\, \alpha \in \{1,2\}$$
$$\tilde{\sigma}_{33} = a_i \tilde{b}_i\left[\tilde{f}(x_1, x_2, z_i)\right]_{,z_i z_i} + a_i \tilde{A}_i\left[\tilde{\omega}(x_1, x_2, z_i)\right]_{,z_i z_i}$$
$$\quad - \delta_3\left[\tilde{\omega}(x_1, x_2, z_0)\right]_{,z_0 z_0}$$
$$\tilde{D}_\alpha = d_i s_i \tilde{b}_i\left[\tilde{f}(x_1, x_2, z_i)\right]_{,z_i \alpha} + d_i s_i \tilde{A}_i\left[\tilde{\omega}(x_1, x_2, z_i)\right]_{,z_i \alpha}$$
$$\quad + \tau_1\left[\tilde{\omega}(x_1, x_2, z_0)\right]_{,z_0 \alpha}, \ \forall\, \alpha \in \{1,2\}$$
$$\tilde{D}_3 = d_i \tilde{b}_i\left[\tilde{f}(x_1, x_2, z_i)\right]_{,z_i z_i} + d_i \tilde{A}_i\left[\tilde{\omega}(x_1, x_2, z_i)\right]_{,z_i z_i}$$
$$\quad - \tau_3\left[\tilde{\omega}(x_1, x_2, z_0)\right]_{,z_0 z_0}$$

The expressions in the above equations simplify on the plane $x_3 = 0^+$ (where $z_1 = z_2 = z_3 = z_0 = 0^+$) to the following:

$$\tilde{u}_\alpha = \left(\tilde{A}_1 + \tilde{A}_2 + \tilde{A}_3 + c_1\right)\left[\frac{\partial\,\tilde{\omega}(x_1, x_2, z_0)}{\partial x_\alpha}\right]_{z_0 = 0},$$

$$\forall\,\alpha \in \{1,2\}$$

$$\tilde{u}_3 = m_i s_i \tilde{b}_i \left[\frac{\partial \tilde{f}(x_1, x_2, x_3)}{\partial x_3}\right]_{x_3 = 0^+}$$

$$+ \left(m_i s_i \tilde{A}_i - c_2 k_0\right)\left[\frac{\partial\,\tilde{\omega}(x_1, x_2, z_0)}{\partial z_0}\right]_{z_0 = 0}$$

$$\tilde{\Phi} = l_i s_i \tilde{b}_i \left[\frac{\partial \tilde{f}(x_1, x_2, x_3)}{\partial x_3}\right]_{x_3 = 0^+}$$

$$+ \left(l_i s_i \tilde{A}_i - c_3 k_0\right)\left[\frac{\partial\,\tilde{\omega}(x_1, x_2, z_0)}{\partial z_0}\right]_{z_0 = 0}$$

$$\tilde{\sigma}_{33} = a_i \tilde{b}_i \left[\frac{\partial^2 \tilde{f}(x_1, x_2, x_3)}{\partial x_3^2}\right]_{x_3 = 0^+}$$

$$+ \left(a_i \tilde{A}_i - \delta_3\right)\left[\frac{\partial^2 \tilde{\omega}(x_1, x_2, z_0)}{\partial z_0^2}\right]_{z_0 = 0^+} \tag{27}$$

$$\tilde{D}_3 = d_i \tilde{b}_i \left[\frac{\partial^2 \tilde{f}(x_1, x_2, x_3)}{\partial x_3^2}\right]_{x_3 = 0^+}$$

$$+ \left(d_i \tilde{A}_i - \tau_3\right)\left[\frac{\partial^2 \tilde{\omega}(x_1, x_2, z_0)}{\partial z_0^2}\right]_{z_0 = 0^+}$$

The three unknown constants $\tilde{A}_1$, $\tilde{A}_2$, $\tilde{A}_3$ are to be determined from the following linear system of equations:

$$\begin{bmatrix} 1 & 1 & 1 \\ l_1 s_1 & l_2 s_2 & l_3 s_3 \\ a_1 & a_2 & a_3 \end{bmatrix}\begin{bmatrix} \tilde{A}_1 \\ \tilde{A}_2 \\ \tilde{A}_3 \end{bmatrix} = \begin{bmatrix} -c_1 \\ c_3 k_0 \\ \delta_3 \end{bmatrix} \tag{28}$$

A glance at equations (23) and (27) reveals now that the potential $\tilde{f}$ is governed by:
– for $(x_1, x_2) \in S$

$$m_i s_i \tilde{b}_i \left[\frac{\partial \tilde{f}(x_1, x_2, x_3)}{\partial x_3}\right]_{x_3 = 0^+} = r(x_1, x_2) \tag{29}$$

– for $(x_1, x_2) \in R^2 - S$

$$\left[\frac{\partial^2 \tilde{f}(x_1, x_2, x_3)}{\partial x_3^2}\right]_{x_3 = 0^+} = 0 \tag{30}$$

where:

$$r(x_1, x_2) = \tilde{\beta}\left[\frac{\partial\,\tilde{\omega}(x_1, x_2, z_0)}{\partial z_0}\right]_{z_0 = 0} + \frac{q_0 n_1}{2 k_3}(x_1^2 + x_2^2) + \varepsilon \tag{31}$$

with the following constant:

$$\tilde{\beta} = c_2 k_0 - m_i s_i \tilde{A}_i \tag{32}$$

A well-known solution to this classical boundary problem in potential theory (Kellogg, 1953) may be written as follows:

$$\tilde{f}(x_1, x_2, x_3) =$$

$$\frac{-1}{2\pi\, a_i \tilde{b}_i} \iint_S \tilde{\sigma}_{33}(\xi_1, \xi_2, 0^+)\ln\left(R_\xi + x_3\right) d\xi_1\, d\xi_2$$

$$\left(R_\xi = \sqrt{(x_1 - \xi_1)^2 + (x_2 - \xi_2)^2 + x_3^2}\right) \tag{33}$$

Now enforcing the displacement boundary condition (29), we arrive at the governing two-dimensional singular integral equation of Newtonian potential type to determine the normal stress $\tilde{\sigma}_{33}^+ \equiv \tilde{\sigma}_{33}(x_1, x_2, 0^+)$ on the upper side of S:

$$\tilde{B}\iint_S \frac{\tilde{\sigma}_{33}^+(\xi_1, \xi_2)\, d\xi_1\, d\xi_2}{\sqrt{(x_1 - \xi_1)^2 + (x_2 - \xi_2)^2}} = -\tilde{r}(x_1, x_2), \tag{34}$$

$$\forall(x_1, x_2) \in S$$

where the constant $\tilde{B}$ is given by:

$$\tilde{B} = \frac{m_i s_i \tilde{b}_i}{2\pi\, a_i \tilde{b}_i} \tag{35}$$

Then, having obtained the distribution of the normal stress in the region S, the unknown rigid translation ε can be calculated from Eq. (15) transformed to the following form:

$$\iint_S \tilde{\sigma}_{33}^+(x_1, x_2)\; dx_1\, dx_2 = 0 \tag{36}$$

Moreover, the main potential $\tilde{f}$ is found from Eq. (33) and the whole perturbed electroelastic fields can be obtained from relations (26).

It is worth mentioning that for a rigid inclusion with an arbitrary shape S, the derived governing equations (21) and (34) generally can be solved by numerical methods. However, analytical solutions to these equations are available when the anticrack is in the form of an ellipse (Rahman, 2002). For illustration, a solution will be presented for a rigid circularly shaped inclusion in the next section.

4. EXAMPLE: CIRCULAR ANTICRACK IN A UNIFORM HEAT FLOW

Let the anticrack is located at the circular region in the $x_1 O x_2$-plane, i.e.,

$$S = \{(x_1 = r\cos\theta, x_2 = r\sin\theta, x_3 = 0):$$
$$0 \le r = \sqrt{x_1^2 + x_2^2} \le a \;\land\; 0 \le \theta \le 2\pi\} \tag{37}$$

Following along the same line of reasoning as that used in the corresponding antisymmetric anticrack problems (Kaczyński, 2014), it is possible to obtain in this case a complete solution expressed in elementary functions due to the results of advanced method in potential theory, reported by Fabrikant (1989, 1991). Only the final results will be presented.

Accordingly, the axially-symmetric solution to the thermal problem is given by:

$$\gamma(x_1, x_2) = \tilde{\gamma}(r) = \frac{q_0}{\pi^2 \sqrt{k_1 k_3}} \sqrt{a^2 - r^2},$$

$$0 \le r \le a$$

$$\frac{\partial\,\tilde{\omega}(r, z_0)}{\partial x_\alpha} = \frac{q_0\, x_\alpha}{\pi \sqrt{k_1 k_3}}\left[-x_3 \sin^{-1}\frac{a}{l_{20}} + \right.$$

$$\left. + \left(\sqrt{a^2 - l_{10}^2}\left(1 - \frac{l_{10}^2 + 2a^2}{3r^2}\right) + \frac{2a^3}{3r^2}\right)\right], \forall\,\alpha \in \{1,2\}$$

$$\frac{\partial\,\tilde{\omega}(r, z_0)}{\partial z_0} = \frac{q_0}{2\pi \sqrt{k_1 k_3}}\left[(2a^2 + 2z_0^2 - r^2)\sin^{-1}\frac{a}{l_{20}}\right.$$

$$\left. - \frac{(2a^2 - 3l_{10}^2)}{a}\sqrt{l_{20}^2 - a^2}\right], \qquad z_0 \ge 0 \tag{38}$$

$$\tilde{T}(r, z_0) = -\frac{\partial^2 \tilde{\omega}}{\partial z_0^2} =$$

$$-\frac{2\, q_0}{\pi \sqrt{k_1 k_3}}\left(z_0 \sin^{-1}\frac{a}{l_{20}} - \sqrt{a^2 - l_{10}^2}\right), z_0 \ge 0$$

where Fabrikant's notation is given below:

$$l_1 \equiv l_1(a,r,x_3) =$$
$$\frac{1}{2}\left[\sqrt{(r+a)^2 + x_3^2} - \sqrt{(r-a)^2 + x_3^2}\right]$$

$$l_2 \equiv l_2(a,r,x_3) =$$
$$\frac{1}{2}\left[\sqrt{(r+a)^2 + x_3^2} + \sqrt{(r-a)^2 + x_3^2}\right]$$

(39)

$$l_{10} = l_1(a,r,z_0), \quad l_{20} = l_2(a,r,z_0)$$

along with the following properties:

$$[l_1]_{x_3=0} = [l_{10}]_{z_0=0} = \min(a,r)$$
$$[l_2]_{x_3=0} = [l_{20}]_{z_0=0} = \max(a,r)$$

(40)

In turn, the analytical solution to the governing equation (34) is:

$$\tilde{\sigma}_{33}^+(r) = \frac{\beta_3^{(ep)} q_0}{\pi}\frac{2a^2 - 3r^2}{\sqrt{a^2 - r^2}}, \qquad 0 \le r < a$$

(41)

where (see Eqs.(18) and (32)):

$$\beta_3^{(ep)} = \frac{2a_i\tilde{b}_i}{3m_j s_j \tilde{b}_j}\left(\frac{2n_1}{k_3} - \frac{\tilde{\beta}}{\sqrt{k_1 k_3}}\right)$$

(42)

and the vertical rigid displacement is found as:

$$\varepsilon = -\frac{a^2 q_0}{3}\left(\frac{\tilde{\beta}}{\sqrt{k_1 k_3}} + \frac{n_1}{k_3}\right)$$

(43)

The primary harmonic potential for the electroelastic perturbed problem is obtained by calculating integral (32) with the use of Eq. (40). As a result, we find that for $x_3 \ge 0$:

$$\tilde{f}(x_1, x_2, x_3) =$$
$$-\frac{\beta_3^{(ep)} q_0}{2\pi^2 a_i \tilde{b}_i}\left[x_3 \sin^{-1}\frac{a}{l_2}\left(a^2 - \frac{3}{2}r^2 + x_3^2\right) + \right.$$
$$\left. + \sqrt{a^2 - l_1^2}\left(5r^2 + \frac{1}{3}a^2 - l_2^2 - \frac{11}{6}l_1^2\right)\right]$$

(44)

and

$$\frac{\partial\tilde{f}(x_1, x_2, x_3)}{\partial x_3} =$$
$$-\frac{\beta_3^{(ep)} q_0}{2\pi a_i \tilde{b}_i}\left[\left(a^2 - \frac{3}{2}r^2 + 3x_3^2\right)\sin^{-1}\frac{a}{l_2} + \right.$$
$$\left. - \frac{3(2a^2 - 3l_1^2)\sqrt{l_2^2 - a^2}}{2a}\right]$$

(45)

$$\frac{\partial^2\tilde{f}(x_1, x_2, x_3)}{\partial x_3^2} =$$
$$-\frac{\beta_3^{(ep)} q_0}{\pi a_i \tilde{b}_i}\left[3x_3\sin^{-1}\frac{a}{l_2} - 3\sqrt{a^2 - l_1^2} + \frac{a^2\sqrt{a^2 - l_1^2}}{l_2^2 - l_1^2}\right]$$

Having the exact expressions for the governing harmonic functions and their derivatives as shown in Eqs. (45) and (38), the full –space piezothermoelastic field can be obtained simply from formulas (26). The derivation is omitted here to save the space of the paper. To investigate the singular behaviour of the thermal-electric-stress field near the disc edge, however, the solution in the inclusion plane $x_3 = 0^\pm$ is given below:

$$T(r, 0^\pm) = \begin{cases} \pm\dfrac{2q_0}{\pi\sqrt{k_1 k_3}}\sqrt{a^2 - r^2} & 0 \le r \le a \\ 0 & r > a \end{cases}$$

$$q_r(r, 0^\pm) = -k_1\frac{\partial T(r, 0^\pm)}{\partial r} =$$
$$= \begin{cases} \pm\dfrac{2q_0}{\pi}\sqrt{\dfrac{k_1}{k_3}}\dfrac{r}{\sqrt{a^2 - r^2}} & 0 \le r \le a \\ 0 & r > a \end{cases}$$

(46)

$$q_3(r, 0^\pm) = -k_3 T_{,3}(r, 0^\pm) =$$
$$= \begin{cases} 0 & 0 \le r < a \\ \dfrac{2q_0}{\pi}\left(\sin^{-1}\dfrac{a}{r} - \dfrac{a}{\sqrt{r^2 - a^2}}\right) - q_0 & r > a \end{cases}$$

$$u_1(r, 0^\pm) = u_2(r, 0^\pm) = 0 \qquad 0 \le r < \infty$$

$$u_3(r, 0^\pm) = \begin{cases} \varepsilon & 0 \le r < a \\ \dfrac{2}{\pi}\left(\varepsilon + \dfrac{q_0 n_1}{2 k_3}r^2\right)\sin^{-1}\dfrac{a}{r} + \\ -\dfrac{q_0 n_1}{\pi k_3}\sqrt{r^2 - a^2} - \dfrac{q_0 n_1}{2 k_3}r^2 & r > a \end{cases}$$

$$\sigma_{33}(r, 0^\pm) = \begin{cases} \pm\dfrac{\beta_3^{(ep)} q_0}{\pi}\dfrac{2a^2 - 3r^2}{\sqrt{a^2 - r^2}} & 0 \le r < a \\ 0 & r > a \end{cases}$$

(47)

$$\sigma_{3r}(r, 0^\pm) = \sigma_{31}(r, 0^\pm)\cos\theta + \sigma_{32}(r, 0^\pm)\sin\theta =$$
$$= \begin{cases} \beta^{(ep)} q_0 r & 0 \le r < a \\ \dfrac{2q_0}{\pi}\left(\beta^{(ep)} r\sin^{-1}\dfrac{a}{r} - \dfrac{\beta_r^{(ep)} a^3}{r\sqrt{r^2 - a^2}} - \dfrac{\beta^{(ep)} a\sqrt{r^2 - a^2}}{r}\right) & r > a \end{cases}$$

$$\Phi(r, 0^\pm) = 0 \qquad 0 \le r < \infty$$

$$D_r(r, 0^\pm) = D_1(r, 0^\pm)\cos\theta + D_2(r, 0^\pm)\sin\theta =$$
$$= \begin{cases} \tilde{\beta}^{(ep)} q_0 r & 0 \le r < a \\ \dfrac{2q_0}{\pi}\left(\tilde{\beta}^{(ep)} r\sin^{-1}\dfrac{a}{r} - \dfrac{\tilde{\beta}_r^{(ep)} a^3}{r\sqrt{r^2 - a^2}} - \dfrac{\tilde{\beta}^{(ep)} a\sqrt{r^2 - a^2}}{r}\right) & r > a \end{cases}$$

(48)

$$D_3(r, 0^\pm) =$$
$$= \begin{cases} \pm\dfrac{q_0}{\pi}\left[\dfrac{\beta_d^{(ep)}(2a^2 - 3r^2)}{\sqrt{a^2 - r^2}} - \dfrac{2(d_i\tilde{A}_i - \tau_3)}{\sqrt{k_1 k_3}}\sqrt{a^2 - r^2}\right] & 0 \le r < a \\ 0 & r > a \end{cases}$$

where:

$$\beta^{(ep)} = \frac{3\beta_3^{(ep)} a_j s_j \tilde{b}_j}{4 a_i \tilde{b}_i} - \frac{(a_k s_k \tilde{A}_k + \delta_1)}{2\sqrt{k_1 k_3}}$$

$$\beta_r^{(ep)} = \frac{a_j s_j \tilde{b}_j}{3m_i s_i \tilde{b}_i}\left(\frac{2n_1}{k_3} - \frac{\tilde{\beta}}{\sqrt{k_1 k_3}}\right)$$

$$\tilde{\beta}^{(ep)} = \frac{3\beta_3^{(ep)} d_j s_j \tilde{b}_j}{4 d_i \tilde{b}_i} - \frac{(d_k s_k \tilde{A}_k + \tau_1)}{2\sqrt{k_1 k_3}}$$

(49)

$$\tilde{\beta}_r^{(ep)} = \frac{d_j s_j \tilde{b}_j}{3 m_i s_i \tilde{b}_i}\left(\frac{2n_1}{k_3} - \frac{\tilde{\beta}}{\sqrt{k_1 k_3}}\right)$$

$$\beta_d^{(ep)} = \frac{d_j \tilde{b}_j}{a_i \tilde{b}_i}\beta_3^{(ep)}$$

Analyzing the above expressions, we reveal that

1. The anticrack S obstructs locally the heat flow, producing the jump of temperature and the drastic change of its gradient on the surface near the anticrack front.

2. The normal stress σ_{33} and electric displacement D_3 suffer jumps across S and exhibit the inverse square-root singularity at $r = a^-$. This indicates a mechanism of failure in the form of material separation from the surface of the rigid inclusion

described by the stress and electric displacement singularity coefficients given by:

$$S_I^{\pm} = \lim_{r \to a^-}\sqrt{2\pi(a-r)}\,\sigma_{33}(r,0^{\pm}) =$$
$$\mp\frac{\beta_3^{(ep)}q_0\,a\sqrt{a}}{\sqrt{\pi}}$$

$$S_I^{\pm(ed)} = \lim_{r \to a^-}\sqrt{2\pi(a-r)}\,D_3(r,0^{\pm}) =$$
$$\mp\frac{\beta_d^{(ep)}q_0\,a\sqrt{a}}{\sqrt{\pi}}$$

(50)

3. Another mechanism controlling the material cracking around the anticrack front is Mode II (edge-sliding) described by the thermal and electric stress intensity factors:

$$K_{II}^{(e)} = \lim_{r \to a^+}\sqrt{2\pi(r-a)}\,\sigma_{3\,r}(r,0)$$
$$= -\frac{2\,\beta_r^{(ep)}q_0\,a\sqrt{a}}{\sqrt{\pi}}$$

$$K_{II}^{(ed)} = \lim_{r \to a^+}\sqrt{2\pi(r-a)}\,D_r(r,0)$$
$$= -\frac{2\,\tilde{\beta}_r^{(ep)}q_0\,a\sqrt{a}}{\sqrt{\pi}}$$

(51)

These parameters can be used in conjunction with a suitable force criterion of fracture.

5. CONCLUSIONS

The three-dimensional thermal stress problem for an insulated rigid inclusion obstructing a uniform heat flux in an infinite linear transversely isotropic thermopiezoelectric medium has been investigated. The case where the electric potential on the anticrack surface is equal to zero was considered. Using the potential function method, the problem involving the inclusion of arbitrary shape has been reduced to classical boundary problems of potential theory. Specifically, with the knowledge of the steady-state temperature distribution, the governing equation was derived, which is similar to that reported in the literature on contact problems in elasticity. In particular, for a circularly shaped inclusion, the solution was obtained in terms of elementary functions. Exact expressions for the thermo-electro-elastic field at the plane of anticrack surface were derived and interpreted from the point of view of linear fracture mechanics. The results obtained are new to the literature and can serve as a benchmark to various numerical analysis.

Appendix A

The material coefficients in characteristic equation (8) are as follows (see (4)):

$$a_0 = c_{44}(c_{33}\,\varepsilon_{33} + e_{33}^2)$$
$$+e_{33}(2c_{44}e_{15} + c_{11}e_{33} - 2\,c\,e)$$

$$b_0 = c_{33}(c_{44}\,\varepsilon_{11} + e^2) + \varepsilon_{33}\,C^2$$
$$+e_{33}(2c_{44}e_{15} + c_{11}e_{33} - 2\,c\,e)$$

$$c_0 = c_{44}(c_{11}\,\varepsilon_{33} + e^2) + \varepsilon_{11}\,C^2$$
$$+e_{15}(2c_{11}e_{33} + c_{44}e_{15} - 2\,c\,e)$$

$$d_0 = c_{11}(c_{44}\,\varepsilon_{11} + e_{15}^2)$$

According to Kaczyński and Kaczyński (2017), material constants appearing in representations (6) and (9) are listed below:

$$m_i = \frac{-c_{44}\,e_{33}\,s_i^4 + (c_{11}e_{33} + c_{44}e_{15} - c\,e)\,s_i^2 - c_{11}\,e_{15}}{s_i^2[(c\,e_{33} - e\,c_{33})s_i^2 - (c\,e_{15} - e\,c_{44})]}$$

$$l_i = \frac{c_{44}\,c_{33}\,s_i^4 - (C^2 - 2c_{44}^2)\,s_i^2 + c_{11}\,c_{44}}{s_i^2[(c\,e_{33} - e\,c_{33})s_i^2 - (c\,e_{15} - e\,c_{44})]}$$

$$a_i = c_{44}(1 + m_i) + e_{15}\,l_i$$
$$d_i = e_{15}(1 + m_i) - \varepsilon_{11}l_i$$
$$\delta_0 = c_{11}\,c_1 + k_0^2(c_{13}c_2 + e_{31}c_3) - \beta_1$$
$$\delta_1 = k_0[c_{44}(c_1 - c_2) - e_{15}\,c_3]$$
$$\delta_3 = c_{13}\,c_1 + k_0^2(c_{33}c_2 + e_{33}c_3) - \beta_3$$
$$\tau_1 = k_0[e_{15}(c_1 - c_2) + \varepsilon_{11}\,c_3]$$
$$\tau_3 = e_{31}\,c_1 + k_0^2(e_{33}c_2 - \varepsilon_{33}c_3) + p_3$$

Moreover, the constants c_i are given from the solution of the following linear system:

$$\begin{bmatrix} c_{11} - c_{44}k_0^2 & c\,k_0^2 & e\,k_0^2 \\ c & c_{33}k_0^2 - c_{44} & e_{33}k_0^2 - e_{15} \\ e & e_{33}k_0^2 - e_{15} & \varepsilon_{11} - \varepsilon_{33}k_0^2 \end{bmatrix}\begin{bmatrix} c_1 \\ c_2 \\ c_3 \end{bmatrix}$$
$$= \begin{bmatrix} \beta_1 \\ \beta_3 \\ -p_3 \end{bmatrix}$$

(A4)

REFERENCES

1. **Chen W.Q.,** (2000), On the general solution for piezothermoelasticity for transverse isotropy with application, _Journal of Applied Mechanics_, 67, 705–711.
2. **Fabrikant V.I.** (1989), _Applications of Potential Theory in Mechanics: A Selection of New Results_, Kluwer Academic Publishers, Dordrecht.
3. **Fabrikant V.I.** (1991), _Mixed Boundary Value Problems of Potential Theory and Their Applications in Engineering_, Kluwer Academic Publishers, Dordrecht.
4. **Kaczyński A.** (2014), Thermal stress analysis of a three-dimensional anticrack in a transversely isotropic solid, _International Journal of Solids and Structures,_ 51, 2382–2389.
5. **Kaczyński A., Kaczyński B.** (2017), On 3D problem of an anticrack under vertically uniform heat flow in a transversely isotropic electro-thermo-elastic space, _European Journal of Mechanics A/Solids_, 66,15–25.
6. **Kaczyński A., Kozłowski W.** (2009), Thermal stresses in an elastic space with a perfectly rigid flat inclusion under perpendicular heat flow, _International Journal of Solids and Structures,_ 46, 1772–1777.
7. **Kellogg O.D.** (1953), _Foundation of Potential Theory_, Dover, New York.
8. **Podil'chuk Yu.,N., Morgado A.H.P.** (2000), Stress distribution in a transversally isotropic piezoceramic body with an elliptic crack in a uniform heat flow, _International Applied Mechanics_, 36(2), 203–215.
9. **Rahman M.** (2002), A rigid elliptical disc-inclusion, in an elastic solid, subjected to a polynomial normal shift, _Journal of Elasticity_, 66, 207–235.
10. **Rao S.S., Sunar M.** (1994), Piezoelectricity and its use in disturbance sensing and control of flexible structures: a survey, _Applied Mechanics Reviews_, 47, 113–123.
11. **Wang B.,L., Noda N.** (2004), Exact thermoelectroelasticity solution for a penny-shaped in piezoelectric materials, _Journal of Thermal Stresses,_ 27, 241–251.
12. **Yang J., Jin X., Jin N.** (2014), A penny-shaped crack in an infinite linear transversely isotropic medium subjected to uniform antisymmetric heat flux: Closed form-solution, _European Journal of Mechanics A/Solids_, 47, 254–270.

BUTT WELDING OF ROUND DRIVE BELTS

Krzysztof WAŁĘSA*, Ireneusz MALUJDA*, Krzysztof TALAŚKA*

*Faculty of Machines and Transportation, Chair of Basics of Machine Design, Poznań University of Technology,
ul. Piotrowo 3, 60-965 Poznań, Poland

kwalesa@poczta.fm, ireneusz.malujda@put.poznan.pl, krzysztof.talaska@put.poznan.pl

Abstract: The on-going rapid development of industry encourages development of new production technologies and designing of machines that use inventive mechanical engineering solutions, a big demand for parts of such machines being a natural consequence. Polymeric power transmission belts are a good example of that. This paper proposes an improvement in the process of production of such belting. Their production includes cutting to length and splicing of elastic round belts to obtain endless belts of the specified length. This is the key phase of the whole production process. A number of splicing methods are available using different physical phenomena. One of them is butt welding technique. In this process heat is applied on the material through an additional heating element called the heat platen. The effect depends on several factors, including preparation of the work pieces. Due to its characteristics the process is often carried out by hand. The need for automated manufacturing was created by important factors associated with manufacturing on an industrial scale: cost, time and quality. The proposed butt welding machine, complete with a control system is an answer to this need. The practical benefits include improved repeatability of splices, time savings and less work load for the operator.

Key words: Splicing, Welding, Power Transmission Belts, Conveyor Belts

1. INTRODUCTION

Machines and equipment used in industrial applications are becoming more and more complicated. There are multiple factors responsible for that.

The technological progress results in an increasing variety of products designed to match various needs of people. This results in an increasing variety of machines that are needed to produce them. Consequently, the machines and equipment are becoming more and more complicated. Improvement of the process efficiency is a desired result.

Note also that automated equipment can perform a sequence of tasks repeatedly and without needing further action of the operative and thus it can successfully replace man in the process of production. As an additional benefit, relieving the operator from burdensome tasks promotes a better and safer work environment. Moreover, a higher accuracy and repeatability of finished product parameters has a beneficial effect on the production quality.

Another important factor responsible for increasing complexity of industrial machines are the cost efficiency and reduction criteria. Reliability and simplicity of operation are closely related to them.

This created a need for fully automatic machines in which power is transmitted through round, polyurethane belts (Domek and Malujda, 2007). Belts of this type are widely used for transmission of power in machines such as rolling mills, roller conveyors, sorting lines and conveying belts. Their main task is transmission of power between the subsequent roller assemblies or processing stations. Enjoying a very wide range application in many industries, including in particular light industry (for example in papermaking or plastic production machines) such belt is in high demand. They are used in difficult conditions, i.e. in low and high temperatures, environments susceptible to electrostatic discharge and in food or medical industries (Domek et al., 2016). What is more, like in gear with timing belt, round belts are subjected to action of lots of forces. Circumferential, pre-tension, friction and centrifugal forces, also vibration, cause that there are complex stresses in cross section of belt (Domek and Dudziak, 2011). This provoke high requirements of their quality.

Round polyurethane belts can be used in lots of specialist applying, i.e. in special robotic arm joint mechanism, with two twisted small diameter belts (Inoue et al., 2016). High quality of round polymer belts is required. The main client are manufacturers of machines and beside installation on the delivered machine such belts comes also as a necessary spare part as part of delivery. The demand for such belts reaches hundreds of thousands of pieces.

All the above-mentioned factors have created the need for automation of the splicing process during production. This can be obtained by designing machines performing the tasks which so far had to be done by hand. The desired effect is to develop the process of splicing with considerably limited involvement of humans to relieve the operative from no longer necessary work and to ensure functionality of the designed automatic splicing system.

These were the assumptions for the research project whose results are described herein. This paper describes a proposed mechatronic device enabling automation of the belt splicing process. Heat platen butt welding technique was chosen as a well-proven, widely accepted splicing method, simple and economical. In addition this type of bonding technique, allow to reach high strength joints (Amanat et al., 2010). The engineering work has covered both mechanical and control aspects.

2. SPECIFIC FEATURES OF THE DRIVE BELTS MANUFACTURING PROCESS

Welding of belts section is one of the key steps in the manufacturing process. A number of factors must be considered as part of the engineering work to ensure that the process is performed as desired. Quality of the splicing directly affects the quality of the manufacturing process as a whole. It is important to recognise characteristic processing stages. As important are the specific parameters of the material used in production. Both the procedure and the welding parameters must be defined according to all these factors.

2.1. Manufacturing process

Polyurethane power transmission belts are produced from round cords, solid or hollow. The cord section is wound around and joined permanently to obtain the specified circumferential length. This length can vary over a wide range depending on the installation requirements, generally from a few dozen millimetres to a few metres. The belts are manufactured from solid or hollow round cords (belting) of thermoplastic polyurethane which is a material having specific properties. Two methods are used in production of polyurethane belting: extrusion and injection moulding (Sikora, 1993). Diameters of such intermediate products are generally in the range from a few to over a dozen millimetres (Behabelt, 2015).

These intermediate products are usually supplied in quite long sections which is typical of the process used in their production It is not convenient from the point of view of storage and transport. The cord material features elasticity, shape memory and specific allowable bending radius. As a measure to cope with this inconvenience the material is factory wound on spools (rolls) holding between a few dozen to a few hundred metres of cord (Behabelt, 2015).

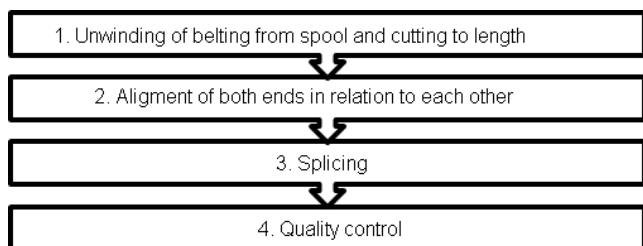The next stage is final processing comprising the following steps (Fig. 1):

Fig. 1. Polyurethane belt production flow chart

In the first step the cord is unwound from the spool and cut to length (1). This length equals the finished product circumference plus welding allowances. The objective is to obtain the effective length of the finished product which is equal to the circumference measured along the axis of symmetry of the cord (Fig. 2). The cut must be done perpendicular to the axis of symmetry of the cord (Fig. 3). This will provide matching ends, important in further processing.

Next the two ends of the cord are aligned in relation to each other and brought together by force *F*. It is critical to ensure proper alignment before welding starts (Fig. 3). This is usually ensured by guiding the two ends with axially aligned guides.

The final product can be formed to shapes other than circular, for example ellipsoidal or any other looped shape, as long as the minimum bend radius is maintained. Its value is most often given in the data sheets by specifying the minimum diameter of roll around which the belt can be routed.

The next step is splicing itself. The parameters of this step are critical to the quality of finished product.
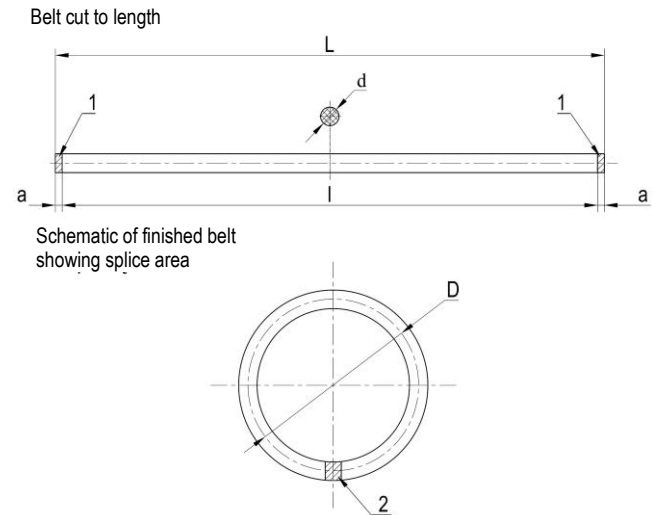

Fig. 2. Dimensional relationships of round belts wound in a circular shape: L – total (cutting) length, l – belt length (circumference after splicing), a – splicing allowance, d – belt diameter, D – diameter of the ring obtained from the cord section, 1 – extent of splicing allowances, 2 – splice area
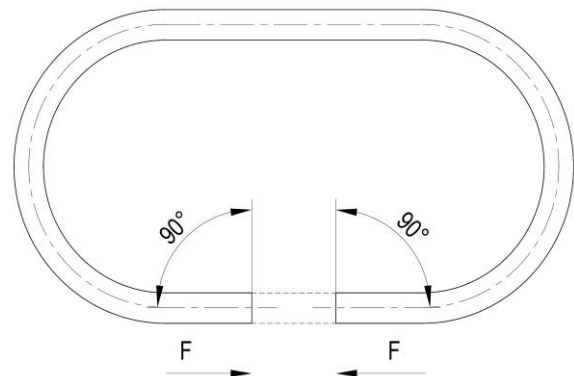

Fig. 3. Schematic drawing showing alignment before splicing: *F* – force required to bring together the two ends of cord to be joined

In the final step the product is removed from machine and a quality check is carried out. The inspection should cover:
– dimensions in the splicing area – to be checked against specifications (seam diameter should correspond to the thickness of undisturbed part of material),
– axial alignment of the two ends across the splice and alignment of the two horizontal faces during welding,
– welding quality, that is full bonding over the whole thickness.

Any deviation from the above requirements would affect the belt performance, manifested for example by vibrations in power transmission systems.

2.2. Joining material properties

According the design assumptions the material to be joined is polyurethane cord. Polyurethane is one of thermoplastic material, with some of elastomer features.

What is specific about polyurethane is that depending on the chemical composition it can be classified as purely thermoplastic or thermoplastic/elastomeric material. Its physical and chemical properties depend on its chemical composition, internal structure and molecular weight (Żuchowska, 2000).

Polyurethanes have segmental (block) structure. Their hydrocarbon chain is built of alternating flexible (methylene, ester or ether) and rigid (urea, urethane, aromatic) blocks (Fig. 4). The hard blocks are responsible for the strength performance and soft ones improve the deformation capacity of the material (Puszka, 2006). These domains do not intermix and make up two-phase heterogenic structure. The flexible polyurethane varieties contain between 60% and 80% of soft blocks. They are generally elastic and easily deformable. The other domain, made up of hard blocks is responsible for mechanical strength (Żuchowska, 2000).
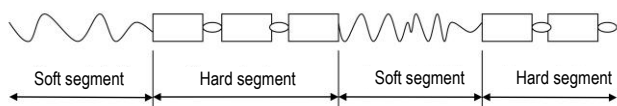

Fig. 4. Example sequence of blocks in polyurethane (Puszka, 2006)

The polyurethane variety used for production of belts is classified in the group of thermoplastic elastomers. They are a mixture of amorphous and crystalline regions.

As a result, polyurethane combines the properties of the two groups. The crystalline regions are responsible for the high strength parameters, clear-cut phase transition temperatures and resistance to chemical compounds. Amorphous regions on their part are responsible for plastic behaviour of the material (Ashby, Jones, 1996). A specific feature of polyurethane, distinguishing it from other plastics, is its behaviour under the effect of higher temperatures. On the macroscopic scale it is manifested by properties typical of elastomers up to the temperature of ca. 100°C which is followed by softening typical of thermoplastic materials when heated above that limit (Ciszewski, Radomski, 1989). This is an important characteristic from the point of view of the welding process.

The analysed plastic has a number of physical properties making it a suitable material for production of power transmission belts. Moreover, the physical properties can be modified, givingit universal character. These characteristics include high elastic modulus, high tensile strength and resistance to repeated bending – a most welcome feature for power transmission and conveying belts. Polyurethanes surpass other thermoplastic materials in terms of abrasion and tear resistance, as well as vibration damping performance. Also important, especially in the analysed area of application is the material's insusceptibility to various chemicals. Polyurethanes are resistant to oxidising agents, solutions of acids, lubricants, oils and organic solvents (Madej, Ozimina, 2010). This makes them a suitable material for conveying systems which often involve the presence of various chemical that can be harmful to other engineering materials.

However, it is not possible to precisely determine the properties of polyurethanes without detailed empirical studies. According

to the review of available literature the upper limit of temperature resistance ranges between 80°C and 120°C (Madej, Ozimina, 2010). The tensile strength in normal operating conditions can be assumed in the range from 20 MPa to 70 MPa. Breaking failure occurs at 200 – 800% elongation. Shore A hardness ranges between 35° and 98° (Żuchowska, 2000).

Both thermal and rheological properties must be considered in analysing the process of welding polyurethane belting. When analysing the influence of temperature it is important to consider the melt volume-flow rate (MFR). This characteristic is important for the welding process efficiency beside other key parameters which are: density, softening point and thermal conductivity of the material. As the value of MFR increases the viscosity of the material decreases, reducing the internal cohesion forces. As a result, partially melted material tends to escape from the splicing area under the force of gravity. MFR decreases with the increase of molecular weight (Żuchowska, 2000).

All these characteristics must be taken into account when designing polyurethane welding machine. Their values should define the welding process parameters.

3. HOT PLATE WELDING

Hot plate welding process is one of the polyurethane direct bonding method (Amanat et al., 2010). It uses the thermal action in the volume of material. In hot plate welding process the joined pieces are heated up by the heat transferred from the heating element to the mating surfaces. This is performed with a specially mounted heater unit comprising a hot plate which is inserted between the belting ends (Fig. 5). The belt ends are heated up as they are pressed against the platen which leads to softening and partial melting of the material in the contact region.
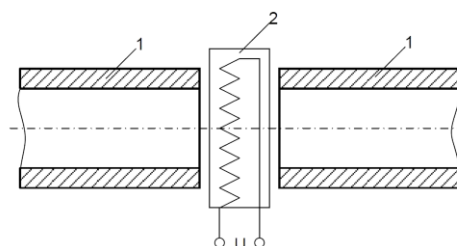

Fig. 5. Butt welding of polymer cords (Sikora, 1993):
1 – pieces to be joined, 2 – hot plate, *U* – supply voltage

The hot plate shape and power supply parameters should be appropriate to the type of pieces to be joined. The surface of hot plates is always coated with a non-stick material. If the working temperature does not exceed 200°C, teflon with the thermal resistance of 270°C can fit the purpose. For higher working temperatures the heat platens made of Al-Cu alloy which can withstand temperatures up to 350°C are used. The purpose is to prevent adhesion, and stick of plastic to the heating surface (Klimpel, 1999). Stick material causes deforming the section of melting polymer, and in consequence some gaps in the bond line (Yousepour, 2004).

Fig. 6 presents the procedure which ensures durable bonding of polyurethane belting with a hot plate welding system. Generally this process it is on heating and pressing against of joining surfaces (Amanat et al., 2010). Using this cycle chart, we can create

the algorithm of welding process, directly for control system (Rzasinski, 2017).

In the first step the two ends of belting are brought together while maintaining alignment and keeping a gap sufficient for inserting the heated plate. Next the plate is placed between the belting ends. It is important to ensure full contact between the ends and the plate so that the temperature is increased evenly throughout the mating surfaces. The plate should be inserted between the ends when it has reached the working temperature. This ensures controlled heating conditions and shortens the process time.
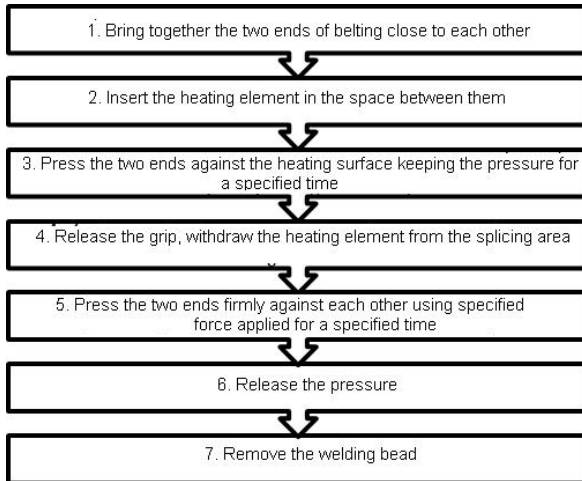

Fig. 6. Butt welding sequence for splicing polyurethane belting

Next the two ends should be pressed against the plate with a specified force. Under the effect of heat transferred to the belting ends the material softens and starts to melt. Additionally polymer chains are activated facilitating chemical reactions associated with linking polymer chains.

In this case heat conduction is an unsteady process. The varying parameters are the coefficient of heat conduction, specific heat, density and viscosity of the heated material. In the case of polyurethane these values strongly depend also on the chemical composition, crystalline structure of the plastic and the sequence of soft and hard blocks.

When the material gets sufficiently softened and partially melted the pressure is released and the belting ends are pulled away from the plate. Next the heater unit is withdrawn from the splicing area.

In the next step the two pieces are pressed against each other. It is important that this step takes place as soon as the plate has been removed from the splicing area. This is to avoid excessive cooling and solidification of melted material. This is the critical step in the whole butt welding process. Chemical reactions take place at that point whereby the macromolecules of melted polymer are connected. This creates a permanent bond between the joined pieces. As soon as the belting ends have been effectively joined pressure can be released. At this point cooling and curing of the joint starts.

Note that the process of butt welding shortens the belting length. Pressing the two ends against each other when the material is soft creates a welding bead that is a ring of material surrounding the joint. The mount of bead material is proportional to the decrease in length of belting. This bead must be removed, most often by cutting, to ensure correct operation of the belt.

Using the cycle chart (Fig. 7) let us review the basic parameters of the butt welding process:

–   unit pressure applied on the joined pieces with the maximum values applied in two steps of the welding process. It includes pressure p_g applied to level out the surfaces and pressure p_z applied during proper welding. Its value ranges generally from 0.05 MPa to 0.1 MPa depending on the type of joined materials (Klimpel, 1999). Decrease of pressure p_n in the second phase of heating is related to significant softening of thermoplastic materials under the effect of heat. Excessive pressure applied at this stage would cause excessive amounts of molten material to flow out of the splicing area.
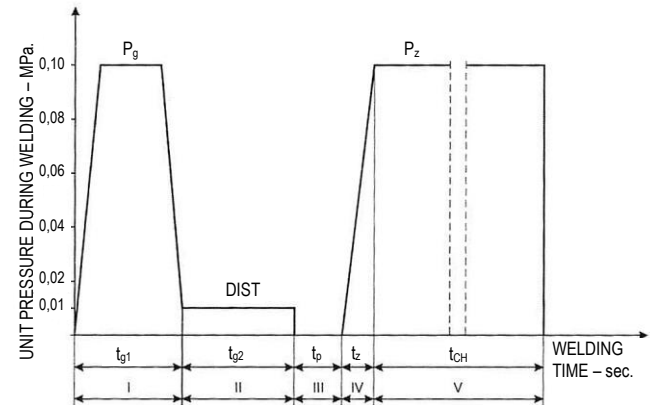

Fig. 7. Cycle chart (cyclogram) of the hot plate welding process (Klimpel, 2000): Stages of the process: I – levelling out the surfaces at high pressure, II – heating up at low pressure, III – hot plate is withdrawn, IV – increase of pressure, V – welding and cooling of joint; Unit pressure values: p_g – during levelling out the faces, p_n – during heating up, p_z – during bulging; Times: t_{g1} – levelling out the faces, t_{g2} – heating up, t_p – withdrawal of the hot plate, t_z – second pressing, t_{CH} – bulging and cooling of joint

–   the cumulative process time, ranging from over a dozen seconds to a few dozen minutes (Cocard, 2009). The levelling out time t_{g1} is usually short and does not exceed a few seconds. In this phase the mating surfaces (faces) are levelled out on the hot plate by partial melting any protrusions. The heating up time t_{g2} depends on the heated mass and on the thermal properties of the material, such as conductivity and specific heat. It is generally much greater than the time t_{g1} and can reach up to a few dozen minutes. In special case the whole heating phase (t_{g1} and t_{g2}) can last more than 60 minutes and depend also on base material's strength (Amancio-Filho, dos Santos, 2009). The hot plate withdrawal time t_p is also referred to as pause time must not be longer than a few seconds and preferably should be as short as practicable. The same applies to the pressure increase time t_z which, when too long, will unnecessarily increase the input of energy. The last step of the process includes bulging and gradual cooling of the joint. It is usually the longest of all steps with the time t_{CH} ranging between a few dozen seconds to over a dozen minutes, depending on the external conditions (Klimpel, 1999).

–   bulging degree, usually defined by the length reduction during welding. It strongly depends on the maximum pressure applied during welding.

–   welding temperature T_z which does not equal the heat platen working temperature T_p, and is usually lower by a few dozen

degrees (Fig. 8). For processing partially crystalline polymers, the maximum temperature T_z is usually set ca. 80°C to 90°C above the melting point. This is different in the case of amorphous polymers for which it is difficult to determine the phase transition temperature and, as such, the welding temperature is taken 150°C – 160°C above the glass transition temperature (Klimpel, 2000). It is important to choose a temperature that provides sufficient level of softening without causing any harm to the material. The initial degradation temperature of most polyurethane elastomers is ca. 270°C – 320°C, dependent on material type and composition. Exceeding this value cause destroy the material volume in a few stages (Wanqing et al., 2017). On the other hand, in case of some polymers, joint strength increases with welding temperature (Evers et al., 2017). The welding temperature choice is very important issue.
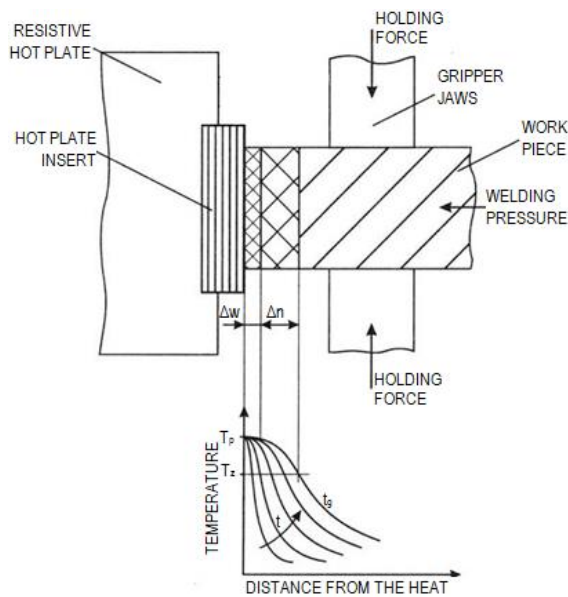

Fig. 8. Schematic of heating an object with a hot plate (Klimpel, 2000): T_p – temperature of the hot plate, T_z – softening point of welded plastic, t_g – specified heating time, Δw – allowance for levelling out the surfaces, Δn – thickness of layer heated up above the softening point

– levelling out allowance Δw, that is the length of belting which is partially melted in the initial heating phase with higher pressure applied on the belting in order to level out the faces.
– thickness of layer heated to the temperature required for softening of material Δn that defines the amount of material softened during the process of welding. Directly associated with it are the heating time and the level of bulging. It is generally assumed that the thickness of softened layer Δn should not be smaller than 30% of the thickness of the joined material for partially crystalline polymers and 14% of that thickness for amorphous plastics (Jasiulek, 2006).

Hence, obtaining a welded joint with the specified shape and mechanical properties requires considering a number of factors and specifying many interrelated parameters. In addition, big influence to welding process has pieces preparation. Their smooth surface lead to increasing contact with hot tool and better heat transference (Amoncio-Filho, dos Santos, 2009). When the heating and cooling process is considered, also it should be noted some division in three zone with different impact of temperature.

This phenomenon can be observed in all of the semi – crystalline thermoplastic polymers, so in butt welding of round belts it has some impact to process (Casalino, Ghrobel, 2008). The difficulty of predicting the behaviour of different types materials during the process of welding adds to the complexity of the problem. All the above factors are taken into consideration when formulating the machine design assumptions.

4. MECHATRONIC DESIGN APPROACH

4.1. Mechanical part

Fig. 9 presents the system for automatic splicing of belts by hot plate welding designed after examining the various factors influencing the butt welding process. The designed system has modular structure.
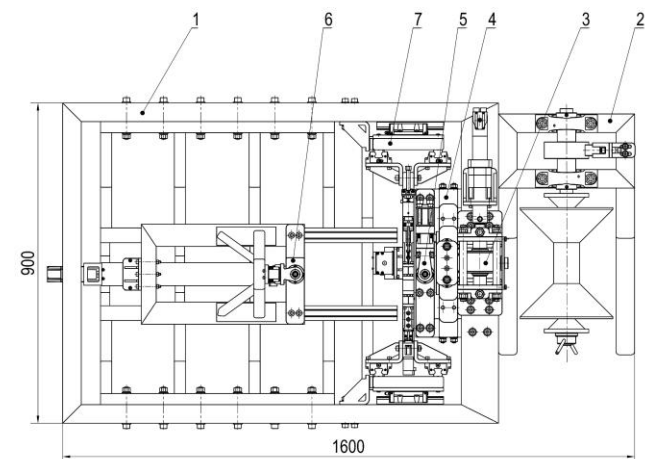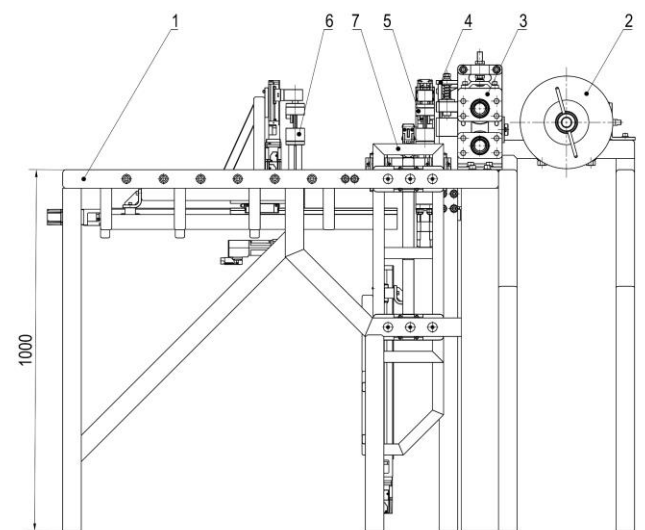

Fig. 9. System for automatic welding of belts: 1 – main frame, 2 – unwind unit, 3 – roll feeder, 4 – shear cutter, 5 – fixed gripper, 6 – sliding gripper, 7 – welding assembly

The main structural component is the main frame (1). Its main function is to combine all the assemblies and keep them at the required distances in relation to each other.

The first assembly (2) is designed for pulling the cord from the spool. The main function is to unwind only such length that is required for further processing. Uncontrolled unwinding of the spool must be prevented.

The next important assembly is the roll feeder (3). Its primary function is to set the belt in translational motion during the preparatory phase before welding. The cord is moved at a constant speed adjusted to the operating speeds of the subsequent assemblies. An additional function is to measure the length of the unwound cord section. This information is used by the cutting control system to ensure the specified length of the finished belt.

Next the cord is directed to the shear cutter (4) synchronised with the roll feeder.

The fixed gripper assembly (5) is designed to grip one end of belting and position it in three-dimensional space. Its characteristic feature is that it can rotate about its axis and grip the cord through displacement of the gripping parts. It is fixed to the main frame of the machine (1).

The same idea is used in the design of the sliding gripper assembly (6). Its movements are similar to the fixed gripper assembly (5). The difference is that in addition to the movements of the fixed gripper the whole assembly can move in the direction parallel to the cord feed axis. This feature enables producing belts of different lengths and prevents collisions of moving parts during operation.

The two gripper assemblies operate in conjunction. Their main function is to arrange the ends of cord section facing each other just before welding. Moreover, then can move to adjust process parameters as required, including pressure during heating up and welding and shifting to remove the welding bead.

The most important part from the point of view of the overall function of the machine is, of course, the welding assembly (7). It supplies the heat required for softening and partial melting of the work pieces, ensures that the specified geometric parameters are obtained and removes the welding bead from the finished belt.

The design enables carrying out all the operations required to splice the belt to the specified geometric and strength parameters.

In order to understand the overall operation of the machine let us consider the design and operation of its assemblies. These are:

‒ unwind unit (Fig 10) – pulls the cord from the spool. The assembly is mounted on the main frame (1). The unwind shaft (3) is supported on the frame through bearing assemblies (3). The shaft can freely rotate about its axis. The spool with belting (4) is fitted on the shaft and protected from sliding off with a wing nut (5). Thus the spool rotates together with the shaft. To control the movement the assembly is provided with a drum brake (6) comprising the brake shoe and drum (7) mounted on the shaft with the stopping effected by friction. The brake generates friction moment which stops the spool after the required length has been pulled off. This prevents uncontrolled unwinding of the cord.

‒ the belt is set in motion by the roll feeder (Fig. 11). The main sub-assembly of the feeder is the powered roll with knurled surface (1) supported on the bearing (4) mounted in the bearing case (3). The back-up roll sub-assembly has a similar design comprising the shaft-mounted plain surface pressure roll (2) supported on the bearing (5) mounted in the case (3). The bearing sub-assembly can be moved and is linked to the roller gap adjustment mechanism (9) which is also fixed to the case (3). It enables pressing down the belting against the powered

roll (1) through pressure roll (2) owing to its vertical movement. The roll driving system (1) comprises the servomotor (6) and the planetary gear (7). The feeder case (3) and bracket of the drive system (8) are bolted to the main frame ((1) in Fig. 9) A supplementary element of the system is the cord guide (10) whose task is to feed the cord in the central part of the gap between the feeder rolls.
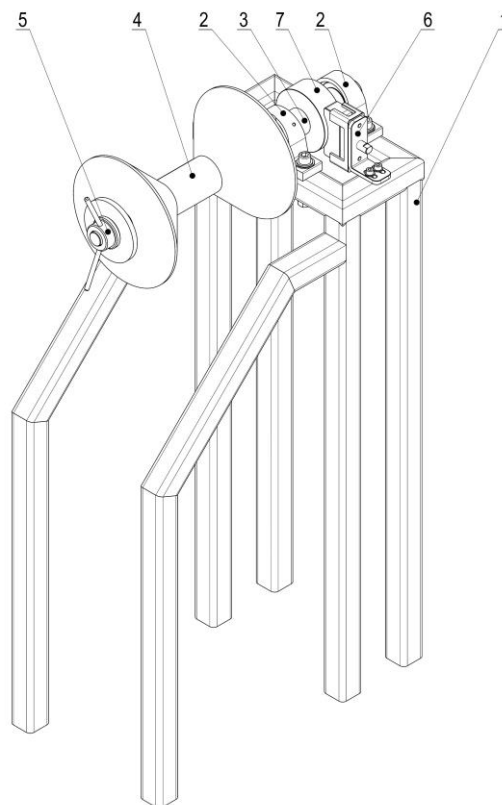

Fig. 10. Unwind unit: 1 – frame, 2 – bearing assemblies, 3 – main shaft, 4 – spool, 5 – securing nut, 6 – drum brake sub-assembly, 7 – brake drum

The roll feeder receives the cord from the unwind unit and moves it to the shear cutter assembly ((2) and (4) in Fig. 9). When servomotor is started (6) the torque is transferred through the planetary gear reducer (7) and through the shaft to the powered roll (1). The cord which is pressed down by the top roll (2) moves without any slipping with the speed of the tangent component of the angular speed of powered roll (1) and in this way it is fed to the subsequent assemblies of the machine. The cord length control is based on the number of rotations of the servomotor (6), geometric parameters of the roll (1) and the reducer gear ratio (7). Upon reaching the preset value the servomotor is stopped. Cord slippage is prevented by the powered roll (1) surface texture and pressure exerted by the pressure roll (2) which ensures reliable length measurement of the cord section delivered for welding.

The cord is cut to length by the shear cutter assembly (Fig. 12). Its support frame is bolted to the main frame ((1) in Fig. 9). It includes the die (5) and the double-acting air cylinder (2). The die has a prismatic groove in which the cord is supported during movement and cutting to length operations. The cord is fed between the prismatic surfaces (5) and the hold-down device (6). After cutting command is received from the control unit the air

cylinder (2) through the upright guides (3) supported on bearings effects movement of the cutting sub-assembly (4) comprising the cutting blade (knife) and all the required brackets/holders and guides. The cutting sub-assembly (4) moves down into the die (5) thus cutting the cord. The hold-down device (6) is elastically connected to the cutting sub-assembly. Its function is to press down the cord against the die (5) during cutting. This secures the cord in place, ensuring perpendicular cut (in relation to the longitudinal axis of the cord). Owing to the flexible connection between them the shear cutter assembly (4) and hold-down device (6) can move together during cutting operation in which the shear cutter assembly (4) can be lowered to cut through the cord while the hold-down device rests on the cord surface (4). The flexible components, compressed by the down movement of the shear cutter generate the pressure holding down the cord against the die (5).
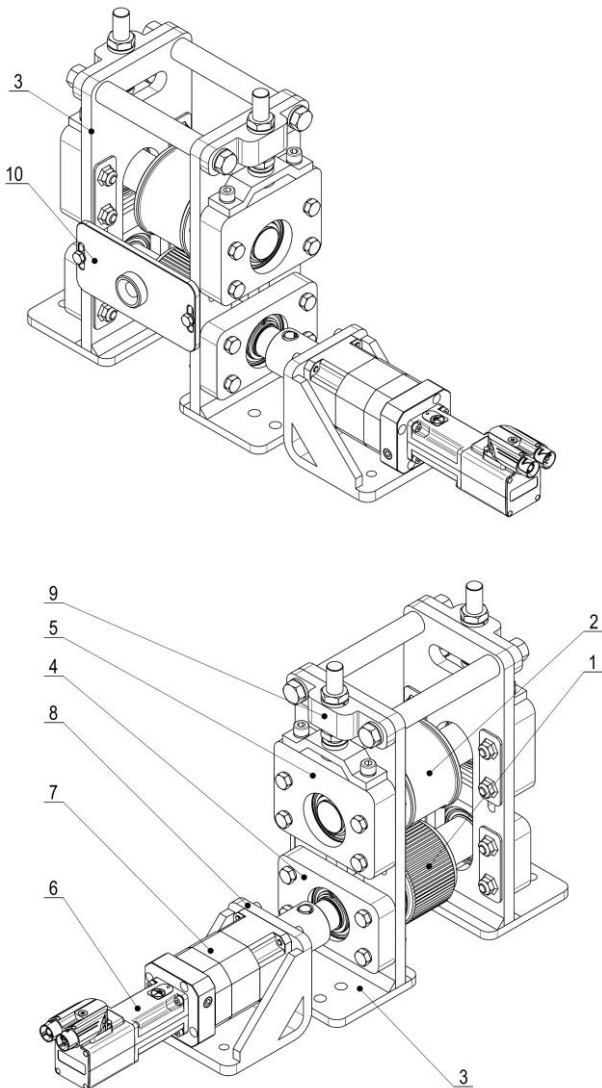

Fig. 11. Roll feeder: 1 – powered roll, 2 – pressure roll, 3 – case, 4 – bearing assembly, 5 – hold-down device bearing system, 6 – servomotor, 7 – planetary gear reducer, 8 – drive system bracket, 9 – hold-down pressure adjustment mechanism, 10 – cord guide

The die design enables cutting cords with different diameters without a need for re-tooling and adjusts the cord position during cutting. This facilitates operation and ensures satisfactory degree of perpendicularity of cut in relation to the cord axis.

– the function of the fixed gripper assembly (Fig. 13) is to grab and position one of the ends of the belting section.
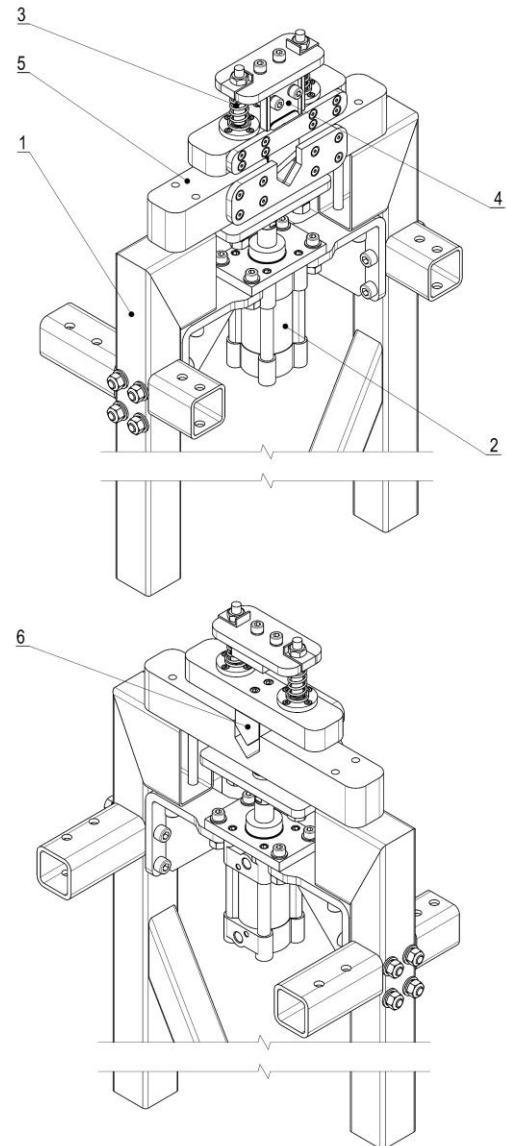

Fig. 12. Shear cutter assembly: 1 – frame, 2 – air cylinder, 3 – guide, 4 – cutting sub-assembly, 5 – die, 6 – hold-down device

The fixed gripper assembly rotates to turn the cord end about its axis and positions it in space. The rotational movement in the range from 0° to 180° is effect by the drive system (1) comprising the servomotor and the angular reduction gear bolted to the base plate (2). It delivers the torque to the bushing (4) fixed to the gripper base plate. The two plates (2 and 3) make up the supporting structure of the assembly, bolted to the shear cutter main frame ((1) in Fig. 12). The bushing is used to support the sectional lower jaw (5) whose shape enables grabbing and guiding the cord during movement. It operates in conjunction with the sliding top jaw (6) which is also shaped to grab the cord. The top jaw is fixed to the yoke (7) connected with the carrier of translational drive system (8) which effects its vertical movement. This sub-assembly comprises a stepper motor and a ball screw mounted through auxiliary frame (9) to the base plate (2). In this arrangement the gripper jaws close up, grabbing and securing the cord in position between the prismatic surfaces of the jaws.
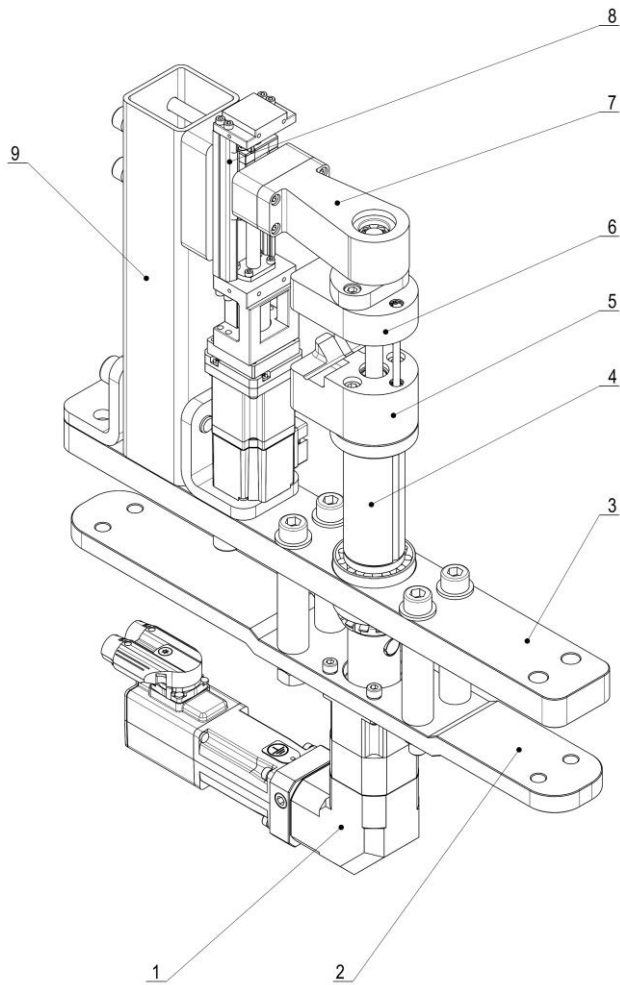
Fig. 13. Fixed gripper assembly: 1 – rotational movement drive system, 2 – drive system mounting plate, 3 – gripper system mounting plate, 4 – rotating bushing, 5 – lower jaw, 6 – sliding top jaw, 7 – yoke of the top jaw, 8 – translational closing movement drive system, 9 – auxiliary frame

– the function of the sliding gripper assembly (Fig. 14) is to grab and position the other end of the cord section.

The design and principle of operation of the cord end grabbing and turning system is similar to that of the fixed gripper assembly. The differences are limited to some design details concerning mounting of the servomotor (10), reduction gear (9), stepper motor powered gripper rotation drive system (12), gripper ball screw (11) and top jaw yoke (13). Notwithstanding the above differences the principle of operation remains the same.

The assembly is mounted through the base plates of the gripper (7) and the drive system (8) on the sliding frame (5) guided by the ball screw guides (6). This arrangement enables translational movement along the cord axis. The translational movement is effected by the stepper motor (3) through the ball screw drive (4). It is fixed to the frame through the bracket (8). For rigid construction, the translation movement drive system (8, 11 and 12) and translation movement guides (6) are fixed to the frame (1) which in turn is mounted on the main frame of the machine ((1) in Fig. 9).

Worthwhile noting is the design of sliding the gripper assembly whereby the cord end grabbing and turning mechanism together with the drive systems can be moved along the cord axis to accommodate cord sections of infinitely variable length. Moreover,

this feature enables pressing the ends of the cord section against each other in the subsequent steps of the splicing process and is used to remove the welding bead.
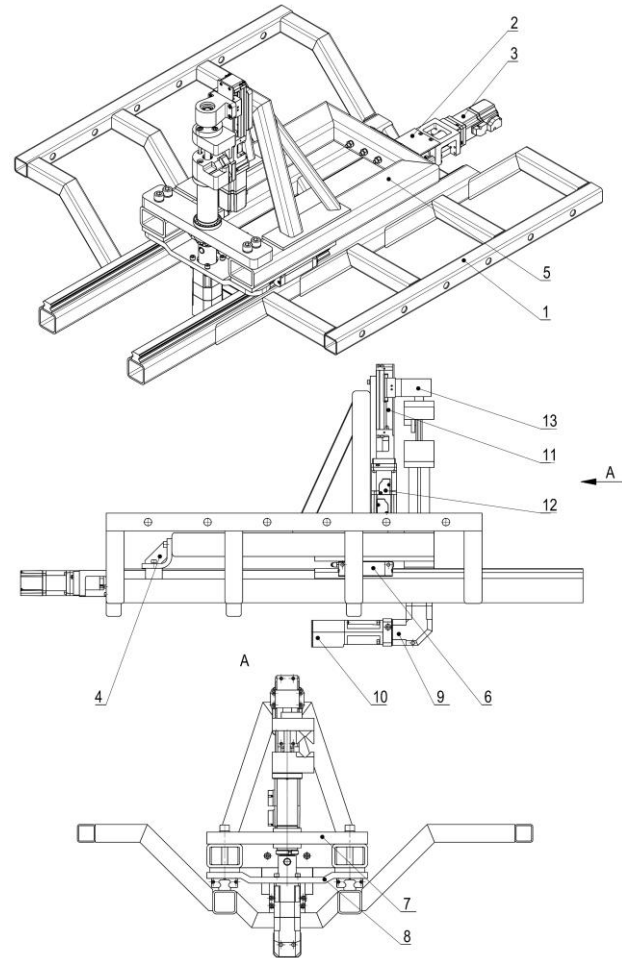

Fig. 14. Sliding gripper assembly: 1 – main frame of the gripper assembly, 2 – translational motion drive system, 3 – translational motion stepper motor, 4 – sliding frame bracket, 5 – sliding frame, 6 – linear guide, 7 – gripper base plate, 8 – rotational drive base plate, 9 – gripper rotation angular gear, 10 – gripper rotation servomotor, 11 – gripper closure ball screw, 12 – gripper closer ball screw, 13 – top jaw yoke

– the heater assembly (Fig. 15) is the most important assembly of the machine described in this paper. Its function is to supply sufficient amount of energy to the ends of the cord section, position the ends during welding and remove the welding bead.

The main frame (1) supports the horizontal guide plates (2) which, in turn, provide support for carriers (3). They operate in conjunction with the profile rails (4) bolted to the main frame of the machine ((1) in Fig. 9). This mechanism enables lateral movement of the whole assembly in the direction parallel to the cord axis. This arrangement ensures equal force with which the two ends are pressed against the heater and is used during the welding bead removal operation. The welding table vertical movement mechanism is also supported on the main frame of the machine (1). This sub-assembly comprises an auxiliary frame (5) used to support the ball screw drive (6) powered by the stepper motor (7). Through the bracket (8) the ball screw drive (6) is fixed to the

frame (9) of the sliding welding table. The carriers of the translational movement guides (11) are fixed to the ball screw drive through brackets (10) and the guides are coupled with profiled rails (12) bolted to the frame (1). This mechanism enables vertical movement of the welding table to eliminate collision with grippers during positioning of the cord section before welding.

The welding table is delimited by the area on top of the frame (9) and is built of the following main sub-assemblies: left-hand die assembly (13) and right-hand die assembly (14) with heater installation (15). These sub-assemblies are equipped with appropriate mechanisms to effect the working movements (Fig. 16).
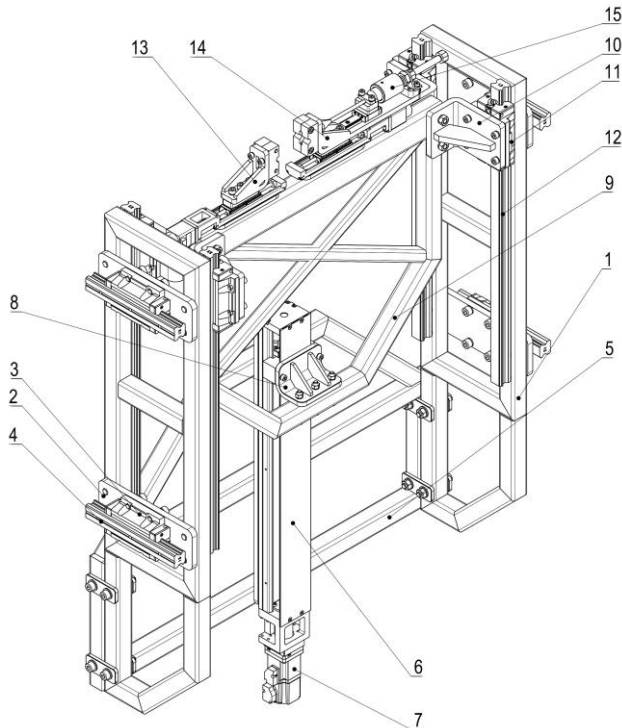

Fig. 15. Heater assembly: 1 – main frame, 2 – horizontal guide plate, 3 – translational movement guide carrier, 4 – guide rail, 5 – auxiliary frame, 6 – vertical movement drive system, 7 – vertical movement stepper motor, 8 – welding table bracket, 9 – welding table frame, 10 – vertical guide bracket, 11 – vertical guide carrier, 12 – vertical guide rail, 13 – left-hand die sub-assembly, 14 – left-hand die sub-assembly, 15 – heater

The base plates (2) of translational movement drive module (3), equipped with ball screw drives with additional guides and limit switches are bolted to the main frame (1). They are driven by stepper motors (4). The left-hand (5) and right-hand (8) die brackets are bolted to their carriers. The bracket support the two dies: cutting die (6) and guiding die (7). Thus the dies can come closer together, closing the ends of cord section within the cylindrical grooves.

The right-hand die bracket (8) supports the profiled rail (14) of the heater guide (9). It moves in conjunction with the guide carrier (13) supporting the heater (9) bolted to it through the yoke (12). The working surface is a flat heat platen with a non-stick coating. This element is inserted in the welding area, i.e. rectangular grooves in the dies due to the action of double-acting air cylinder (10). The cylinder is fixed to the die bracket (8) through the yoke (11). This design enables movement of the heater (9). It can be inserted between the cord ends, closed in the dies (6 and 7) such that the heat platen entirely abuts the end faces.

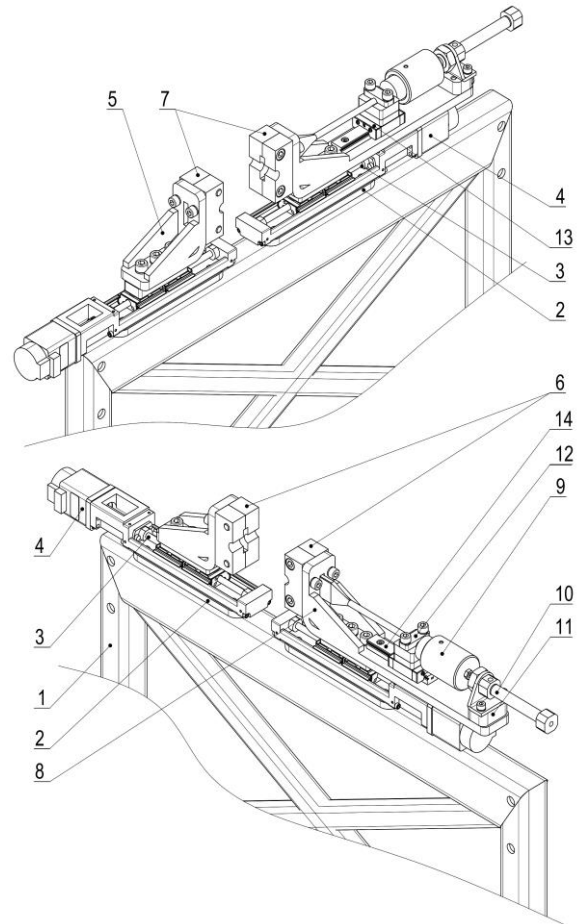– the main frame (Fig. 17) defines the spatial arrangement of all the machine assemblies.

Fig. 16. Welding table: 1 – frame, 2 – base plate of translational movement drive, 3 – translational die movement drive system, 4 – stepper motor, 5 – left-hand die bracket, 6 – cutter die, 7 – guide die, 8 – right-hand die bracket, 9 – heater, 10 – air cylinder, 11 – air cylinder yoke, 12 – heater yoke, 13 – heater translation guide carrier, 14 – profiled rail of the heater translation guide
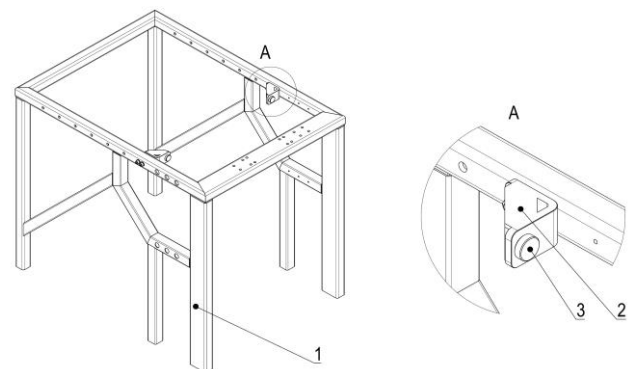

Fig. 17. Main frame: 1 – frame, 2 – end stop bracket, 3 – elastomeric end stop

The frame (2) is welded from steel sections. An important part of the assembly is the end stop (3) fixed to the frame through the ends top bracket (2). Its function is to restrict the range of movement of the heater assembly in the direction parallel to the cord axis during bead removal operation.

The machine has a complicated structure. Moreover, the work area is small, this resulting from the small minimum length of belt (150 mm) to be handled. This makes the fabrication and assembly precision so important for all the sub-assemblies and parts of the machine.

4.2. Control system

The kinematic diagram of the machine (Fig. 18) enables preparation of the machine flow chart. This flowchart is then used to prepare the control system diagram. To avoid confusion it has been decided that the positive direction of translation corresponds to the positive direction of the adopted system of coordinates. For rotational movement the clockwise direction is positive.

As a preparation before starting the machine the spool with cord is placed on the unwind unit shaft (2). Next the cord is pulled from the spool and inserted between the feed rolls (3) through bushing with hole, mounted in the guide plate. This is possible due to free movement of the unwind unit in the XY (c_1) plane. Now adjustments should be done, which must be repeated after each replacement of the spool. Adjustments should cover also the unwind unit (2) and the roller feeder hold-down device (3). This ends the start-up preparations.

Next the operator makes sure that all the mechanisms are in their home positions that is:

- the shear cutter blade (4) is in the top end position, according to the positive direction of movement along axis Y (y_1),
- fixed gripper (5) is in the end position in the positive direction of rotational movement in XZ (b_1) plane. The opening made by the prismatic surfaces of the gripper jaws must be aligned with the shear cutter exit hole. Additionally the top jaw must be lifted up to the top end position of the movement along the Y (y_2) axis.
- the sliding gripper (6) is in the right end position of movement in the positive direction along the X (x_1) axis. Additionally, the gripper should be turned to the end position of the negative rotational movement direction in XZ (b_2) plane and its jaw must be lifted to the top end position of movement in the direction along the Y (y_3) axis,
- the welding assembly (7) is in the lower end position of movement in the direction along the Y (y_4) axis and the dies are completely opened by movements in the positive (z_1) and negative directions (z_2) along the Z axis. The heater must be removed from the die area to the end position of movement in the negative direction along Z (z_3) axis.

The machine can now start in automatic mode. The powered roll of the roll feeder (3) rotates in the in the negative direction of rotational movement in XY (c_2) plane. The cord end moves through the open jaws of the fixed gripper (5) until it reaches the sliding gripper (6). After passing the sliding gripper (so that some portion of the cord extends beyond the element face) the feeder drive system (3) stops without engaging the electromagnetic brake of the servomotor. Now the sliding gripper jaws are closed ((6), movement in the negative direction along axis Y – y_3), the cord is gripped and the jaws drive system is stopped to maintain the grip. Then the assembly pulls the cord from the unwind unit (2) while moving in the negative direction along the X (x_1) axis. The length of the gripper movement depends on the specified belting length. At that point the roll feeder (3) can be restarted (3) to move the belt through open sliding gripper (5) thus increasing its quantity. This quantity is temporarily held between the grippers. When sufficient amount of the cord has been fed the feeder is stopped and the servomotor brake is engaged.
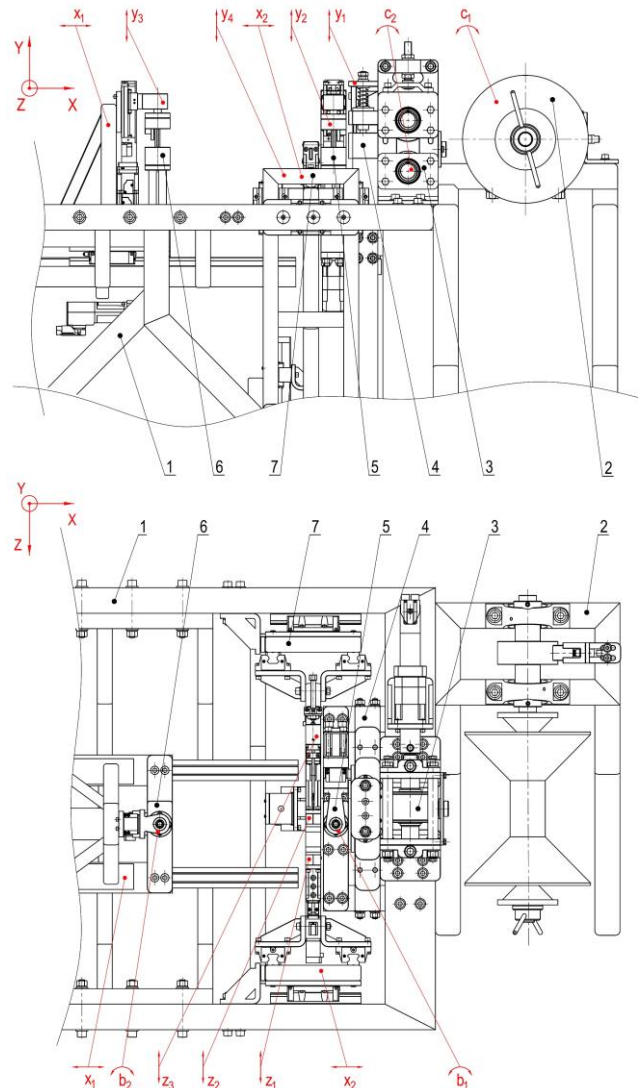

Fig. 18. Kinematic diagram of machine: 1 – main frame, 2 – unwind unit, 3 – roll feeder, 4 – shear cutter, 5 – fixed gripper, 6 – sliding gripper, 7 – welding assembly; Parameters: x_n – translation in the direction of axis X, y_n – translation in the direction of axis Y, z_n – translation in the direction of axis Z, b_n – rotation in XZ plane, c_n – rotation in the YZ plane

Then the fixed gripper (5) closes by movement of the jaws in the negative direction along the Y (y_2) axis. As previously, when the cord is gripped the jaws translational movement drive is controlled to stop in order to maintain the grip. At that point both ends are secured in position and against axial movement.

The next operation is cutting of the cord by the shear cutter assembly (4), involving movement of the cutter together with hold-down device in the negative direction along the Y (y_1) axis. Next the sliding gripper (6) moves in the positive direction along the X (x_1) axis. During this movement the cord ends are initially positioned in relation to each other by rotation of the gripper jaws in the YZ plane by 180° (b_1 and b_2) in opposite directions. This positions the cord end faces facing each other. On completion of this operation the rotational movement drives are stopped and

their brakes are engaged. Next the sliding gripper is moved along the X (x_1) axis to the preset position. The position results from the welding table width and is set at the value preventing collision of the machine assemblies.

Next the heater assembly (7) moves up along the Y (y_4) axis to the position at which the holes in the dies are aligned with the belt ends. Then the vertical movement drive system is controlled to stop. The dies move along the Z axis (z_1 and z_2) until they come in contact, as detected by the limit switches installed on their ball screw drives.

When the cord ends are closed between the dies the heater is inserted between them moving in positive direction along the Z (z_3) axis, powered by air cylinder. Then the sliding gripper (6) moves in the positive direction along the X (x_1) axis in order to press both surfaces against the heat platen. To ensure that the same pressure is applied on both side of the heat platen the whole heater unit (7) is able move along the X (x_2) axis. This movement is not limited by any external control. The cord end mounted in the sliding gripper (6) pushes through the heater the entire heater assembly, thus pressing the heat platen against the cord end that is being held in the fixed gripper (5).

Then the heating up phase follows, resulting in softening and partial melting of the cord end faces. In this phase the pressure can be adjusted by slightly moving the sliding gripper (6) along the X (x_1) axis.

Next the sliding gripper assembly (6) is moved in negative direction along the X (x_1) axis thus moving the end faces away from the heat platen. This enables withdrawing of the heat platen from the welding area (movement in negative direction along Z axis – z_2). Next the heated up ends of belting are pressed against each other by movement of the sliding gripper (7). Axial alignment of the end faces is ensured by alignment of the die holes through which the two ends pass.

After some time, sufficient for the seam to cool off the welding bead is removed. The process is effected by opening the fixed gripper (5) and then the sliding gripper (6) pulls the belt through the die. Initially the die moves together with the whole heater assembly (7) in the negative direction along the X (x_2) axis until it rests against the end stops fixed to the main frame (1). Moving further the sliding gripper (6) pulls the belt through profiled hole of the cutting die, thus cutting off excess material.

After that the heating dies are withdrawn to their initial positions and the sliding gripper opens. Now the finished belt can be removed from the machine by the operator. All the mechanisms return to their home positions in a way to avoid collisions.

The key aspect to ensure the desired operation are the electrical settings of the control system (Fig. 19). Besides quality of welding it ensures effectiveness and safety of the machine operation.

The main element of this control system is programmable logic controller (PLC) which has the watchdog function. The PLC is equipped with the communication module (MK) to support networking with other controlling or operating devices via RS485 serial interface. One of the networked elements is the human-machine interface providing the operating with status data (including number of completed belts) and information on the changes to the settings (such as heating up time).

The three drive units use AC servomotors (M1 – feeder drive system, M2 – fixed gripper rotation drive system and M3 – sliding gripper drive system). These units are controlled by dedicated controllers S1-S3 as they cannot be operated directly by PLC (Sreejeth et al., 2012). They control the operation of the AC ser-

vomotor, the electromagnetic brake and also the digital encoder. In order to obtain a consistent control cycle the controllers are connected with the PLC, HMI, between themselves and with other elements via the RS485 interface. Master/slave relationship is established between PLC and the servomotor controllers with the PLC acting as master. The devices are supplied with 230V power and in addition to their main function they deliver power to servomotors.
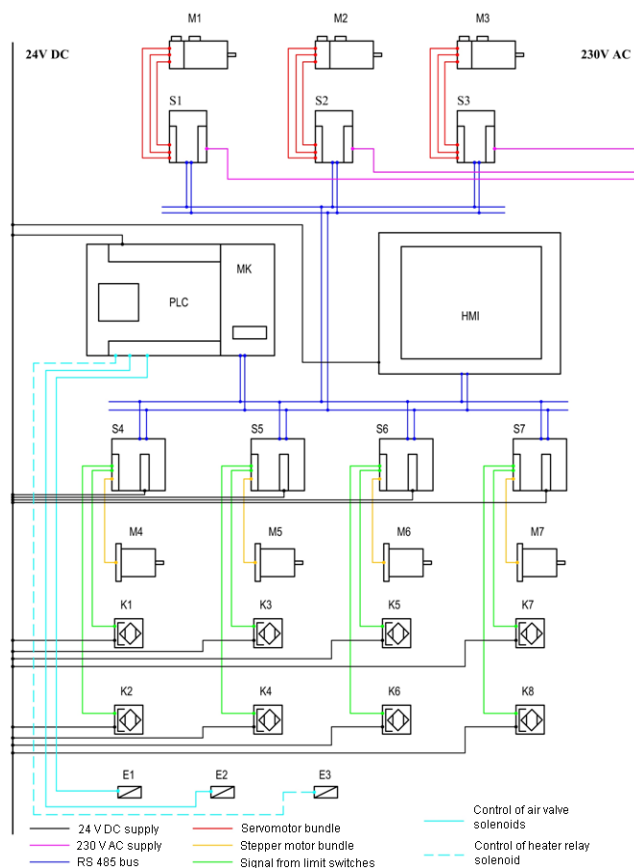

Fig. 19. Control system schematic: M1 – roll feeder servomotor, M2 – fixed gripper servomotor, M3 – sliding gripper servomotor, S1 – S3 – servomotor controller, PLC – central processing unit, MK – PLC communication module, HMI – human-machine interface, M4 – sliding gripper movement stepper motor, M5 – welding table lifting motor, M6 i M7– heating die movement stepper motor, S4 – S7 – stepper motor controller, K1 and K2 – gripper end-of-travel limit switch, K3 and K4 – welding table lifting limit switch, K5 – K8 heating dies end-of-travel limit switch, E1 – solenoid of shear cutter cylinder valve , E2 – solenoid of the heater cylinder valve, E3 – heater relay solenoid

The remaining electrical drive systems are based on bipolar, two-phase stepper motors (M4 – M7) powering the ball screw drives, equipped with end-of-travel limit switches (K1 – K8). The drive systems based on M6 and M7 motors (drives of the heating dies elements) are identical while the systems driving the fixed gripper and lifting the welding table (M4 and M5 respectively) have higher power, higher maximum allowable forces and different dimensions. Characteristics of stepper motor - maximum torque from start, and mild decline with increasing of rotational speed are matched to work specification of i.e. sliding gripper. (Kukla et al., 2016). The maximum torque is required to i.e. remove waste from welding process by move of the gripper.

The stepper motor cannot be controlled directly by PLC. Special controllers (S4 – S7) have been used to meet the control requirements. These devices are supplied with 24V power and while controlling the stepper motors they also transmit power. The system functionality is maintained owing to connecting the stepper motor controllers to RS485 interface in order to enable communication with the master controller (PLC) in master/slave configuration.

The reed limit switches (K1-K8) protect the drive systems from losing steps by the stepper motors.

The solenoid (E1) operates the spring return pneumatic valve 5/2 through which air is supplied to the shear cutter cylinder. The solenoid (E2) operates the valve supplying air to the heater cylinder. Activating both solenoids produces operating movements of the sub-assemblies connected with the respective cylinders and when they are disconnected the sub-assemblies return to their home positions. The solenoid (E3) activates the heater when the machine is starting up. With fixed working temperature of 200°C it can be controlled by the solenoid alone. All the solenoids are controlled directly from binary outputs of the PLC.

The control system design is based on commercially available devices.

5. CONCLUSIONS

Application of mechatronic design methods in designing industrial machine systems can lead to automation of various manual processes. Thus these processes can be carried out without operator's involvement. One of such processes is butt welding of round belting. The process is generally done by hand. Automation of the process requires designing a machine to perform all the operations of the process flow chart. The mechatronic assemblies are expected to improve the effectiveness of welding while ensuring satisfactory quality of the finished products.

There are several important factors to be taken into account in the design and implementation of the machines for automatic splicing of belting. The mechanical part of the machine must enable processing cords of specified geometry. It is also necessary to define the size range of finished products to be handled by the machine which will significantly influence the dimensions of the machine sub-assemblies. The control system must, on its part, execute the process flow chart that is quite complex in this case. Appropriately designed control is critical for good quality of welding. Communication with operator is also important. It is necessary to enable monitoring and adjustment of the current parameters, such as finished belt length. Last but not least, one should remember about safety of operation. It is important to protect both the machine and the people in its vicinity from unplanned situations associated with the characteristics of the processed material, such as uncontrolled unwinding of cord from the spool.

The design of the mechanical, as well as control systems of the machine, as described in this paper provides the basis for building a prototype of the designed machine. Whether or not any modifications should be implemented in the proposed design should be established on the basis of experimental verification of the machine functions and of the quality of splicing.

REFERENCES

1. **Amanat N., James N. L., McKenzie D.R**. (2010), Welding methods for joining thermoplastic polymers for the hermetic enclosure of medical devices, *Medical engineering & Physics,* Vol. 32, 690–699.
2. **Amancio-Filho S.T., dos Santos J.F.** (2009), Joining of Polymers and Polymer-Metal Hybrid Structures: Recent Developments and Trends, *Polymer Engineering and Science,* 49(8), 1461–1476.
3. **Ashby M.F., Jones D.R.H.** (1996), *Engineering materials (in Polish),* WNT, Warszawa.
4. **Behabelt** (2015), *Product Catalogue 2015/2016,* Behabelt, Glottertal.
5. **Casalino G., Ghorbel E.** (2008), Numerical model of CO_2 laser welding of thermoplastic polymers, *Journal of Materials Processing Technology*, 207, 63–71.
6. **Ciszewski A., Radomski T.** (1989), *Construction materials in machine design (in Polish),* PWN, Warszawa.
7. **Cocard M., Grozav I., Iacob M., Caneparu A.** (2009), Establishing the Optimum Welding Procedure for PE 100 Polyethylene Pipelines Using the Response Surface Design, *Materiale Plastice*, 46(4), 452–457.
8. **Domek G., Dudziak M.** (2011), Energy Dissipation in Timing Belts Made From Composite Materials, *Advanced Material Research,* 189– 193, 4414–4418.
9. **Domek G., Kołodziej A., Dudziak M., Woźniak T.** (2016), Identification of the quality of timing belt pulleys, *Procedia Engineering*, 177, 275–280.
10. **Domek G., Malujda I.** (2007), Modeling of timing belt construction*, Proceedings in Applied Mathematics and Mechanics*, 7, 45–46.
11. **Evers F., Schöppner V., Lakemeyer P.** (2017), The influence on welding processes on the weld strength of flame-retardant materials, *Weld World*, 61, 161–170.
12. **Inoue T., Miyata R., Hirai S.** (2016), Antagonistically Twisted Round Belt Actuator System for Robotic Joints, *Journal of Robotics and Mechatronics*, 28(6), 842 – 853.
13. **Jasiulek P.** (2006), *Joining of plastics by welding, glueing and laminating (in Polish),* Wydawnictwo "KaBe", Krosno.
14. **Klimpel A.** (1999), *Metals and thermoplastic polymers welding technology (in Polish),* Wydawnictwo Politechniki Śląskiej, Gliwice.
15. **Klimpel A.** (2000), *Welding of termoplastics materials (in Polish),* Wydawnictwo Politechniki Śląskiej, Gliwice.
16. **Kukla M., Tarkowski P., Malujda I., Talaśka K., Górecki J.** (2016), Determination of the torque characteristics of a stepper motor, *Procedia Engineering*, 136, 375–379.
17. **Madej M., Ozimina D.** (2010), *Plastics and composite materials (in Polish),* Wydawnictwo Politechniki Świętokrzyskiej, Kielce.
18. **Puszka A.** (2006), *Polyurethanes – sources, properties and modifications (in Polish),* Zakład Chemii Polimerów, Wydział Chemii Uniwersytetu Marii Curie Skłodowskiej w Lublinie, Lublin.
19. **Rzasinski R.**, (2017), The algorithm of verification of welding process for plastic pipes, IOP Conference Series: *Materials Science and Engineering,* 227, 012113.
20. **Sikora R.** (1993), *Proceeding macromolecular materials (in Polish),* Wydawnictwo ŻAK, Warszawa.
21. **Sreejeth M., Singh M., Kumar P.** (2012), Monitoring, Control and Power Quality Issues of PLC Controlled Three-Phase AC Servomotor Drive, *2012 IEEE Fifth Power India Conference*, 19-22 Dec. 2012, Murthal, India.
22. **Wanqing L., Changqing F., Xing Z., Youliang C., Rong Y., Donghong L.** (2017), Morphology and thermal properties of polyurethane elastomer based on representative structural chain extenders, *Thermochimica Acta*, 653, 116–125.
23. **Yousepour A., Hojjari M., Immarigeon J-P.** (2004), Fusion Bonding/Welding of Thermoplastic Composites, *Journal of Thermoplastic Composite Materials,* 17, 303–341.
24. **Żuchowska D.** (2000), *Construction polymers (in Polish),* WNT, Warszawa.

DYNAMIC ANALYSIS OF A ROD VIBRO-IMPACT SYSTEM
WITH INTERMEDIATE SUPPORTS

Volodymyr GURSKY[*], **Igor KUZIO**[*]

[*]Department of Mechanics and Automation Engineering, Institute of Engineering Mechanics and Transport,
Lviv Polytechnic National University, 12 Bandera Street, 79013 Lviv, Ukraine

vol.gursky@gmail.com, ikuzio@polynet.lviv.ua

Abstract: The two-mass resonant vibro-impact module is presented as the rod system with cylindrical intermediate supports. The corresponding design diagram is constructed. Based on the finite element method, the frequency of free oscillations is defined for the corresponding location of the intermediate supports. A stress-strain state of the elastic element is considered. The stiffness of the intermediate supports is defined by solving the contact problem between the cylindrical rod supports and the flat spring. The dynamics of the vibro-impact rod system with multiple natural frequencies is analyzed taking into account the contact stiffness of the intermediate supports. The determination of contact and equivalent stresses occurring during the operation of the vibro-impact rod system is performed.

Key words: Rod System, Electromagnetic Drive, Vibro-impact, Resonance, Finite Element Method (FEM)

1. INTRODUCTION

Vibromachines are widely used in industries with large energy consumption, especially in metallurgy, civil and mechanical engineering (Bednarski and Michalczyk, 2017; Nadutyi et al., 2013; Filimonikhin and Yatsun, 2017). This emphasizes their actuality. A large amount of vibromachines are of the vibro-impact type and fall under the category of nonlinear systems (Babitsky, 2013). They can operate both in non-resonant and in resonant mode (Luo et al., 2007; Sokolov et al., 2007). Resonant systems are energy efficient ones, so they have better prospects, despite the peculiarities of their operational parameters control (Despotović et al., 2014). Their structural basis is formed by nonlinear stiffness characteristics chiefly by piecewise-linear asymmetric characteristics (Krot, 2010; Yoon and Kim, 2015). They are the most usable ones in terms of implementation. Several elastic elements working in series are applied to implement an appropriate stiffness characteristic. One of them is a working element and the other one is a nonmetallic (rubber) movement limiter. The system is to be setup in order to ensure the resonance operation mode by changing the value of the stiffness coefficient of the metallic elastic element.

2. DESCRIPTION OF THE STRUCTURE
OF THE VIBRO-IMPACT SYSTEM

Fig. 1 shows a general view of a vibro-impact resonance module with an electromagnetic drive. It consist of two oscillatory masses (working mass 1 and reactive mass 2), which have the values of m_1 and m_2 and are joined by one flat spring 3. The oscillatory mass 1 is designed as a frame (body); the brackets 4 are fixed in their horizontal grooves. The metallic or non-metallic cylindrical rods 5, on which the flat spring 3 is lent, are assembled in vertical grooves of the brackets 4. The use of such movement limiters allow to implement various asymmetric characteristics of stiffness using one flat spring 4. Two alternating current electromagnets presented in a form of cores with coils 6 and armatures 7, which are placed on corresponding oscillatory masses, are used for system disturbance.
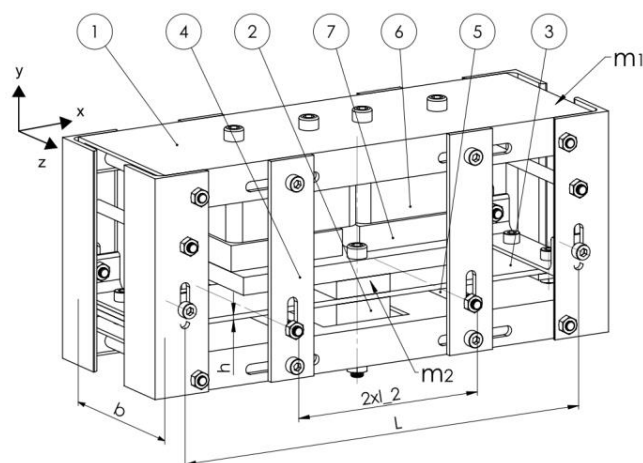

Fig. 1. General view of the two-mass resonance vibratory module:
1 – working mass, 2 – reactive mass, 3 – flat spring, 4 – brackets,
5 – intermediate supports (cylindrical rods),
6 – coils of electromagnets, 7 – armatures

The approach proposed for implementation of an asymmetric stiffness characteristic (Fig. 2) consists in the use of the limiter in a form of absolutely rigid supports contacting with the resonance elastic element. Herewith, the rational implementation of an asymmetric characteristic of a single stiffness element is possible

under the condition of coordination of the structural parameters with the frequency parameters of a vibratory machine, as well as with the tractive characteristic of a drive.
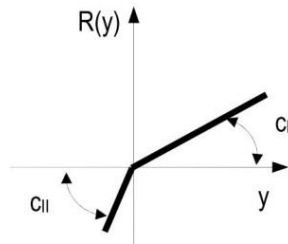

Fig. 2. Piecewise-linear asymmetric stiffness characteristic of a flat spring with intermediate supports

Investigations on the subject of dynamics and synthesis of the vibro-impact systems based on piecewise-linear asymmetric stiffness characteristics are presented in many research papers. Despite the fact that much attention is paid to the problems of dynamic analysis, in particular to the stability analysis and the study of nonlinear effects in a form of bifurcations and sub-resonances (Simon et al., 2014; Belovodskiy et al., 2015), it is essential to coordinate the main frequency and force characteristics of a particular design diagram with the appropriate inertial and geometrical parameters.

3. FEM MODEL AND FREQUENCY ANALYSIS

Considering the vibratory machines as the dynamic models, while carrying out the calculations, they can be presented as the rod systems (elements) with distributed or lumped parameters.

Fig. 3 shows an operational diagram of a resonance vibro-impact module implemented in a form of a rod system. The upward movement is implemented in diagram I without supports; the downward movement is represented in diagram II with rigid intermediate supports. The structural non-linearity in a form of the gapless asymmetrical stiffness characteristic (Fig. 2) is implemented with a help of a flat spring of bending stiffness EJ using rigid or relatively compliant movement limiters fixed on appropriate parts of an elastic element. Herewith, the real two-mass system can be transformed to the single mass system with the corresponding mass reduction to an inertial coefficient $m = \frac{m_1 m_2}{(m_1 + m_2)}$. Thus, the procedure of dynamic analysis is to be substantially simplified, in particular by the generalized coordinate $y(t)$.

Vibro-impact processes are attended by contact phenomena both in the mediums being treated and in the mechanical systems, in particular at the moment of switching the stiffness characteristic from the parameter c_I to the parameter c_{II}. Thus, it is important to take into account these effects while carrying out the complex analysis of a vibratory system for representation of the dynamic problem integrity and for studying the efficiency of the vibro-impact mode implementation.

The problems of frequency analysis of the elastic rod systems can be solved directly by analytical methods, as well as by approximate methods (Clough and Penzien, 1995) performing the finite and boundary elements analysis, or using the methods of Relay, Dunkerley, etc. The finite element method (FEM) has become very popular (Hutton, 2004) and it is the basis of all applications of computer analysis. Under appropriate conditions, the

original problem can be reduced to the final formulas applicable for performing the engineering calculations and the system designing.
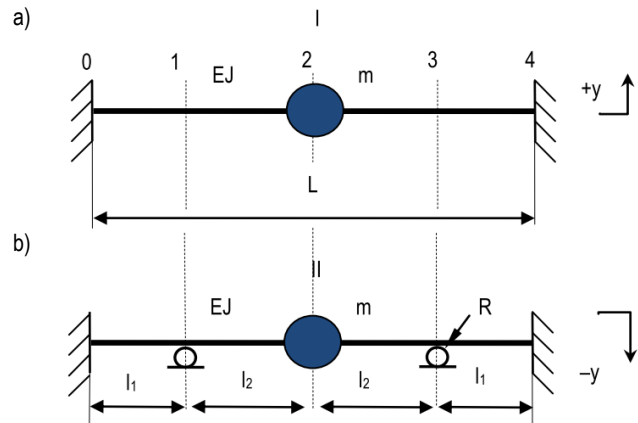
a)

b)

Fig. 3. Operational diagrams of the rod system implementing an asymmetric stiffness characteristic without (a) and with (b) the intermediate supports

The formula for determination of the natural frequency of bending oscillations of the rod system discrete model with the reduced mass m is presented as (Hutton, 2004):

$$\omega_{0I} = \sqrt{192EJ/mL^3}. \tag{1}$$

To ensure the prescribed natural frequency of free oscillations while performing the design calculation of bending stiffness EJ, the following formula is used:

$$EJ = \frac{mL^3 \omega_{0I}{}^2}{192}. \tag{2}$$

To construct the stiffness matrix of the presented rod system with a help of FEM, it is used the basic element in a form of the rod with four degrees of freedom: y_i, y_{i+1} and φ_i, φ_{i+1} are the vertical displacements and the angles of rotation of the utmost nodal points of the rod. The matrix of nodal reactions of the shearing forces and the bending moments is as follows (Hutton, 2004; Clough and Penzien, 1995):

$$[\overline{Z}_{i,i+1}] = \begin{Bmatrix} R_i \\ M_i \\ R_{i+1} \\ M_{i+1} \end{Bmatrix} = $$
$$EJ \begin{bmatrix} 12/l_i{}^3 & -6/l_i{}^2 & -12/l_i{}^3 & -6/l_i{}^2 \\ -6/l_i{}^2 & 4/l_i & 6/l_i{}^2 & 2/l_i \\ -12/l_i{}^3 & 6/l_i{}^2 & 12/l_i{}^3 & 6/l_i{}^2 \\ -6/l_i{}^2 & 2/l_i & 6/l_i{}^2 & 4/l_i \end{bmatrix}. \tag{3}$$

The matrix of reactions is used for constructing the diagrams of the stress-strain state of the rod system.

The finite element diagram for free bending oscillations analysis of the rod system presented in Fig. 3, b takes into account the corresponding boundary conditions:

$$\begin{pmatrix} y_0 = 0 \\ \varphi_0 = 0 \end{pmatrix}, \begin{pmatrix} y_1 = 0 \\ \varphi_1 = \text{var} \end{pmatrix}, \begin{pmatrix} y_2 = \text{var} \\ \varphi_2 = \text{var} \end{pmatrix},$$
$$\begin{pmatrix} y_3 = 0 \\ \varphi_3 = \text{var} \end{pmatrix}, \begin{pmatrix} y_4 = 0 \\ \varphi_4 = 0 \end{pmatrix}. \tag{4}$$

The stiffness matrix of 10×10 order of the separate finite elements-rods is constructed on the basis of the on generalized matrix (3) of the single rod in the absolute coordinate system taking into consideration the boundary conditions presented in (4).

$$\mathbf{C_{01}} = EJ \begin{bmatrix} 1 & 0 & 0 & 0 \\ 0 & 1 & 0 & 0 \\ 0 & 0 & 1 & 0 \\ 0 & 0 & 0 & 4/l_1 \end{bmatrix},$$

$$\mathbf{C_{12}} = EJ \begin{bmatrix} 1 & 0 & 0 & 0 \\ 0 & 4/l_2 & -6/l_2^2 & 2/l_2 \\ 0 & -6/l_2^2 & 12/l_2^3 & -6/l_2^2 \\ 0 & 2/l_2 & -6/l_2^2 & 4/l_2 \end{bmatrix},$$

$$\mathbf{C_{23}} = EJ \begin{bmatrix} 12/l_2^3 & 6/l_2^2 & 0 & 6/l_2^2 \\ 6/l_2^2 & 4/l_2 & 0 & 2/l_2 \\ 0 & 0 & 1 & 0 \\ 6/l_2^2 & 2/l_2 & 0 & 4/l_2 \end{bmatrix},$$

$$\mathbf{C_{34}} = EJ \begin{bmatrix} 1 & 0 & 0 & 0 \\ 0 & 4/l_1 & 0 & 0 \\ 0 & 0 & 1 & 0 \\ 0 & 0 & 0 & 1 \end{bmatrix}. \tag{5}$$

The stiffness matrix of the rod system with 10 degrees of freedom consisting of four rod elements (5) can be constructed by adding the separate stiffness matrixes in the absolute coordinate system, where the coefficients are to be added taking into account the corresponding generalized coordinates:

$$\mathbf{C_{04}} =$$

$$EJ \begin{bmatrix} 1 & 0 & 0 & 0 & 0 & 0 & 0 & 0 & 0 & 0 \\ 0 & 1 & 0 & 0 & 0 & 0 & 0 & 0 & 0 & 0 \\ 0 & 0 & 2 & 0 & 0 & 0 & 0 & 0 & 0 & 0 \\ 0 & 0 & 0 & \frac{4}{l_1}+\frac{4}{l_2} & \frac{-6}{l_2^2} & \frac{2}{l_2} & 0 & 0 & 0 & 0 \\ 0 & 0 & 0 & \frac{-6}{l_2^2} & \frac{24}{l_2^3} & 0 & 0 & \frac{6}{l_2^2} & 0 & 0 \\ 0 & 0 & 0 & \frac{2}{l_2} & 0 & \frac{8}{l_2} & 0 & \frac{2}{l_2} & 0 & 0 \\ 0 & 0 & 0 & 0 & 0 & 0 & 2 & 0 & 0 & 0 \\ 0 & 0 & 0 & 0 & \frac{6}{l_2^2} & \frac{2}{l_2} & 0 & \frac{4}{l_1}+\frac{4}{l_2} & 0 & 0 \\ 0 & 0 & 0 & 0 & 0 & 0 & 0 & 0 & 1 & 0 \\ 0 & 0 & 0 & 0 & 0 & 0 & 0 & 0 & 0 & 1 \end{bmatrix}. \tag{6}$$

The free oscillations equation of the rod system is written in the matrix form:

$$\mathbf{M} \times \ddot{\mathbf{X}} + \mathbf{C_{04}} \times \mathbf{X} = 0, \tag{7}$$

where $\mathbf{X} = \mathrm{column}(y_0, \varphi_0, \dots, y_4, \varphi_4)$ is the column vector of the nodal finite elements displacements; $\mathbf{M} = \mathrm{diag}(0,0,0,0,m,0,0,0,0,0)$ is the diagonal matrix of the inertial parameters of the localized masses; $\mathbf{C_{04}}$ is the system stiffness matrix.

The frequency equation of the rod system formed on the basis of the determinant

$$\det(-\mathbf{M} \times \Omega^2 + \mathbf{C_{04}}) = 0, \tag{8}$$

and allows to derivate the formula for calculation of the natural

frequency of free bending oscillations:

$$\omega_{0II} = \sqrt{6EJ(l_1 + 4l_2)/m(l_1 + l_2)l_2^3}. \tag{9}$$

According to the equations (1) and (9), the stiffness coefficients of the rod systems are as follows:

$$c_I = 192EJ/L^3, \quad c_{II} = 6EJ(l_1 + 4l_2)/(l_1 + l_2)l_2^3, \tag{10}$$

Taking into account that $l_2 = \frac{L}{2} - l_1$, the ratio of the stiffness coefficients can be presented as:

$$n_c = c_{II}/c_I = L^2(L - 1.5l_1)/(L - 2l_1)^3, \tag{11}$$

The ratio of the natural frequencies of free oscillations is as follows:

$$n_\omega = \omega_{0II}/\omega_{0I} = \sqrt{n_c}.$$

For example, introducing the multiplicity condition of the bending oscillations of the considered rod systems as

$$n_\omega = 2, \tag{12}$$

the formulas of determination of the intermediate supports location are derived:

$$l_1 = 0.275L, \quad l_2 = 0.225L, \tag{13}$$

considering that $l_1 + l_2 = 0.5L$.

Considering the stiffness of the intermediate supports. In fact, the intermediate supports cannot be absolutely rigid (Fig. 4). Their compliance can be influenced by the design of the corresponding limiters made of the non-metallic materials.
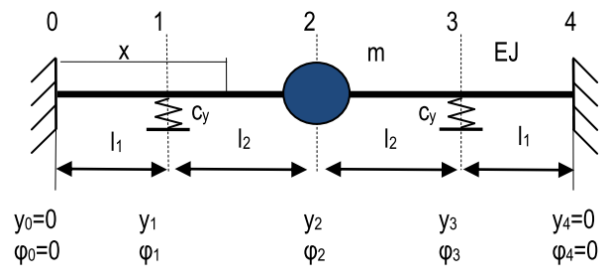

Fig. 4. Computational finite-element diagram and boundary conditions of the rod system with elastic intermediate supports

To take into account the stiffness coefficient c_y of the intermediate supports in a vertical direction, the resultant stiffness matrix $\mathbf{C_{04}}$ of the rod system is constructed. It takes into account the corresponding boundary conditions:

$$\begin{pmatrix} y_0 = 0 \\ \varphi_0 = 0 \end{pmatrix}, \begin{pmatrix} y_1 = \mathrm{var} \\ \varphi_1 = \mathrm{var} \end{pmatrix}, \begin{pmatrix} y_2 = \mathrm{var} \\ \varphi_2 = \mathrm{var} \end{pmatrix},$$

$$\begin{pmatrix} y_3 = \mathrm{var} \\ \varphi_3 = \mathrm{var} \end{pmatrix}, \begin{pmatrix} y_4 = 0 \\ \varphi_4 = 0 \end{pmatrix}, \tag{14}$$

and is presented as:

$$\mathbf{C_{04}} = EJ \begin{bmatrix} 1 & 0 & 0 & 0 & 0 & 0 & 0 & 0 & 0 & 0 \\ 0 & 1 & 0 & 0 & 0 & 0 & 0 & 0 & 0 & 0 \\ 0 & 0 & \frac{2c_y}{EJ} + \frac{12}{l_1^{\,3}} + \frac{12}{l_2^{\,3}} & \frac{6}{l_2^{\,2}} - \frac{6}{l_1^{\,2}} & \frac{-12}{l_2^{\,3}} & \frac{6}{l_2^{\,2}} & 0 & 0 & 0 & 0 \\ 0 & 0 & \frac{6}{l_2^{\,2}} - \frac{6}{l_1^{\,2}} & \frac{4}{l_1} + \frac{4}{l_2} & \frac{-6}{l_2^{\,2}} & \frac{2}{l_2} & 0 & 0 & 0 & 0 \\ 0 & 0 & \frac{-12}{l_2^{\,3}} & \frac{-6}{l_2^{\,2}} & \frac{24}{l_2^{\,3}} & 0 & \frac{-12}{l_2^{\,3}} & \frac{6}{l_2^{\,2}} & 0 & 0 \\ 0 & 0 & \frac{6}{l_2^{\,2}} & \frac{2}{l_2} & 0 & \frac{8}{l_2} & \frac{-6}{l_2^{\,2}} & \frac{2}{l_2} & 0 & 0 \\ 0 & 0 & 0 & 0 & \frac{-12}{l_2^{\,3}} & \frac{-6}{l_2^{\,2}} & \frac{2c_y}{EJ} + \frac{12}{l_1^{\,3}} + \frac{12}{l_2^{\,3}} & \frac{6}{l_1^{\,2}} - \frac{6}{l_2^{\,2}} & 0 & 0 \\ 0 & 0 & 0 & 0 & \frac{6}{l_2^{\,2}} & \frac{2}{l_2} & \frac{6}{l_1^{\,2}} - \frac{6}{l_2^{\,2}} & \frac{4}{l_1} + \frac{4}{l_2} & 0 & 0 \\ 0 & 0 & 0 & 0 & 0 & 0 & 0 & 0 & 1 & 0 \\ 0 & 0 & 0 & 0 & 0 & 0 & 0 & 0 & 0 & 1 \end{bmatrix}. \tag{15}$$

The formula for calculating the natural frequency of free oscillation of the system derived on the basis of the corresponding equation taking into account the stiffness matrix $\mathbf{C_{04}}$ mentioned above:

$$\Omega = 8 \sqrt{\frac{3EJLm(2c_yLl_1^{\,3} - 3c_yL^4 + 3EJL) \times \begin{pmatrix} 2c_yL^3l_1^{\,3} + 3EJL^3 - 12c_yL^2l_1^{\,4} + \\ +24c_yLl_1^{\,5} - 16c_yl_1^{\,6} \end{pmatrix}}{m\begin{pmatrix} 2c_yL^4l_1^{\,3} + 3EJL^4 - 12c_yL^3l_1^{\,4} + \\ +24c_yL^2l_1^{\,5} - 16c_yLl_1^{\,6} \end{pmatrix}}}. \tag{16}$$

The natural frequency of the system Ω is within $\omega_{0I} \leq \Omega \leq \omega_{0II}$ (Fig. 5) and approaches asymptotically to the value ω_{0II} with considerable increase of the stiffness coefficient c_y:

$$\lim_{c_y \to \infty} \Omega = \omega_{0II}, \tag{17}$$

Considering the real support stiffness c_y in the case of ensuring the appropriate value of the natural frequency requires adjustment of their location using the appropriate formula (16).
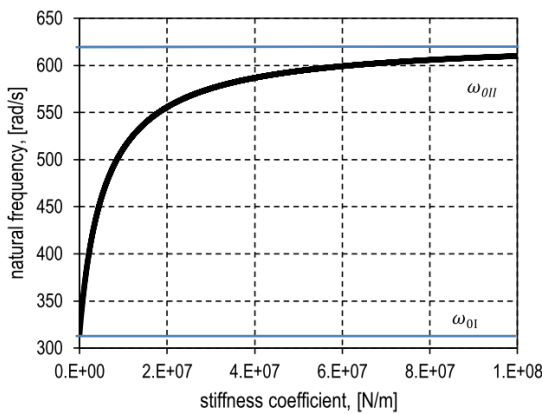

Fig. 5. Influence of the stiffness coefficient of the intermediate supports on the natural frequencies of oscillations of the rod system

The model being analyzed numerically has the following parameters: $\omega = 314\,\text{rad/s}$, $m = 20\,\text{kg}$, $L = 0.5\,\text{m}$, $E = 2.05 \times 10^5\,\text{MPa}$, $b = 0.080\,\text{m}$, $R = 0.006\,\text{m}$.

On the basis of the parameters presented above we can calculate the following values: $EJ = 1.284 \times 10^5\,\text{Nm}^2$, $l_1 = 0.113\,\text{m}$, $l_2 = 0.137\,\text{m}$, $h = 9.79 \times 10^{-3}\,\text{m}$, $c_I = 1.972 \times$

$10^6\,\text{N/m}$, $c_{II} = 7.888 \times 10^6\,\text{N/m}$, $\omega_{0I} = 314\,\text{rad/s}$, $\omega_{0II} = 628\,\text{rad/s}$.

4. FORCE ANALYSIS AND STIFFNESS CHECK-UP

The vector of the nodal displacements for statically loaded rod system of mode II can be defined by equation:

$$\mathbf{Y} = \mathbf{C_{04}}^{-1} \times \mathbf{P}, \tag{18}$$

where $\mathbf{P}$ is the vector of external loads reduced to nodes.

The nodal displacements vectors of each finite element-rod are constructed using the matrix equation (18) in the form of state vectors:

$$\mathbf{Y_{01}} = \begin{bmatrix} y_0 \\ \varphi_0 \\ y_1 \\ \varphi_1 \end{bmatrix}, \mathbf{Y_{12}} = \begin{bmatrix} y_1 \\ \varphi_1 \\ y_2 \\ \varphi_2 \end{bmatrix},$$

$$\mathbf{Y_{23}} = \begin{bmatrix} y_2 \\ \varphi_2 \\ y_3 \\ \varphi_3 \end{bmatrix}, \mathbf{Y_{34}} = \begin{bmatrix} y_3 \\ \varphi_3 \\ y_4 \\ \varphi_4 \end{bmatrix}. \tag{19}$$

The vectors of the nodal reactions of each finite element are determined using the matrix equation (3). Plotting a deflection curve of each finite element-rod is performed based on the known shape functions for unit nodal displacement (Shigley, 2011) defined by (20).

$$y_{01}(x) = \begin{bmatrix} \frac{(2x^3 - 3l_1x^2 + l_1^{\,3})}{l_1^{\,3}} \\ \frac{(x^3 - 2l_1x^2 + l_1^{\,2}x)}{l_1^{\,2}} \\ \frac{(-2x^3 + 3l_1x^2)}{l_1^{\,3}} \\ \frac{(x^3 - l_1x^2)}{l_1^{\,2}} \end{bmatrix} \times \mathbf{Y_{01}},$$

$$y_{12}(x) = \begin{bmatrix} \frac{(2(x-l_1)^3 - 3l_2(x-l_1)^2 + l_2^{\,3})}{l_2^{\,3}} \\ \frac{((x-l_1)^3 - 2l_2(x-l_1)^2 + l_2^{\,2}(x-l_1))}{l_2^{\,2}} \\ \frac{(-2(x-l_1)^3 + 3l_2(x-l_1)^2)}{l_2^{\,3}} \\ \frac{((x-l_1)^3 - l_2(x-l_1)^2)}{l_2^{\,2}} \end{bmatrix} \times \mathbf{Y_{12}},$$

$$y_{23}(x) = \begin{bmatrix} \frac{\left(2(x-l_1-l_2)^3 - 3l_2(x-l_1-l_2)^2 + l_2{}^3\right)}{l_2{}^3} \\ \frac{\left(\begin{array}{c}(x-l_1-l_2)^3 - 2l_2(x-l_1-l_2)^2 + \\ +l_2{}^2(x-l_1-l_2)\end{array}\right)}{l_2{}^2} \\ \frac{\left(-2(x-l_1-l_2)^3 + 3l_2(x-l_1-l_2)^2\right)}{l_2{}^3} \\ \frac{\left((x-l_1-l_2)^3 - l_2(x-l_1-l_2)^2\right)}{l_2{}^2} \end{bmatrix} \times \mathbf{Y_{23}},$$

$$y_{34}(x) = \begin{bmatrix} \frac{\left(\begin{array}{c}2(x-l_1-2l_2)^3 - 3l_1(x-l_1-2l_2)^2 + \\ +l_1{}^3\end{array}\right)}{l_1{}^3} \\ \frac{\left(\begin{array}{c}(x-l_1-2l_2)^3 - 2l_1(x-l_1-2l_2)^2 + \\ +l_1{}^2(x-l_1-2l_2)\end{array}\right)}{l_1{}^2} \\ \frac{\left(-2(x-l_1-2l_2)^3 + 3l_1(x-l_1-2l_2)^2\right)}{l_1{}^3} \\ \frac{\left((x-l_1-2l_2)^3 - l_1(x-l_1-2l_2)^2\right)}{l_1{}^2} \end{bmatrix} \times \mathbf{Y_{34}}. \tag{20}$$

The total displacements and the rod deflection curve of the system II are determined using the following dependences:

$$y(x) = \begin{cases} y_{01}(x), & 0 \leq x \leq l_1, \\ y_{12}(x), & l_1 < x \leq l_1 + l_2, \\ y_{23}(x), & l_1 + l_2 < x \leq l_1 + 2l_2, \\ y_{34}(x), & l_1 + 2l_2 < x \leq 2(l_1 + l_2). \end{cases} \tag{21}$$

The stress state of the system is defined by the values of the bending moment, the shearing force, the normal and the shear stresses:

$$M(x) = EJ\frac{d^2}{dx^2}y(x), \; Q(x) = EJ\frac{d^3}{dx^3}y(x), \tag{22}$$

$$\sigma(x) = M(x)/W, \; \tau(x) = Q(x)S_{max}/bJ,$$

where $S_{max} = bh^2/8$, $J = bh^3/12$, $W = bh^2/6$ are the geometrical characteristics of the flat spring's cross section; b and h are the width and the thickness of the flat spring, correspondingly.

If the nodal loads vector is presented as the concentrated force with the amplitude value F, which acts on the local oscillatory mass in the central cross-section, thus, by solving equations (18), (20)-(22), in turn, we obtain the corresponding diagrams of deflection, rotation angle, shearing forces and bending moments when the rod bends. Calculation of the maximum equivalent stresses in the corresponding cross-sections of the elastic element and for the corresponding design diagrams is very important for the proposed variant of implementation of the asymmetric stiffness characteristic.

The values of the maximal bending stresses are defined using the well-known formulas (the indexes denote the stresses for corresponding design diagrams):

$$\sigma_{maxI} = \frac{M_{maxI}}{W}, \; \sigma_{maxII} = \frac{M_{maxII}}{W}, \tag{23}$$

where $M_{maxI} = \frac{FL}{8}$, $M_{maxII} = [\overline{\mathbf{Z}}_{12}]_4 = \frac{Fl_2(l_1+2l_2)}{2(l_1+4l_2)}$ are the maximal bending moments in the dangerous cross-sections of the rod systems discussed.

The maximal shearing stress in the central cross-sections of the rod can be defined as:

$$\tau_{maxI} = \tau_{maxII} = \frac{1.5F}{bh}, \tag{24}$$

The equivalent von Mises bending stress is as follows:

$$\sigma_{eq} = \sqrt{\sigma_{max}{}^2 + 4\tau_{max}{}^2}. \tag{25}$$

The stress-strain state analysis of the rod systems can be carried out by the value of the displacement y_m of the local mass or by the value of the restoring force which is defined by the given displacement for the corresponding diagrams using the appropriate formulas: $F_I = c_I y_m$, $F_{II} = c_{II} y_m$. Considering that $y_m = 0.24$ mm, we obtain the diagram of the form I with $\sigma_{eqI} = 23.2$ MPa; for the diagram of the form II we obtain $\sigma_{eqII} = 59.5$ MPa. The diagram of the deflection and equivalent stresses for a half of the elastic element (considering symmetry of the rod system) is presented in Fig. 6.
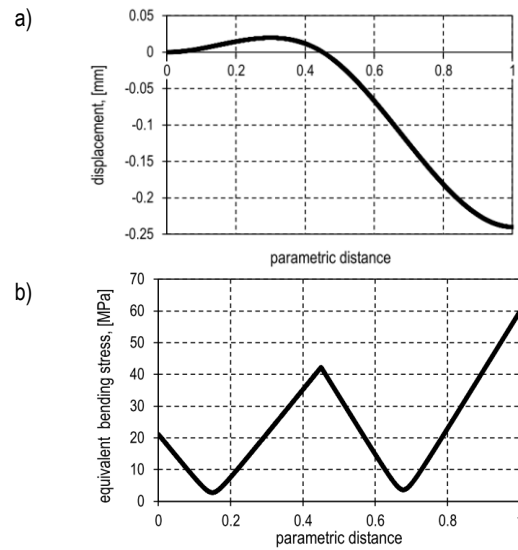

Fig. 6. Graphical dependencies of deflection (a) and equivalent bending stress (b) for the half-rod

Considering the reactions in the intermediate supports (caused by the shearing force), the check on the contact stresses between the cylindrical support and the flat spring is carried out based on Hertzian contact stress theory. The contact pressure is defined by the corresponding formula (Shigley, 2011):

$$p_{max} = \frac{2Q_1}{\pi bt}, \tag{26}$$

where $t = K_t\sqrt{Q_1}$; $K_t = \sqrt{\frac{2}{\pi b}\frac{\frac{1-\mu_1{}^2}{E_1} + \frac{1-\mu_2{}^2}{E_2}}{\frac{1}{2R}}}$; b is the length of the contact area (i.e., the width of the flat spring); R is the radius of the intermediate support; E_1, E_2 and μ_1, μ_2 are the elasticity modula and the Poisson's ratio of the materials being in the contact; Q_1 is the support action on a spring, which can be determined at the sum of reactions (shearing forces) in the rod's node:

$$Q_1 = |[\overline{\mathbf{Z}}_{01}]_3 + [\overline{\mathbf{Z}}_{12}]_1| = \frac{F_{II}\left(l_1{}^2 + 4l_1l_2 + 3l_2{}^2\right)}{2l_1(l_1 + 4l_2)}. \tag{27}$$

The components of the spatial stressed state vector are determined by the following formulas (Shigley, 2011):

$$\sigma_x = -p_{max}\left(\frac{1+2\zeta_b{}^2}{\sqrt{1+\zeta_b{}^2}} - 2|\zeta_b|\right),$$

$$\sigma_y = -p_{max}\frac{1}{\sqrt{1+\zeta_b{}^2}}, \tag{28}$$

$$\sigma_z = -2\mu_1 p_{max}\left(\sqrt{1+\zeta_b{}^2} - |\zeta_b|\right).$$

where $\zeta_b = y/t = 0.786$ is used for the calculations considering the maximal stress values.

Herewith, the main stresses are equal to the following axial components:

$$\sigma_1 \equiv \sigma_x, \ \sigma_2 \equiv \sigma_z, \ \sigma_3 \equiv \sigma_y. \tag{29}$$

The maximal shear stress and the equivalent stress in the contact zone are as follows:

$$\tau_{max} = \frac{\sigma_1 - \sigma_3}{2}, \tag{30}$$

$$\sigma_{max}{}^{(contact)} = \sqrt{\frac{1}{2}[(\sigma_1 - \sigma_2)^2 + (\sigma_2 - \sigma_3)^2 + (\sigma_3 - \sigma_1)^2]}. \tag{31}$$

The compliance of the intermediate supports depends on the relative displacement Δ_c of the flat spring and the support in contact zone can be determined by the following equation (Pisarenko et al., 1988):

$$\Delta_c = 0.83\sqrt[3]{\frac{Q_1{}^2}{R}\left(\frac{1-\mu_1{}^2}{E_1} + \frac{1-\mu_2{}^2}{E_2}\right)^2}. \tag{32}$$

The stiffness coefficient in the contact zone is $c_y = Q_1/\Delta_c$. For steel-steel contact problem the formulas are as follows:

$$\Delta_c = 1.23\sqrt[3]{\left(\frac{Q_1}{E}\right)^2\frac{1}{R}}, \tag{33}$$

$$c_y = 0.81\sqrt[3]{Q_1 R E^2}. \tag{34}$$

The last formula allows taking into account contact stiffness of the intermediate supports during implementation of the vibro-impact operation modes. In particular, assuming that its value is parametrically dependent on the contact force, we obtain the dependence of contact stiffness on the instantaneous displacement $y(t)$ of the local mass.

5. DYNAMIC ANALYSIS

In order to perform the dynamic analysis (Dyachenko et al., 2017), there is studied a model of forced oscillations taking into account instantaneous change of the frequency parameters of the rod system due to switching the stiffness characteristics and considering the contact stiffness of the intermediate supports:

$$y''(t) + 2n \cdot y'(t) + \begin{cases} \omega_{0I}{}^2 \cdot y(t), & y(t) \geq 0 \\ \Omega_{0II}[y(t)]^2 \cdot y(t), & y(t) < 0 \end{cases} = f \cdot \sin(\omega t), \tag{35}$$

where: $n = b/2m$, $b = 2m\omega\zeta$, $\zeta = 0.15$, $f = F/m$, $F = 600$ N.

The kinematic characteristics (Fig. 7) of the local oscillating mass motion are obtained using the numerical method RADAU while solving (35). The characteristics have asymmetric nature confirming the presence of the vibro-impact mode.
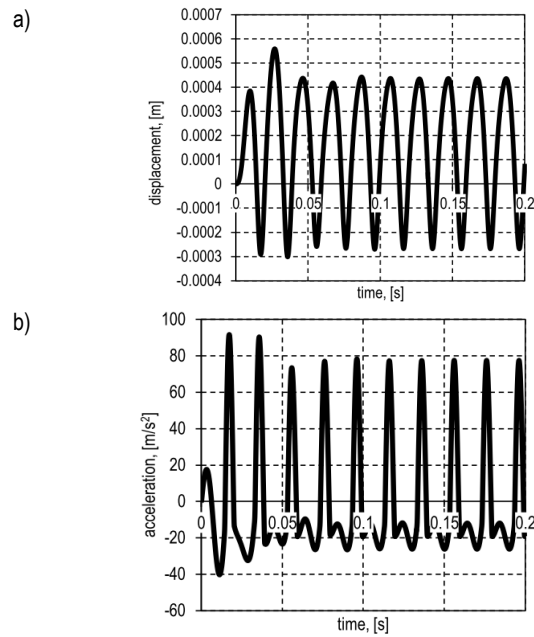

Fig. 7. Time dependencies of the dynamic displacement (a) and the acceleration (b) of the local mass

The obtained system has the following amplitude-frequency characteristic (Fig. 8), the resonance peak of which is determined by the following value of the natural frequencies of free oscillations (Yevstignejev, 2008):

$$\Omega_0 = \frac{2\omega_{0I}\omega_{0II}}{\omega_{0I} + \omega_{0II}} = 418.67 \frac{rad}{s}. \tag{36}$$
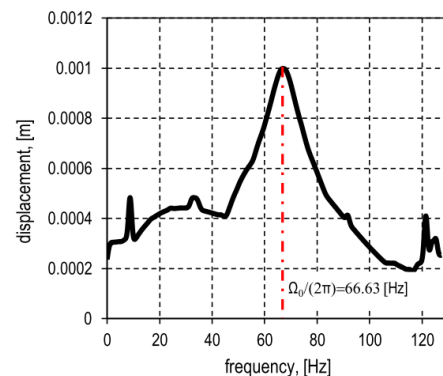

Fig. 8. Amplitude-frequency characteristic of the system

Multiple subharmonic and superharmonic resonances, which are analyzed in publications of Belovodskiy (2015), Luo (2007, 2009) and Simon (2014), can be observed on the obtained amplitude-frequency characteristic (Fig. 8).

Considering that in Eg. (27) the contact force depends on the instantaneous displacement $y(t)$ of the local mass, the parametric dependency of the contact stiffness on the contact force is constructed in Fig. 9 and has the explicitly nonlinear character.
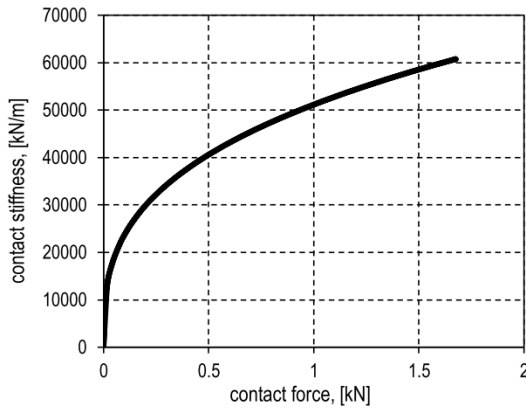
Fig. 9. Dependency of the stiffness coefficient of the intermediate support on the contact force (on the local mass displacement)

Herewith, the equivalent bending stress and the contact force are determined by the working conditions of the rod system:

$$\sigma_{eq}(t) = \begin{cases} \sigma_{eqI}(t), y(t) \ge 0, \\ \sigma_{eqII}(t), y(t) < 0, \end{cases} \quad (37)$$

$$Q_c(t) = \begin{cases} 0, y(t) \ge 0, \\ \dfrac{F_{II}[y(t)]\left(l_1{}^2 + 4l_1 l_2 + 3l_2{}^2\right)}{2l_1(l_1 + 4l_2)}, y(t) < 0, \end{cases} \quad (38)$$

where $F_{II}[y(t)] = c_{II}[y(t)]y(t) = m\Omega[y(t)]^2 y(t)$ is the restoring force in the central cross-section of the rod system.

The instant dependencies of the equivalent bending stresses and the contact stresses are presented in Fig. 10 and have the asymmetric impulsive character. The obtained results shows that the maximum values of the bending and contact stresses take place during the contact of the flat spring with the cylindrical supports.
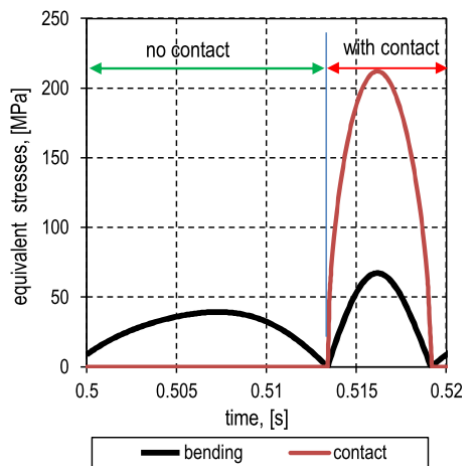

Fig. 10. Time dependency of the equivalent bending stresses and the contact stresses of the vibro-impact rod system

The bending stress is changing linearly and the contact stress is nonlinear in relation to the displacement of the local mass (Fig. 11, a). As an additional result, let us present the parametric dependency of the calculated stress values (Fig. 11a) and the restoring force of the flat spring (Fig. 11b) in respect to the instantaneous displacement of the local mass.
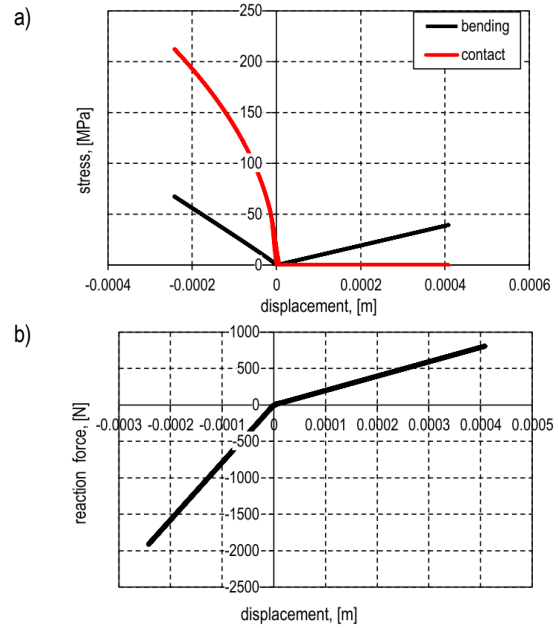

Fig. 11. Parametric dependency of the calculated stress values (a) and the restoring force (b) of the spring in respect to the displacement of the local mass

The synthesized asymmetric stiffness characteristic taking into account compliance of the intermediate supports (contact zone pliability) can be presented as:

$$R[y(t)] = \begin{cases} c_I y(t), y(t) \ge 0 \\ c_{II} y(t), y(t) < 0 \end{cases}.$$

Subsequently, the considered elastic element can be calculated by well-known techniques in order to ensure necessary durability and endurance taking into account bending and contact stiffness and stress asymmetry (Kogaev, 1977). The similar results are presented in the publication (Gursky and Kuzio, 2016). Complex accounting of the bending and contact stresses is carried out using the reduced coefficient of strength, which should not exceed the permissible value.

6. CONCLUSIONS

A complex dynamic analysis of the vibro-impact system based on the rod system is carried out using the finite element method. Compliance of the intermediate supports is considered and the analytical equation for calculating the natural frequency of free oscillations of such system is derived. The calculations of the contact stiffness are presented and modeling of oscillations of the vibro-impact system is performed taking into account stiffness of the intermediate supports. On the basis of the results of the dynamic analysis the stresses checking is carried out considering the bending conditions and the contact stiffness. The expediency of this approach is substantiated by the obtained formulas which are used while carrying out design calculations and allow to perform the efficiency evaluation of the vibro-impact modes implementation meeting the requirement imposed on strength of the basic system's element.

REFERENCES

1. **Babitsky V.** (2013), *Theory of vibro-impact systems and applications*, Springer Science & Business Media.
2. **Bednarski Ł., Michalczyk J.** (2017), Modelling of the working process of vibratory conveyors applied in the metallurgical industry, *Archives of Metallurgy and Materials*, 62(2), 721–728.
3. **Belovodskiy V.N., Bukin S.L., Sukhorukov M.Y., Babakina A.A.** (2015), 2:1 superharmonic resonance in two-masses vibrating machine, *Journal of Vibration Engineering & Technologies*, 3(2), 123–135.
4. **Clough Ray W., Joseph Penzien.** (1995), *Dynamics of Structures*, Berkeley: Computers & Structures.
5. **David V. Hutton.** (2004), *Fundamentals of finite element analysis*, Editorial McGraw − Hill, USA.
6. **Despotović Ž.V., Lečić M., Jović M. R., Durić A.** (2014), Vibration control of resonant vibratory feeders with electromagnetic excitation, *FME Transactions*, 42(4), 281–289.
7. **Dyachenko P., Chychuzhko M., Al-Ammouri A.** (2017). Development and application of computer model to study the modes of dynamic loading in mechanical oscillatory systems. *Eastern-European Journal of Enterprise Technologies*, 1(85), 42–49.
8. **Filimonikhin G., Yatsun V.** (2017). Conditions of replacing a single-frequency vibro-exciter with a dual-frequency one in the form of passive auto-balancer. *Naukovyi Visnyk Natsionalnoho Hirnychoho Universytetu*, 1, 61–68.
9. **Gursky V., Kuzio I.** (2016), Strength and durability analysis of a flat spring at vibro-impact *loadings*, *Eastern-European Journal of Enterprise Technologies*, 5, 7(83), 4–10.
10. **Kogaev V.P.** (1977), *Raschetu na prochnost pry napriazhenyiakh, peremennukh vo vremeny* [*Calculation of strength under stresses variable in time*], Mashinostroenie, Moscow, (in Russian).
11. **Luo G., Ma L., Lv X.** (2009), Dynamic analysis and suppressing chaotic impacts of a two-degree-of-freedom oscillator with a clearance, *Nonlinear Analysis: Real World Applications*, 10(2), 756–778.
12. **Luo G., Zhang Y., Xie J., Zhang J.** (2007), Vibro-impact dynamics near a strong resonance point, *Acta Mechanica Sinica*, 23(3), 329–341.
13. **Nadutyi V.P., Sukharyov V.V., Belyushyn D.V.** (2013), Determination of stress condition of vibrating feeder for ore drawing from the block under impact loads, *Metallurgical & Mining Industry*, 5(1), 24–26.
14. **Pavel V. Krot.** (2010), Dynamics and diagnostics of the rolling mills drivelines with non-smooth stiffness characteristics, *Proceedings of the 3rd International Conference on Nonlinear Dynamics*, Kharkov, Ukraine, 115–120.
15. **Pisarenko G.S., Yakovlev A.P., Matveev V.V.** (1988), *Spravochnyk po soprotyvlenyyu materyalov* [*Handbook on strength of materials*, Naukova Dumka, Kiev, (in Russian).
16. **Shigley Joseph Edward.** (2011), *Shigley's mechanical engineering design*, Tata McGraw-Hill Education.
17. **Simon P., Reuss P, Gaul L.** (2014), Identification of sub- and higher harmonic vibrations in vibro-impact systems, *Nonlinear Dynamics*, 2, 131–140.
18. **Sokolov I.J., Babitsky V.I., Halliwell N.A.** (2007), Autoresonant vibro-impact system with electromagnetic excitation, *Journal of Sound and Vibration*, 308, 375–391.
19. **Vladislav Yevstignejev** (2008), *Application of the complete bifurcation groups method for analysis of strongly nonlinear oscillators and vbro-impact systems*, Riga, Summary.
20. **Yoon J. Y., Kim B.** (2015), Vibro-impact energy analysis of a geared system with piecewise-type nonlinearities using various parameter values, *Energies*, 8(8), 8924–8944.

ELECTRONIC SPECKLE PATTERN INTERFEROMETRY FOR VIBRATIONAL ANALYSIS OF CUTTING TOOLS

Piotr MROZEK*, Ewa MROZEK**, Andrzej WERNER*

*Faculty of Mechanical Engineering, Department of Materials and Production Engineering, Bialystok University of Technology,
Wiejska 45C, 15-351 Bialystok, Poland
**Faculty of Mechanical Engineering, Department of Mechanics and Applied Computer Science, Bialystok University of Technology,
Wiejska 45C, 15-351 Bialystok, Poland

p.mrozek@pb.edu.pl, e.mrozek@pb.edu.pl, a.werner@pb.edu.pl

Abstract: A Michelson interferometer based ESPI system for static and vibration out of plane displacement measurements is presented. The aim of the article is to demonstrate the usability of ESPI non-contact measurement method in the field of machining. The correlation fringe patterns were visualized using custom software. The accuracy of ESPI interferometer was verified by the comparison with measurement results collected using industrial XL-80 laser system. The efficacy in vibration analysis was tested by studying the mode shapes and resonant frequencies of the transverse vibrations of square plates. The measurement methodology was used to determine natural frequencies and the shapes of vibrational modes of NFTe 100x1.2/64-II circular slitting saw. As a result the values of rotational speed that should be avoided during machining were determined.

Key words: Interferometry, Speckle Pattern, Correlation Fringes, Vibrational Analysis

1. INTRODUCTION

Advanced optical measurement methods, due to their high sensitivity and non-contact character, have been widely accepted both in scientific research and industry as a tool for displacement and vibrations analysis. Electronic speckle pattern interferometry (ESPI) is the most sensitive and accurate optical method for full-field three-dimensional (3D) displacement assessment (Fu and Moosa, 2002; Hild and Roux, 2006; Yang et al., 2014). In experimental non-contact vibration analysis time-averaged amplitude fluctuation (AF)-ESPI is the most widely used optical method. The advantage of AF-ESPI method is that both resonant frequencies and the corresponding mode shapes for transverse (out of plane) modes can be obtained. Experimentally revealed correlation fringe patterns of AF-ESPI correspond to the natural vibrational modes. So far, several different ESPI systems have been commercialized (Dantec Dynamics, Laser Technology Inc.), nevertheless due to significant progress made in corresponding fields of modern technology: laser sources, computer equipment and high resolution CCD and CMOS detector arrays, a variety of robust custom constructions of ESPI systems have been worked out by different research groups (Augulis et al., 2004; Quin et al., 2016). ESPI has been applied to experimentally verify the analytical and numerical models of applied mechanics (Halama et al., 2016), vibration theory (Chi-Hung et al., 2004), in automotive industry (Beeck and Hentschel, 2000; Ven der Auweraer et al., 2002), materials engineering (Richardson et al., 1998), biomedical area (Yang et al., 2014), micro-electro-mechanical systems (MEMS) (Foitzik et al., 2003) and in many other fields of science and engineering.

A field in which knowledge of frequencies of natural vibrations and natural vibrational modes plays a significant role is mechani-

cal engineering and the engineering of cutting tools (Rothberg and Bell, 2004; Tatar and Gren, 2008). Vibrations of tools and components of cutting machines directly affect machining accuracy, geometric structure of the product surface and the noise generated during machining. Until now relatively little attention has been paid to experimental research of vibrations of cutting tools using AF-ESPI. In the present study a Michelson interferometer based ESPI system for static and vibration out of plane displacement measurements is presented. The instrument was built using components actually available as standard. Custom software was worked out to visualize the correlation fringe patterns. The accuracy of the device was verified by the comparison with measurement results collected using industrial laser interferometer and the efficacy in vibration analysis was tested by studying the mode shapes and resonant frequencies of the transverse vibrations of square plates. A usefulness of the measurement methodology in the field of machining was revealed by the determination of natural frequencies and the shapes of vibrational modes of a circular slitting saw. The results may help to select the appropriate parameters of machining in order to minimize tool vibrations affecting roughness of the machined surface and noise generated during machining.

2. MATERIALS AND METHODS

2.1. Michelson ESPI interferometer construction

A schematic diagram of the setup of a Michelson interferometer based ESPI system is shown in Fig. 1. The subassemblies of the system were fixed to a massive cast iron frame to minimize

Piotr Mrozek, Ewa Mrozek, Andrzej Werner
Electronic Speckle Pattern Interferometry for Vibrational Analysis of Cutting Tools

DOI 10.2478/ama-2018-0021

the magnitude of eventual vibrational noise affecting the measurement accuracy. A light beam of He-Ne laser source 1 (12 mW, λ = 632.8 nm) was diverged by a glass lens 2 and fell on a beam splitter 3. The beam was divided into two equal intensity coherent beams, which illuminated two surfaces: S_0 (object surface 4) and S_r (reference surface 5). The surfaces were coated with thin (0.05 mm thickness) white color light diffusive self-adhesive foil. Speckle patterns were generated by these surfaces. The speckle patterns after passing through a beam splitter and the camera 6 lens met and interfered with each other in the image plane of a CCD sensor of the camera (1/3" SONY EXview HAD CCD II). The aperture of the camera lens was fitted to adjust the size of the speckle to the size of a pixel of the CCD array. The average size of a speckle was slightly greater than the diagonal length of a pixel of the sensor. The relative intensities of the two beams were adjusted by the arrangement of S_0 and S_r surface position. The exposure time of the camera was adjusted to acquire an image without saturating the CCD sensor. Bitmap files of 768x576 resolution were acquired by a video capture card installed in a PC. Deformations were applied to S_0 surface with S_r undisturbed surface serving as a reference. An initial speckle pattern image was acquired when no extortion was applied to S_0 surface. Subtraction of an actual speckle pattern image from the initial speckle pattern image was accomplished by a custom software. The resulting correlation fringes were displayed on a PC monitor screen and transferred to the hard disc of PC with 40 Hz frequency. For a static deformation of S_0 surface a stationary correlation fringe pattern was obtained as a result of an actual from the initial speckle images subtraction. In a case of natural vibration analysis a loudspeaker driven by a function generator and an acoustic amplifier was used as the source of an excitation wave. When a vibrating frequency was in the neighborhood of the resonant frequency of object surface S_0, stationary correlation fringes were observed. The fringes became the most clear and intensive as the resonant frequency was approached. The resonant frequencies and corresponding mode shapes could be determined at the same time.
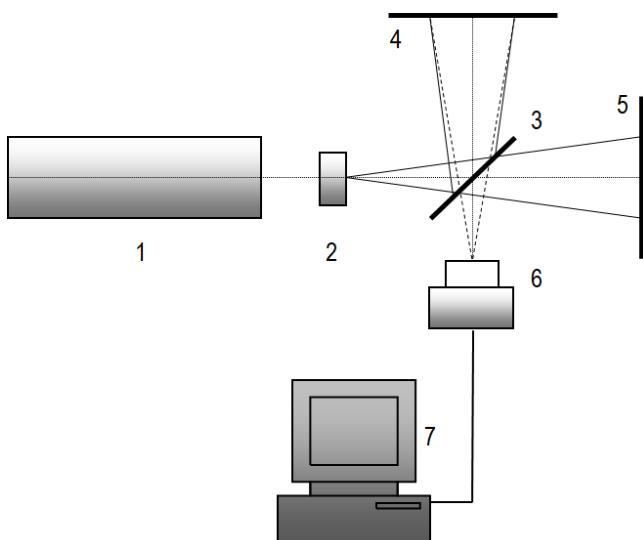

Fig. 1. Schematic diagram of ESPI setup: 1 – He-Ne laser, 2 – lens, 3 – beam splitter, 4 – object surface S_0, 5 – reference surface S_r, 6 – CCD camera, 7 – PC with a video capture card and a custom software for speckle patterns processing

2.2. Basic principle of ESPI out of plane displacement measurements

The wavefronts of the object (U_0) and reference (U_r) beam reflected from S_0 and S_r surfaces (Fig. 1), respectively, can be expressed as (Yang et al., 2014):

$$U_0 = a_0 \sin(\omega t + \varphi_0) \tag{1}$$

$$U_r = a_r \sin(\omega t + \varphi_r) \tag{2}$$

where a_0 and a_r are amplitudes of electric field strength, ω is an angular frequency of a light wave, φ_0 and φ_r represent the phase of the object beam and the reference beam, respectively (Yang et al., 2014). U_0 and U_r are functions of plane x, y coordinates. Intensity I of the speckle pattern image acquired by the CCD sensor can be written as:

$$I = a_0^2 + a_r^2 + 2a_0 a_r \cos(\varphi_0 - \varphi_r) \tag{3}$$

The argument in parentheses in Eq. (3) can be described as a phase difference:

$$\Theta = \varphi_0 - \varphi_r \tag{4}$$

Eq. (3) can be written as:

$$I = I_0(1 + \gamma \cos\Theta) \tag{5}$$

where:

$$I_0 = a_0^2 + a_r^2 \tag{6}$$

is the background intensity and

$$\gamma = \frac{2a_0 a_r}{a_0^2 + a_r^2} \tag{7}$$

is the contrast. When surface S_0 is deformed (with S_r surface undisturbed), the intensity of the speckle pattern becomes:

$$I = I_0(1 + \gamma \cos(\Theta + \Delta)) \tag{8}$$

where Δ represents the phase difference shift of the speckle pattern before and after S_0 deformation:

$$\Delta = \varphi'_0 - \varphi_0 \tag{9}$$

For a Michelson-type interferometer the relationship between phase change Δ and displacement w of surface S_0 can be written as:

$$\Delta = \frac{4\pi}{\lambda} w \tag{10}$$

For $\Delta = 2\pi$ which corresponds to transition between the centers of two adjacent fringes of order i and $(i + 1)$ in a correlation image, from Eq. (10) one can obtain:

$$w = \frac{\lambda}{2} \tag{11}$$

Eq. (11) defines a basic sensitivity of the correlation fringe pattern ESPI system. For a wavelength λ=632 nm (He-Ne laser source) the basic sensitivity equals to 316 nm.

2.3. Basic expressions for natural frequencies of vibrating plates

The equation of free motion for small out of plane deformations w of a flat uniform elastic plate of density ρ, in x, y

Cartesian coordinates has the form (Blevins, 2016):

$$\frac{Eh^3}{12(1-v)}\left(\frac{\partial^4 w}{\partial x^4} + 2\frac{\partial^4 w}{\partial x^2 y^2} + \frac{\partial^4 w}{\partial y^4}\right) + \gamma\frac{\partial^2 w}{\partial t^2} = 0 \qquad (12)$$

where: E – modulus of elasticity of plate material, v – Poisson's ratio, h – plate thickness, t – time, γ – mass per unit area of the plate ($\gamma = \rho h$).

Using a separation of variables solution for Eq. (12) allows to obtain the associated formulas of natural frequencies and mode shapes for rectangular and annular plates (Blevins, 2016). Natural frequency f_{ij} is expressed in a form:

$$f_{ij} = \frac{\lambda_{ij}^2}{2\pi a^2}\left[\frac{Eh^3}{12(1-v^2)}\right]^{\frac{1}{2}} \text{ Hz} \qquad (13)$$

where: i – number of half-waves in mode shape along x axis (rectangular plate) or number of nodal diameters (round and annular plate), j – number of half-waves in mode shape along y axis (rectangular plate) or number of nodal circles (round and annular plate), λ_{ij} – dimensionless frequency parameter, a – linear dimension of the plate (length of a rectangular plate or outer radius of round or annular plate).

The mode shapes of rectangular plates are combinations of sinusoidal and hyperbolic functions. The mode shapes of circular plates are Bessel functions.

3. EXPERIMENTAL

3.1. Verification of ESPI interferometer accuracy for static out of plane displacement measurement

A general view of the experimental stand is shown in Fig. 2. A front surface of a rectangular 2 mm thick aluminum plate of dimensions 9x10 cm^2 (width and height, respectively) clamped at its bottom edge was used as S_0 surface (Fig. 3). A surface of 15 mm thick aluminum rectangular plate was used as a reference S_r surface. At the upper edge of the back (opposite to S_0 surface) side of the plate, a retroreflector of Renishaw XL-80 laser measuring system was attached. A laser head and the interferometer of the XL-80 system were placed in front of the retroreflector. Slowly increasing load force was applied at the middle of the upper edge of the plate using a tensioned spring. A laser beam reflected from the retroreflector was used by the XL-80 measuring system to evaluate the displacement of the retroreflector. Slight bending of the plate resulted in a decrease of a distance of S_0 to a laser head of XL-80 system and increase of a distance to S_r surface. In this way a measurement of out of plane displacement of a central point of the retroreflector and the corresponding point of S_0 surface was possible at the same time using XL-80 system and ESPI interferometer, respectively. Due to Eq. (11) out of plane displacements w_{i_ESPI} of the points located at the center of a dark correlation fringe of i-th order can be expressed as:

$$w_{i\_ESPI} = i\frac{\lambda}{2} \qquad (14)$$

ESPI correlation fringes of increasing order i, w_{i_ESPI} measurement results determined using Eq. (14) for λ =632 nm and the corresponding values of XL-80 system point displacement measurement results w_{XL80} for a central point of a retroreflector ("+" mark) for increasing deflection of the plate are shown in Fig. 4.
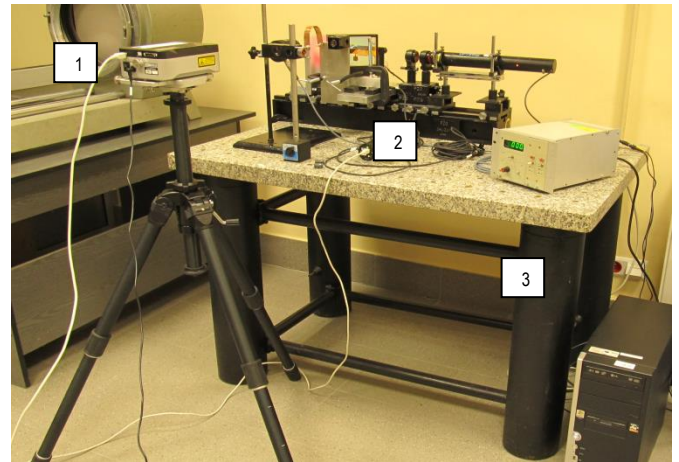

Fig. 2. A general view of the experimental setup: 1 – laser head of XL-80 system, 2 – ESPI interferometer, 3 – anti vibration table
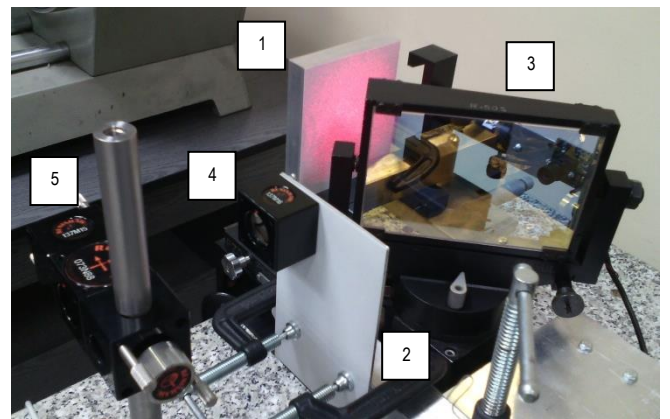

Fig. 3. A setup for verification of ESPI interferometer accuracy: 1 – reference plate, 2 – object plate, 3 – beam splitter, 4 – retroreflector of XL-80 system, 5 – optics of XL-80 system

3.2. Experimental determination of natural frequencies and mode shapes of a vibrating square plate

Resonant frequencies and corresponding mode shapes of the transverse vibrations were experimentally determined for square 9x9 cm^2 aluminum 2 mm thick plate. The plate was clamped at the bottom edge. Vibrations of the plate were excited by a louder driven by an amplifier and a sine wave function generator. The louder was located a short distance from the back side of the plate. When the frequency of vibration was equal to the resonant frequency, stationary and clear correlation fringe patterns were observed. The mode shapes for corresponding resonant frequencies are shown in Fig. 5. Dark correlation fringes represent nodal lines of mode shapes in the pictures.

3.3. Experimental determination of natural frequencies and mode shapes of a vibrating circular slitting saw

Resonant frequencies and corresponding mode shapes of the transverse vibrations of a circular slitting saw (NFTe 100x1.2/64-II) were determined using a method described in Section 3.2. A slitting saw of 100 mm diameter and 1.2 mm thickness was used in the experiment (Fig. 6). The tool was clamped at the sides of a socket (30 mm diameter). The mode shapes for corresponding resonant frequencies are shown in Fig. 7.
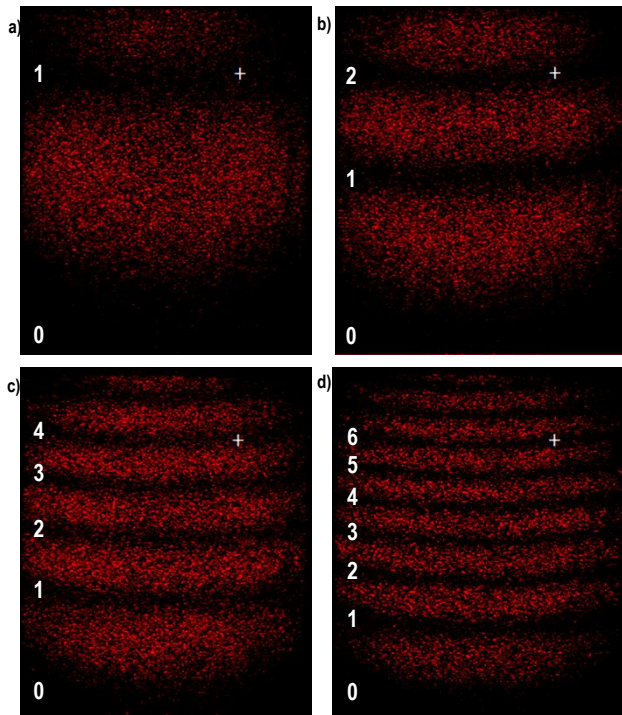
Piotr Mrozek, Ewa Mrozek, Andrzej Werner
Electronic Speckle Pattern Interferometry for Vibrational Analysis of Cutting Tools

DOI 10.2478/ama-2018-0021

Fig. 4. ESPI correlation fringes for out of plane static displacements w of a rectangular Al plate; the numbers at the left side of the picture represent the order i of dark ESPI correlation fringes; "+" mark represents the position of a center of XL-80 system retroreflector used to measure w_{XL-80} point displacement; ESPI and corresponding XL-80 measurement results: a) w_{1_ESPI}=0.316 μm, w_{XL80}=0.313 μm, b) w_{2_ESPI}=0.632 μm, w_{XL80}=0.627 μm, c) w_{4_ESPI}=1.266 μm, w_{XL80}=1.266 μm, d) w_{6_ESPI}=1.896 μm, w_{XL80}=1.945 μm
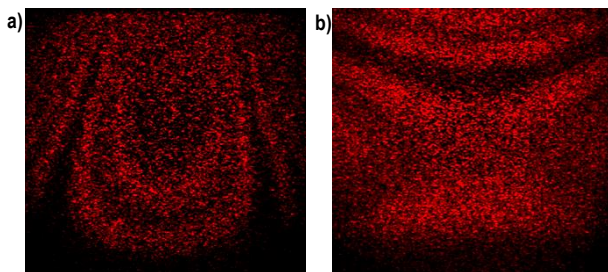
Fig. 5. Mode shapes of vibrations of a square Al plate at resonant frequencies: a) f=532 Hz, b) f=390 Hz

4. RESULTS AND DISCUSSION

Linear measurement accuracy of XL-80 laser system is ±0.5 ppm due to a stabilised laser source and accurate environmental compensation (Brochure: XL-80 laser measurement system). In the experiment the distance between the retroreflector and the interferometer optics was 0.1 m, therefore the static displacement of S_0 surface was measured with about 50 nm accuracy, which was higher than the basic sensitivity of the ESPI system described by Eq. (11). For the correlation fringes shown in Fig. 4. the dark fringes can be easily distinguished from the bright ones, therefore it seems that the accuracy of about $\lambda/4$ (158 nm for He-Ne laser source) may be assumed for ESPI measurements in this case. The results of ESPI measurements show good agreement with XL-80 assessment results, which may serve as the calibration data for the speckle interferometer.
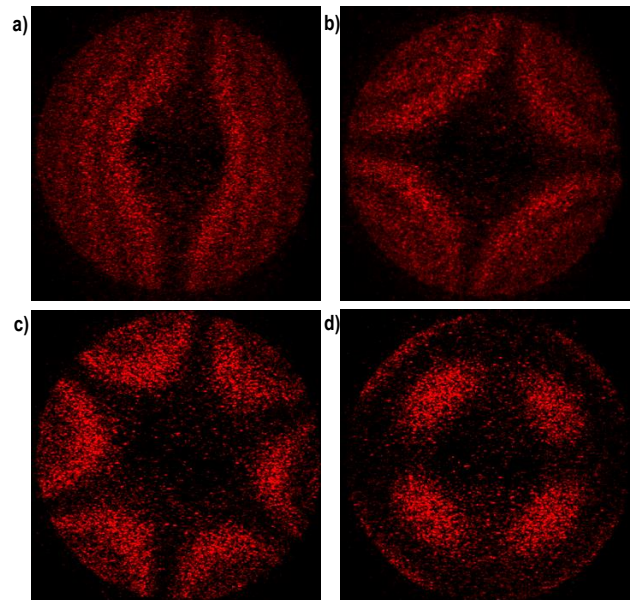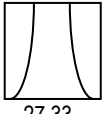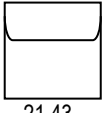

Fig. 6. NFTe 100x1.2/64-II circular slitting saw

Fig. 7. Mode shapes of resonant vibrations of a circular slitting saw at different frequencies: a) f=607 Hz, b) f=840 Hz, c) f=1495 Hz, d) f=5190 Hz

Resonant frequencies f_{ij} of the vibrating aluminum (AW 1050A alloy) square plate were calculated using Eq. (13) for the values of plate material parameters: E=70 GPa, ρ=2700 kg/m³, ν=0.3, a=0.09 m, h=0.002 m. The values of square of dimensionless frequency parameter λ_{ij}^2 for particular vibrating modes (Blevins, 2013) are shown in Tab. 1 and the results of calculations are compared with the experimental data. The values of relative error Δf_{ij} are in a range of a few percent, therefore calculated and measured basic resonant frequencies are in good agreement.
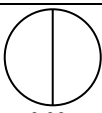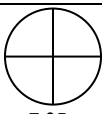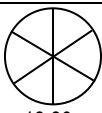
Resonant frequencies f_{ij} of the vibrating circular slitting saw were calculated using Eq. (13) for the values of parameters (SW7M - HS6-5-2 high-speed tool steel): E=210 GPa, ρ=7800 kg/m³, ν=0.3, a=0.010 m, a/b=0.3 (a and b are outer and inner diameters of the tool, respectively), h=0.0012 m. The values of

square of dimensionless frequency parameter $\lambda_{ij}{}^2$ for particular vibrating modes (Blevins, 2013) are shown in Tab. 2 and the results of calculations are compared with the experimental data.

Tab. 1. Analytically and experimentally determined resonant frequencies of a square Al plate (*x,y* - vertical and horizontal direction, respectively)

$\lambda_{ij}{}^2$ for a vibrational mode	Number (*i, j*) of half-waves in *x* and *y* direction	Resonant frequency f_{ij_a} (analytical) [Hz]	Resonant frequency f_{ij_e} (experimental) [Hz]	Relative error Δf_{ij} [%]
27.33	$i = 1$ $j = 3$	523	532	1.7
21.43	$i = 2$ $j = 1$	410	390	5.1

Tab. 2. Analytically and experimentally determined resonant frequencies of a circular saw

$\lambda_{ij}{}^2$ for a vibrational mode	Number (*i, j*) of nodal diameters and nodal circles	Resonant frequency f_{ij_a} (analytical) [Hz]	Resonant frequency f_{ij_e} (experimental) [Hz]	Relative error Δf_{ij} [%]
6.33	$i = 1$ $j = 0$	745	607	22.7
7.95	$i = 2$ $j = 0$	936	840	11.4
13.30	$i = 3$ $j = 0$	1566	1495	4.7

The values of relative error Δf_{ij} are greater than in the case of the square plate experiment, particularly for lower resonant frequencies. For increasing values of a resonant frequency the experimental and theoretical results are in better agreement. In general, the analytical formula of Eq. (13) for resonant frequencies of a circular plate does not strictly apply to a cutting tool of a complex shape as a circular saw, due to differences in geometry between an analytical and the real object. The thickness of the saw used in the experiment was not uniform – it was decreasing radially from a value of 1.2 mm at the cutting edge to a value of 1.0 mm near a tool socket. A variable thickness is not included in analytical calculations. A more accurate computational method should be applied to precisely calculate the resonant frequency in this case. Resonance of the circular saw will occur when the frequency of excitation of the saw vibrations is equal to

one of the experimentally determined resonant frequencies (Tab. 2). The frequency of excitation can be determined as the product of the rotational speed n and the number z of tool tips. Thus the values of rotational speed n that should be avoided during machining using a circular saw with z=64 tips (Fig. 6) may be easily calculated for resonant frequencies shown in Tab. 2 (n_1=9.5 s^{-1}, n_2=13.1 s^{-1} and n_3=23.4 s^{-1} for f_{10_e}=607 Hz, f_{20_e}=840 Hz and f_{30_e}=1495 Hz, respectively).

5. SUMMARY

Detailed knowledge on a range of undesirable frequencies resulting in high amplitude tool vibrations is an essential factor contributing to avoid the improper machining parameters. This issue is particularly important in a case of machining using tools susceptible to chatter diminishing the quality of a machined surface and generating excessive noise. Based on the research carried out, it appears that ESPI gives the opportunity to precisely determine the resonant frequencies of geometrically complex cutting tools. The experimental procedure allows for determining resonant frequencies with accuracy within a few Hz. The important advantage of ESPI method is its simplicity which enables easy interpretation of the results. The conducted experiments showed the usability of this non-contact measurement method in a field of machining.

REFERENCES

1. **Augulis L., Tamulevicius S., Augulis R., Bonneville J., Goudeau P., Templier C.** (2004), Electronic speckle pattern interferometry for mechanical testing of thin film, *Optics and Lasers in Engineering,* 42, 1–8.
2. **Beeck M.A., Hentschel W.** (2000), Laser metrology - a diagnostic tool in automotive development processes, *Optics and Lasers in Engineering,* 34(2), 101–120.
3. **Blevins R.D.** (2016), *Formulas for Dynamics, Acoustics and Vibration*, John Wiley & Sons, Ltd.
4. **Chi-Hung H., Yu-Chih L., Chien-Ching M.** (2004) Theoretical analysis and experimental measurement for resonant vibration of piezoceramic circular plates, *IEEE Transactions On Ultrasonics, Ferroelectrics, And Frequency Control*, 51(1), 12-24.
5. **Foitzik A.H.**, **Kaese W.**, **Vogt T.**, **Sommerer M.**, **Arkhipov S.** (2003), Static and Dynamic Characterization of MEMS via ESPI, *International Journal Of Computational Engineering Science,* 4(3), 467–470.
6. **Fu G., Moosa A.G.** (2002), An Optical Approach to Structural Displacement Measurement and Its Application, *Journal of Engineering Mechanics*, 128, 511–520.
7. **Halama R., Hornacek L., Pecenka L., Krejsa M., Smach J.** (2016), 3-D ESPI Measurements Applied to Selected Engineering Problems, *Applied Mechanics and Materials*, 827, 65–68.
8. **Hild F., Roux S.** (2006), Digital Image Correlation: from Displacement Measurement to Identification of Elastic Properties – a review, *Strain*, 42, 69–80.
9. **Qin J., Gao Z., Wang X., Yang S.** (2016), Three-Dimensional Continuous Displacement Measurement with Temporal Speckle Pattern Interferometry, *Sensors*, 16(12), 2020.
10. **Richardson M.O.W., Zhang Z.Y., Wisheart M., Tyrer J.R. Petzing J.** (1998), ESPI non-destructive testing of GRP composite materials containing impact damage, *Composites Part A*, 29A, 721–729.
11. **Rothberg S.J., Bell J.R.** (2004), On the application of laser vibrometry to translational and rotational vibration measurements on rotating shafts, *Measurement*, 35, 201–210.

12. **Tatar K., Gren P.** (2008), Measurement of milling tool vibrations during cutting using laser vibrometry, *International Journal of Machine Tools & Manufacture,* 48, 380–387.

13. **Van der Auweraer H., Steinbichler H., Vanlanduit S., Haberstok C., Freymann R., Storer D., Linet V.** (2002), Application of stroboscopic and pulsed-laser electronic speckle pattern interferometry (ESPI) to modal analysis problems, *Measurements Science and Technology,* 13, 451–463.

14. **Yang L., Xie X., Zhu L., Wu S., Wang Y.** (2014), Review of Electronic Speckle Pattern Interferometry (ESPI) for Three Dimensional Displacement Measurement, *Chinese Journal Of Mechanical Engineering*, 27(1), 1–13.

15. **http**://www.dantecdynamics.com, Dantec Dynamics, ESPI-Q100.

16. **http**://www.laserndt.com/technology/shearography.htm, Laser Technology Inc., Laser Shearography Technology.

17. **http**://resources.renishaw.com, Brochure: XL-80 laser measurement system.

NUMERICAL SIMULATION AND EXPERIMENTAL TESTING OF TOPOLOGICALLY OPTIMIZED PLA CERVICAL IMPLANTS MADE BY ADDITIVE MANUFACTURING METHODICS

Jozef ŽIVČÁK[*], Radovan HUDÁK[*], Marek SCHNITZER[*], Tomáš KULA[**]

[*]Faculty of Mechanical Engineering, Department of Biomedical Engineering,
Technical University of Košice, Letná 9, 04200, Košice, Slovakia
[*]Faculty of Mechanical Engineering, Department of Applied Mechanics and Mechanical Engineering,
Technical University of Košice, Letná 9, 04200, Košice, Slovakia

jozef.zivcak@tuke.sk, radovan.hudak@tuke.sk, marek.schnitzer@tuke.sk, tomas.kula@tuke.sk

Abstract: The article focuses on compressive axial loading experimental testing and simulations of topologically optimized design and additively manufactured cervical implants. The proposed platform design is based on anatomical and biomechanical requirements for application in the cervical area. Thanks to new ways of production, such as additive manufacturing, and new software possibilities in the field of structural analysis, which use the finite element method and analysis, it is possible to execute topological optimization of an implant in construction solution, which would be impossible to make by conventional methods. The contribution of this work lies in investigation of 3D printed PLA cervical implant usage in surgical intervention and creation of a numerical static loading modelling methodics and subsequent experimental confirmation of the modelling correctness.

Keywords: Topological Optimization, Cervical Implant, Additive Manufacturing, FEA, Numerical Simulation, PLA

1. INTRODUCTION

The proposed platform design of the cervical implant is based on the anatomical and biomechanical parameters of the cervical spine which are currently being used in surgical procedure spinal fusion, aiming to replace the damaged intervertebral disc or for fusion of the individual segments of the vertebra. The spinal inter-body fusion cage could be solid, porous, hollow implant, either cylindrical or nearly cuboid in shape and it can. It can replace the degenerative disc and distract the intervertebral body, thus restoring physiological disc height. The bone grafts can be inserted into the hollow and porous cage allowing the growth of bone through the cage, resulting inner body fusion. Furthermore, it can increase the mechanical strength and fusion rate (Kani and Chew, 2018; Mende et al., 2018). These implants are currently created with conventional manufacturing technologies, e.g. milling, in cases of metal implants or by plastic injection (Yin et al., 2017; Zivcak and Hudak, 2001). These implants are usually created as monoliths without the possibility to manufacture internal structures which creates the opportunity for topological optimization based on numerical analysis and subsequent implementation for production with the use of additive manufacturing technology which makes the manufacturing of internal structures possible.

Within the scope of the topologically optimized design Zhong et al. (2006) investigated topological optimization of lumbar intervertebral cages, this study attempts to prevent the stress shielding effect (the implants is substantially more dense than its surroundings for its application) which is in spinal fusion displayed as the subsidence of the implant based on experimentally calculated parameters in the cervical spine area. Subsidence is a complication whereby the patient's disc height decreases, causing discomfort (Eck et al., 2000; Gzik et al., 2008; Teng et al., 2017).

This paper investigates mechanical properties of topologically optimized design of the intervertebral cage regarding to surgical intervention usage and in addition, the study compares experimentally measured values of additively produced PLA intervertebral cage with numerically calculated values based on material library data.

Aim of the optimization was to find out if optimized design prepared for auotologous bone graft injection withstand compressive axial loading as human vertebra in cervical spine.

The topologically optimized design is built on finite element method (FEM) calculation and finite element analysis (FEA) executed in NX NASTRAN software and experimental tested data executed on tensile testing equipment TIRA TEST2300.

2. MATERIALS AND METHODS

A total of four numerical simulations and one experimental testing of intervertebral cage platform design were constructed and tested in this study.

2.1. Part design and preparation of the finite element model

Intervertebral cage design and construction solution was created to fulfill strict anatomical and biomechanical parameters of the cervical spine based on relevant studies and articles (Gzik et al., 2008; Steffen et al., 2000; Wang, 1996). Parameter of the implant varies from the placement. Our test cage is designed for the intervertebral space C2/C3.

Basic dimensions of test cage: length – 12.5 mm, width – 1.2 mm, height – 7 mm. The model was created in software SIEMENS NX 10. A part of SIEMENS NX 10 software is FEM software NASTRAN with wall thickness analysis feature which is very helpful for topological optimization and comparison of optimized construction solutions, because it shows localities with maximal wall thickness which is relevant optimization criterion.
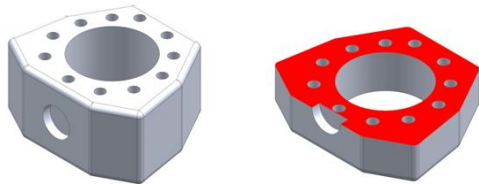
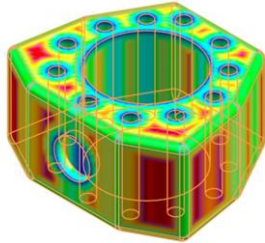**Fig. 1.** Intervertebral cage platform design with cross section

Fig. 2. Wall thickness analysis

Wall thickness analysis shows red colored area (Fig.2) which represents the largest thickness of the wall respectively area with the largest volume of the material (Ivanco et al., 1994). For the accurate results of FEM simulation the input data must correspond with the real environment. In this study PLA – poly-lactid-acid was chosen as a construction material, because nowadays it is trend to use biodegradable materials in surgical interventions (Chen et al., 2013; Kandziora et al., 2001). Mechanical properties are shown in Tab. 1.

Tab. 1. Mechanical properties of PLA vs. Cortical bone (Gillet, 2008; Pintar et al., 1998; NX NASTRAN, 2017)

Propert. Mat.	E [GPa] Young's Modulus	μ [-] Poisson's Ratio	R_e [MPa] Yield Strength	R_m [MPa] Ultimate Tensile Strength
PLA	5.6	0.36	varies	varies
Cortical bone	12	0.6	125 longitud.	130 longitud.

2.2. Numerical simulation base and algorithm

In this case study testing in linear and also in nonlinear area is needed.

For linear area (LFEA) is important a system solution of linear algebraic equations:

$$K(D) = R \qquad (1)$$

For nonlinear (NFEA) area is important a system solution of nonlinear algebraic equations:

$$K(D)D = R(D) \qquad (2)$$

where: K – is the stiffness matrix, D – is a vector containing displacements in nodes, R – is a vector containing external forces (Bocko and Segľa, 2016; Matishen, 2012; Seweryn and Molski, 1996). For numerical study of implant behavior under the influence of load was also used NASTRAN software. Algorithm of the simulation has four steps: 1. CAD model creation, 2. FE model creation, 3. Boundary conditions definition, 4. Numerical and graphical results analysis (Fig.3).
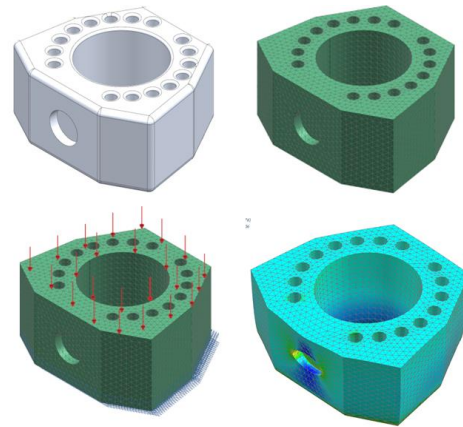

Fig. 3. Numerical simulation algorithm: 1. CAD model creation (left up); 2. FE model creation (right up); 3. Boundary conditions definition (left down); 4. Numerical and graphical results analysis (right down)

2.3. Numerical simulation 1 methodics

Intervertebral cage construction solution was original solid platform design. Material parameters were imported from NX NASTRAN material library. Initial input parameters for FEM processing were defined as compressive axial stress (static load) which is produced by weight of the head, muscles and surrounding tissue. Initial FE model is composed from these parameters: element type → CTETRA 10 nodes, element size → 0.5 mm, number of elements → 43392, restraint → displacement in direction 1, 2 and 3 (x, y, z) prevented, free rotation, load → 50N, number of time steps →100, max time increase → 0.001 sec.

Next step was to simulate vertebra like mechanical properties. In systematic study effect of age and loading rate on human cervical spine injury threshold, Pintar et al. (1998) found out compressive axial load which causes serious vertebra injury varies from 2 kN – 7 kN. Based on this information load parameter was changed to 7 kN to simulate vertebra fracture load.

2.4. Numerical simulation 2 methodics

Intervertebral cage construction solution was topologically optimized based on wall thickness analysis data and data from numerical simulation 1. Construction solution was designed for additive manufacturing technology. Aim of the optimization is material reduction, stiffness reduction due to prevent subsidence effect (Teng et al., 2017; Yin et., 2017; Zhong yet al., 2006). The inner space of the implant is formed by 16 cavities which are interconnected with initial technological apertures. The purpose of these apertures is in having access to each cavity, to be sure there is no presence of extra powder after production process. Optimized construction solution is designed to withstand load of cervical vertebra. It means 7kN was set as load force. Other input data for numerical simulation were identical as for modified simulation in chapter 2.3.
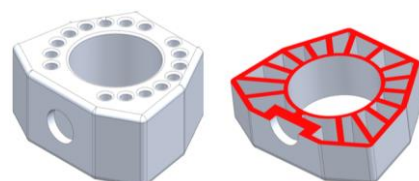

Fig. 4. Topological optimization side view (left), cross section (right)

2.5. Experimental testing and numerical simulation based on experimental tested data

For numerical simulation results confirmation experimental testing was done. There were 20 prototypes produced by fused filament fabrication technology (FFF) printed from E-sun bioplastic PLA material each of which underwent compressive axial testing by electromechanical testing device TIRA TEST2300 that ended with the destruction of the sample.

The purpose of this testing was to gain the true material properties of the alloy in our case of topologically optimized intervertebral cage. Subsequently, these values were used to create numerical computations that simulated the process of the generated tension fields in the implant as a result of a load factor. Through inner sensor of device TIRA TEST2300 were obtained datasets with over a thousand values corresponding to load force F [kN], induced stress σ [MPa], displacement P1/P2[mm] and to resulted strains ε [-] in every loading step for each cage prototype (Fig. 5).

1-F [kN]	1 σ [Mpa]	P1-P2[mm]	1 ε [-]	2-F [kN]	2 σ [Mpa]	P1-P2[mm]	2 ε [-]
0.030	0.316	0.090	0.014	0.020	0.211	0.050	0.007
0.030	0.316	0.100	0.015	0.000	0.000	0.060	0.009
0.030	0.316	0.100	0.015	0.020	0.211	0.060	0.009
0.030	0.316	0.100	0.015	0.010	0.105	0.060	0.009
0.030	0.316	0.110	0.017	0.010	0.105	0.070	0.010
0.040	0.422	0.120	0.018	0.010	0.105	0.080	0.012
0.050	0.527	0.120	0.018	0.010	0.105	0.080	0.012
0.050	0.527	0.120	0.018	0.020	0.211	0.080	0.012
0.060	0.633	0.130	0.020	0.020	0.211	0.090	0.013
0.080	0.844	0.140	0.021	0.020	0.211	0.100	0.015
0.090	0.949	0.140	0.021	0.040	0.422	0.100	0.015
0.100	1.055	0.140	0.021	0.040	0.422	0.100	0.015
0.120	1.266	0.150	0.023	0.040	0.422	0.110	0.016
0.140	1.477	0.150	0.023	0.050	0.527	0.120	0.018
…	…	…	…	…	…	…	…
5.990	63.186	3.130	0.472	5.240	55.274	3.080	0.460
5.990	63.186	3.140	0.474	5.240	55.274	3.080	0.460
6.010	63.397	3.140	0.474	5.260	55.485	3.090	0.461
6.030	63.608	3.150	0.475	5.260	55.485	3.090	0.461
6.040	63.713	3.160	0.477	5.270	55.591	3.100	0.463
6.050	63.819	3.160	0.477	5.280	55.696	3.100	0.463
6.060	63.924	3.160	0.477	5.290	55.802	3.110	0.464

Fig. 5. Measured values corresponding to load force, induced stress, displacement and to resulted strains in every loading step – start and end measurement of prototypes 1,2

After detailed analysis of measured data (Fig. 6) area between $R_{p0.2}$ value to R_e value was screened.
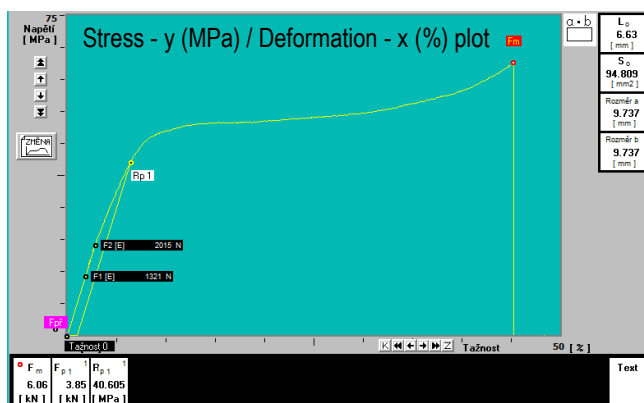

Fig. 6. Pressure testing processing curve – TIRA TEST 2300 (one of 20 intervertebral cage test samples) – screened area between $R_{p0.2}$ to R_eH. Maximal values: Stress 75 MPa (step 10MPa), Deformation 50% (step 5%)
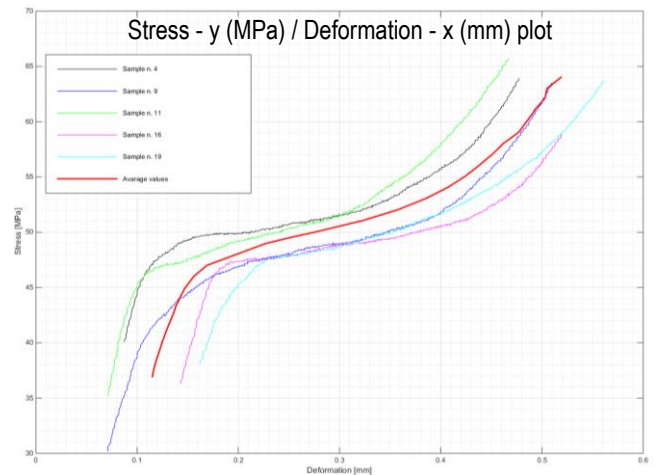

Fig. 7. Curves of experimental testing behaviour – NX NASTRAN (5 samples of 20 with average values), Maximum values: Stress 70 MPa (step 10MPa), Deformation 0.6mm (step 0.1mm)

The reason why this area was object of study was to examine the behavior of the material made by additive manufacturing technology under biomechanical loads in the cervical spine area, because of anisotropic properties assumption of the material. Input values for simulation based on experimental tested data (Fig.7) of all 20 prototypes were calculated using mathematical and statistical methods.

3. RESULTS AND DISCUSSION

This paper investigated numerical and experimental testing of topologically optimized PLA cervical implants and methodics creation of numerical simulation based on FEA. Aim of the optimization was to find out if optimized design prepared for auotologous bone graft injection withstand compressive axial loading as human vertebra in cervical spine (Pintar et al., 1998; Seweryn and Molski, 1996; Sidun and Dąbrowski, 2009). Results of initial simulation (Fig. 8) for deformations and displacement were: displacement δ = 2.058 $\times 10^{-3}$mm and maximal equivalent von Mises stress σ_{max} = 0.8 MPa.
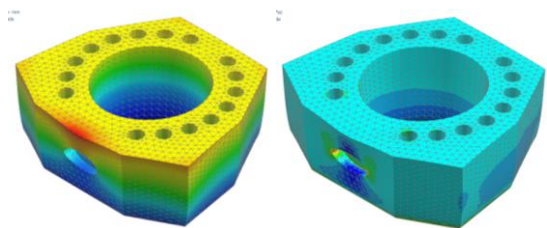

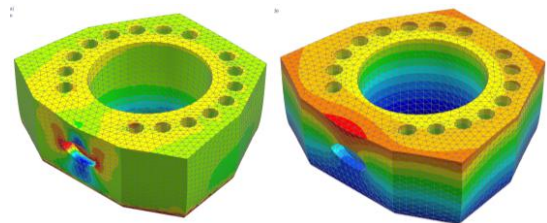**Fig. 8.** Results of initial simulation – deformation (left), induced stress field (right)

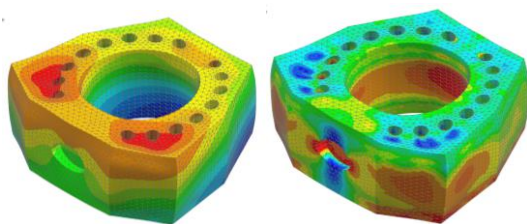**Fig. 9.** Results of modified simulation – deformation (left), induced stress field (right)

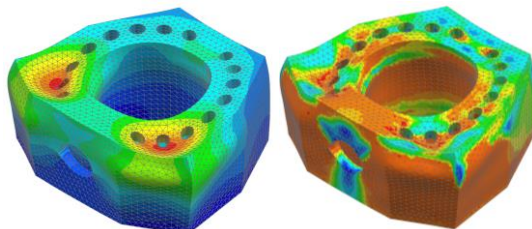**Fig. 10.** The resulting deformation (left), induced stress field (right)

Fig. 11. The resulting deformation (left), induced stress field (right) – real yield strength for simulation based on experimental data

Results of modified simulation (Fig.9) with 7 kN load were: displacement δ = 0.134 mm and maximal equivalent von Mises stress σ_{max} = 87 MPa.

From results it is seen conventional solid design can withstand load of the segments above the neck and it is suitable for seniors and for passive people regarding compressive axial loading.

Results of optimized cage simulation with 7 kN loading (Fig.10) were: displacement δ = 0,348 mm and maximal reduced stress Von Mises σ_{max} = 82.34 MPa.

Results of the numerical simulation showed topologically optimized design cannot withstand full compressive axial load of human vertebra on its own. For numerical simulation results confirmation experimental testing was done. Subsequently, values from testing were used to create numerical computations that simulated the process of the generated tension fields in the implant as a result of a load factor.

Results of simulation based on experimental testing (Fig.11) were: displacement δ = 0.388 mm and maximal reduced stress Von Mises σ_{max} = 87.29 MPa.

After detailed analysis of measured data area between $R_{p0.2}$ value to R_e value was screened. The reason why is this area object of study is to examine the behavior of the material made by additive manufacturing technology under higher loads, because of anisotropic properties assumption of the material. Based on analysis, mathematical, statistical methods and data processing it was concluded that the true average yield strength of the material is R_e = 63.6 MPa, while the yield strength listed in the software material library is R_e = 62.7 MPa. It can be concluded that with right setting of input material values and properly set numerical values compressive axial simulation can be a tool for implant design verification.

PLA material on its own cannot withstand the same compressive axial loading as autologous human vertebra. Potential of this material is to fulfill the role as a scaffold in combination with autologous bone graft and its following whole biodegradation

REFERENCES

1. **Bocko J., Segľa Š.** (2016), *Numerical methods of rigid and pliable bodies*, 1st Edition, Technical University of Košice.

2. **Chen Y., Wang X., Lu X., Yang L., Yang H., Yuan W., other authors** (2013), Comparison of titanium and polyetheretherketone (PEEK) cages in the surgical treatment of multilevel cervical spondylotic myelopathy: a prospective, randomized, control study with over 7-year follow-up, *European Spine Journal.* 22(7), 1539–1546.

3. **Eck K.R., Bridwell K.H., Ungacta F.F. Ungacta, Lapp M.A., Lenke L.G., Riew.** (2000), Analysis of titanium mesh cages in adults with minimum two-year follow-up, Spine, 25(18), 2407–2415.

4. **Gillet P.**, **Cessotto S.,** (2008), *Mechanics of bones*, Montefiore Institute lecture available online: http://www.montefiore.ulg.ac.be/systems/GBIO/gbio001/chap_2.3.pdf

5. **Gzik M., Wolański W., Tejszerska D.** (2008), Experimental determination of cervical spine mechanical properties, *Acta of Bioengineering and Biomechanics*, 10(4), 49–54.

6. **Ivančo V., Kubín K., Kostolný K.** (1994), *Finite Element Method*, 1st Edition, Elfa, Košice

7. **Kandziora F., Pflugmacher R., Schäfer J., Born C., Duda G., Haas N.P.** (2001), Biomechanical comparison of cervical spine interbody fusion cages, *Spine*, 26(17), 1850–1857.

8. **Kani K.K., Chew FS.** (2018), Anterior cervical discectomy and fusion: review and update for radiologists, *Skeletal Radiology*, 47(1), 7–17

9. **Mathisen K.M.** (2012), *Solution methods for nonlinear finite element analysis (NFEA)*, Norwegian University of Science and Technology Lecture 11: Geilo Winter School – January, available online: https://www.sintef.no/globalassets/project/evitameeting/2012/kmm-geilo-2012-lecture-11a.pdf

10. **Mende K., Eicker S., Weber F.** (2018), Cage deviation in the subaxial cervical spine in relation to implant position in the sagittal plane, *Neurosurgical Review*, 41(1), 267–274.

11. **NX NASTRAN** (2017), Material library.

12. **Pintar F.A, Yoganandan N, Voo L.** (1998), Effect of age and loading rate on human cervical spine injury threshold, *Spine*, 23(18), 2407–2415

13. **Seweryn A, Molski K.** (1996), Elastic stress singularities and corresponding generalized stress intensity factors for angular corners under various boundary conditions, *Engineering Fracture Mechanics*, 55(4), 529–556,

14. **Sidun J., Dabrowski J.** (2009), Bone Ingrowth Processes on Porous Metalic Implants, *Solid State Phenomena,* 147-149, 776–781.

15. **Steffen T., Tsantrizos A., Fruth I., Aebi M.** (2000), Cages: designs and concepts, *European Spine Journal*, 9(1), 89–94.

16. **Teng L., Chao L., Baohui Y., Jiantao L., Feng Z., Dong W., Haopeng L., Xijing H.** *(*2017), Single-Level Anterior Cervical Corpectomy and Fusion Using a New 3D-Printed Anatomy-Adaptive Titanium Mesh Cage for Treatment of Cervical Spondylotic Myelopathy and Ossification of the Posterior Longitudinal Ligament: A Retrospective Case Series Study, *Medical Science Monitor*, 23:3105-3114.

17. **Wang K.** (1996), The use of titanium for medical applications in the USA, *Material Science Engineering*, 213, 134–137.

18. **Yin X., Jiang L., Yang J., other authors** (2017), Application of biodegradable 3D-printed cage for cervical diseases via anterior cervical discectomy and fusion (ACDF): an in vitro biomechanical study, *Biotechnology Letters*, Springer, 39(9), 1433–1439

19. **Zhong Z.CH., other authors** (2006), Finite element analysis of the lumbar spine with a new cage using a topology optimization method, *Medical Engineering & Physics*, 28(1), 90–98.

20. **Živčák J., Hudák R.** (2001), *Biomechanisms*, ManaCon, Prešov.

INVESTIGATION OF FRACTURE PROCESS OF S355JR STEEL IN TRANSITION REGION
USING METALLOGRAPHIC AND FRACTOGRAPHIC TESTS AND NUMERICAL ANALYSIS

Ihor DZIOBA[*], Sebastian LIPIEC[*], Piotr FURMANCZYK[**], Robert PALA[*]

[*]Faculty of Mechatronics and Mechanical Engineering, Department of Machine Design,
Kielce University of Technology, Al. 1000-lecia PP 7, 25-314 Kielce, Poland
[**]Faculty of Mechatronics and Mechanical Engineering, Department of Metal Science and Manufacturing Processes,
Kielce University of Technology, Al. 1000-lecia PP 7, 25-314 Kielce, Poland

pkmid@tu.kielce.pl, slipiec@tu.kielce.pl, pfurmanczyk@tu.kielce.pl, rpala@tu.kielce.pl

Abstract: In the paper are presented test results of fracture process in brittle-to-ductile transition range for two microstructural types of S355JR steel – ferrite-pearlite and ferrite-carbides. For both kinds of S355JR steel obtained in temperature range of transition region the strength and plastic properties are similar, but the fracture toughness characteristics showed significantly are various. To clarify the differences in the course of trends in the mechanical characteristics performed metallographic and fractographic observations using the scanning electronic microscope. The fractographic examination showed that changes in the fracture surface morphology were dependent on the test temperature. It was also found that during the subcritical crack growth the region of ductile fracture extension reduced with decreasing temperature. The results of finite element method (FEM) calculation the stress fields in front of the crack of single edge notch in bending (SENB) specimens in the range of brittle-to-ductile transition are presented also. The FEM calculations were performed on the numerical model of SENB specimen using the ABAQUS program.

Keywords: S355JR steel, Mechanical Properties, Microstructure, Fractographic Examination, Numerical Analysis, Stress Distributions

1. INTRODUCTION

The S355JR (18G2A) steel is a material widely used for different types of structural elements and systems. Its manufacturing process usually involves normalizing, which leads to the formation of a layered ferrite-pearlite (FP) or ferrite-pearlite-bainite microstructure (Dobrzański, 1999; Dzioba and Skrzypczyk, 2006; PN-EN 10025-2, 2007). When the steel is welded, its microstructure in the heat affected zone changes as a result of the formation of bainite or ferrite-bainite microstructures. Annealing or long-term exposure to elevated temperatures results in the spheroidization and coagulation of carbides, and, consequently, the formation of a microstructure ferrite with coarse carbide particles (FC) in the ferrite or/and bainite regions as well as at the grain boundaries (Boumerzoug et al., 2010; Dymski et al., 2005). Changes to the microstructure, which are responsible for the changes in the strength and fracture toughness of the material, have a direct effect on the structure integrity. When the strength and reliability of a structure are assessed, it is important that the real characteristics of the material be taken into account (ASTM E1820-09, 2011; Chen and Cao, 2015; Dzioba and Neimtiz, 2007; FITNET, 2008). This analysis cannot base on the data contained in the material certificate.

Testing carried out under low temperature conditions is essential to assess the integrity of structures containing welded elements, especially when this temperature is from the range of ductile-to-brittle transition region and lower (Dymski et al., 2005). Assessment of structural integrity requires focusing on welded elements, because the mechanical properties of a material in the fusion and heat affected zones are much different from those of base metal (Dymski et al., 2005; Dzioba and Skrzypczyk, 2006).

Fractographic and metallographic investigations provide information on the mechanisms by which fracture occurs in steels and metallic alloys (Kocanda, 1978). The analysis of microstructure and fracture surfaces is necessary to identify the crack propagation behaviour and the internal factors affecting the failure process, such as dimension of the grains and types and size of inclusions or carbides.

According to the most important fracture criteria in order to realize the fracture process it is necessary to exceed the critical level of stress (or strain) on critical length (McClintok, 1968; Beremin, 1983; Rotchie et al., 1973; Seweryn, 1993; Seweryn and Mróz, 1995; Neimitz et al., 2007, 2010). So, the knowledge on local stress and/or strain distributions in the crack front is required. The components of stress and strain should be calculated using a numerical method.

2. TEST METHODS, STRENGTH AND FRACTURE TOUGHNESS PROPERTIES, FRACTOGRAPHY OBSERVATION

The two types of microstructure of S355JR steel were analyzed in present testing: ferrite-pearlite and ferrite with coagulated carbides. The FP microstructure (Fig. 1a) in the specimens was obtained as a result of normalization through annealing at 950°C per 20 minutes and cooling in the air. In the second heat treatment additionally to normalization carried out the annealing at 150 hours with cooling in oil, what leads to FC microstructure (Fig. 1b).

The tests were conducted using a UTS/Zwick (100 kN) testing machine with an electrodynamic drive and an automated control and data acquisition system. The strength properties of S355JR steel were determined through uniaxial tensile testing. Standard specimens of 5 mm in diameter were used for that purpose (PN-EN ISO 6892-1, 2010).

Because of the high plasticity of S355JR steel fracture toughness was determined as the critical value of J-integral, J_{IC}, using single-edge notched specimens in three-point bending, SENB. The potential drop method or change compliance method were used to determine the critical values of fracture toughness for each single specimen tested. The specimens were prepared and tested in accordance with the ASTM standard (ASTM E1820-09, 2011).

The low-temperature tests were performed in the temperature range from -130°C to +20°C in a thermal chamber using liquid nitrogen as a coolant. A thermocouple was mounted directly on a specimen tested. During the measurements, the temperature changes did not exceed ±1°C; the measurement accuracy was 0.1°C.
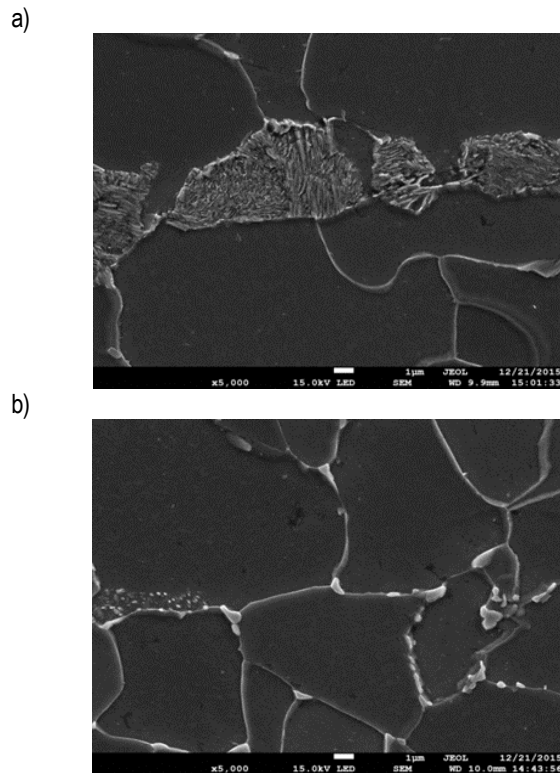
a)

b)

Fig. 1. The FP (a) and FC (b) microstructure types of S355JR steel

The true $\sigma - \varepsilon$ dependences were obtained in the range of testing temperature from data of tensile uniaxial test. The average data of strength characteristics of FP and FC microstructure of S355JR steel are presented in Tab. 1. Generally, the strength characteristics of FP material are some higher than of FC. For both kinds of S355JR steel microstructure, FP and FC, temperature lowering leads to increase in strength characteristics. Only the material hardening factor, n, slowly decreases with temperature reduction.

The process of sub-crack propagation in plasticity steel is realized in some stages. The initially sharp tip of pre-crack becomes blunted as a loading result. In certain moment the sub-crack

starts. Fracture toughness according to this moment is denoted as J_i. The method for determining fracture toughness value in crack initiation moment was proposed in Japanese and ESIS (ESIS P2-92, 1992; JSME S 001-81, 1981) standards and in the paper by Zu-Han and Chang-Xiang (1985). According to these standards, J_i is proportional to stretch zone width (SZW), $\Delta\overline{a}_{SZW}$: $J_i = \lambda \cdot \Delta\overline{a}_{SZW}$, which should measured using microscope. Factor λ in various standards was differently defined. According to Shih (1981) proposal, J_i is calculated from the equation:

$$J_i = \frac{2\sigma_Y}{d_n}\Delta\overline{a}_{SZW} \tag{1}$$

where: $\sigma_Y = 0.5(\sigma_{YS} + \sigma_{UTS})$.

Tab.1. Mechanical properties of FP and FC microstructures of S355JR steel at test temperature range

Materials	Characteristics	+20°C	-50°C	-80°C	-100°C (FC)/ -120°C (FP)
FP	E [GPa]	202	210	212	214
	σ_{LYS} [MPa]	378	414	414	473
	σ_{UYS} [MPa]	380	428	456	522
	σ_{UTS} [MPa]	613	670	673	686
	n	4.69	4.28	4.04	3.89
FC	E [GPa]	211	216	218	220
	σ_{LYS} [MPa]	380	378	420	448
	σ_{UYS} [MPa]	392	379	458	486
	σ_{UTS} [MPa]	588	626	626	681
	n	4.92	4.37	4.15	4.01

where: σ_{LYS} – lower yield stress; σ_{UYS} – upper yield stress; σ_{UTS} – ultimate tensile strength.
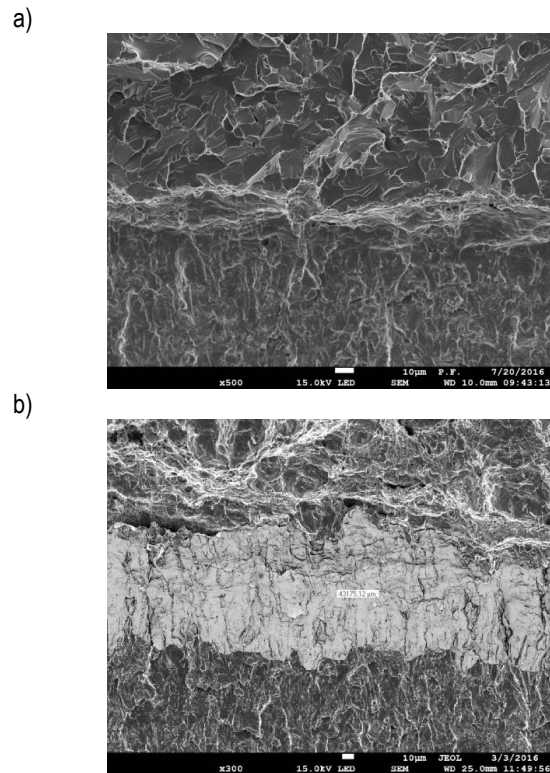
a)

b)

Fig. 2. The fracture surface of FC material for: (a) -80°C; (b) 20°C with stretch zone area measured

Coefficient d_n is a function dependency of power hardening factor n, and stress state in crack front. According to Guo (1995) proposal d_n is function of n and stress state factor T_Z:

$$T_Z = \frac{\sigma_{33}}{\sigma_{11} + \sigma_{22}} \qquad (2)$$

In the current investigation the SZW were measured on fracture surfaces of SENB tested specimens using the scannig electronnic microscope (SEM) (Fig. 2a). The stretch zone area was measured (Fig. 2b). The average value of SZW was obtained by dividing area per length.

According to the ASTM standard (ASTM E1820-09, 2011) the fracture toughness critical value for sub-crack ductile propagation is determined for its extension equal to 0.2 mm. So, it can be observed that there is some difference between fracture toughness measured at the initiation moment and for crack extension 0.2 mm. This difference is significant for high plasticity material.

In Fig. 3 are shown curves, which present dependences of fracture toughness critical values on test temperature range. Three zones are present in each curve. The lower plateau, where crack extension is only by brittle cleavage fracture. The higher plateau, where crack growth is according to the ductile fracture mechanism. And the transition region, where growth cracks starts by ductile mechanism and mechanism of growth changes into brittle.
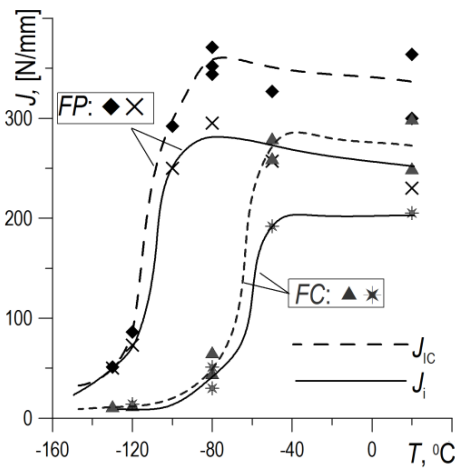

Fig. 3. The relations of fracture toughness critical values on temperature

The fracture toughness of FP material is higher than FC material. In the figure are presented data of fracture toughness J_{IC} (dotted lines) and J_i (solid lines) received at the crack initiation. The similar level of fracture toughness of J_{IC} and J_i are obtained only for full brittle fracture on the lower plateau. In the transition region and in the higher plateau, where is present ductile fracture, the value of J_{IC} is higher. These differences increase together with temperature.

3. NUMERICAL MODELING AND CALCULATION

The FEM calculations were performed on the numerical model of SENB specimen ($W = 24$ mm, $S = 96$ mm, $B = 12$ mm) by using the ABAQUS program (Abaqus 6.12). In the first stage the true stress-strain relation was determined for the elastic-plastic range. Nominal stress-strain data relation was used only to the max stress value, σ_{UTS}. Using this data were calculated true

stress and strain according to the well-known formulas (Boumerzoug et al., 2010; Chen et al., 2015):

$$\epsilon_t = \ln(1 + \epsilon_{nom}) \qquad (3)$$

$$\sigma_t = \sigma_{nom}(1 + \epsilon_{nom}) \qquad (4)$$

where: ϵ_t – true strain, σ_t – true stress, ε_{nom} – nominal strain, σ_{nom} – nominal stress.

From the linear part of the stress-strain relation was determined the Young modulus. The non-linear part of the stress-strain relation was interpolated in the direction of the increased stress values by the linear function approximation of 100 – 120 last points from the data set (Neimitz and Galkiewicz, 2010). The true plastic components of strain were obtained by using the formula:

$$\varepsilon_{pl} = \varepsilon_t - \frac{\sigma_t}{E} \qquad (5)$$

The SENB specimen was divided into 12 layers in thickness direction. The 8 nodes three-dimensional elements were used in calculation. Density of the elements mesh increases in the direction to crack tip. The crack tip was modelled as an arc of 0.012 mm in the radius.

The possibility of transference was blocked according to the scheme shown in Fig. 4. The process of load simulation was generated by moving the high pin roller in y axis direction. The roller position was taken from the experimental load-displacement record.
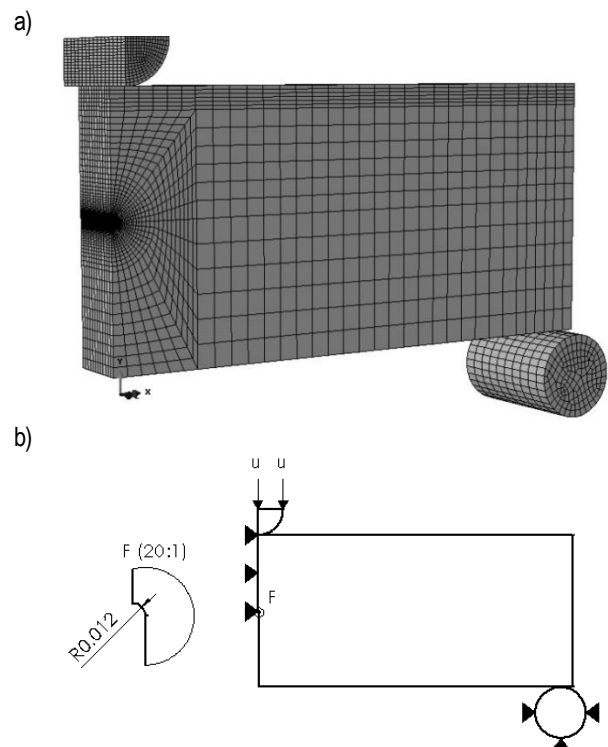
a)

b)

Fig. 4. The three points bend (SENB) specimen model: a) numerical model with mesh, b) boundary conditions scheme

In numerical calculation C3D8R finite elements were used. The three-dimensional problem using 8-nodes elements was solved numerically. Three-point bending specimen model contained 21600 elements. The finite elements size was reduced from furthest areas, to the crack front. In the area immediate at top crack the dimension of elements was equal to about 0.02 mm.

Ihor Dzioba, Sebastian Lipiec, Piotr Furmanczyk, Robert Pala
Investigation of Fracture Process of S355JR Steel in Transition Region using Metallographic, Fractographic Tests and Numerical Analysis

DOI 10.2478/ama-2018-0023

While on the furthest areas the elements dimension was equal to about 1.6 mm (Fig. 8a). Finite element mesh quality in a model was compromised using the Abaqus grid quality option.
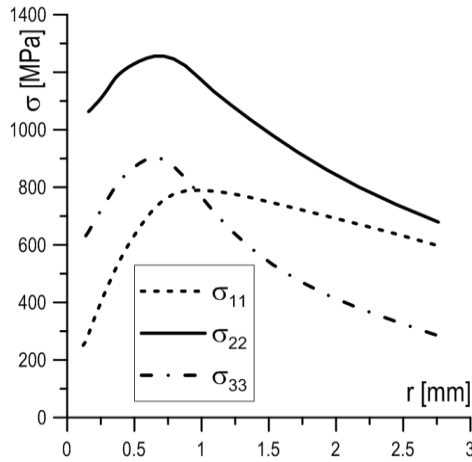

Fig. 5. The distributions of stress components in the axis plane of specimen, FC material, T_{test}= +20°C

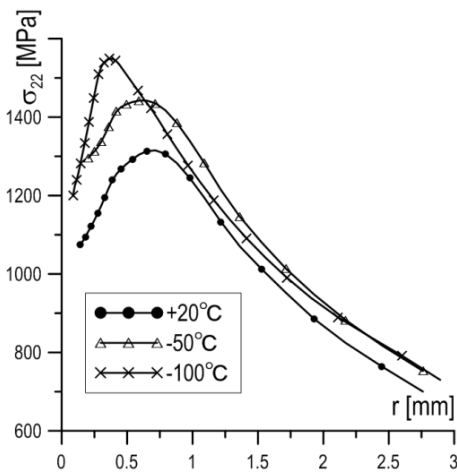**Fig. 6.** The opening stresses distributions σ_{22} in the axis plane of specimen, FP material, T_{test}= +20°C, -50°C and -100°C

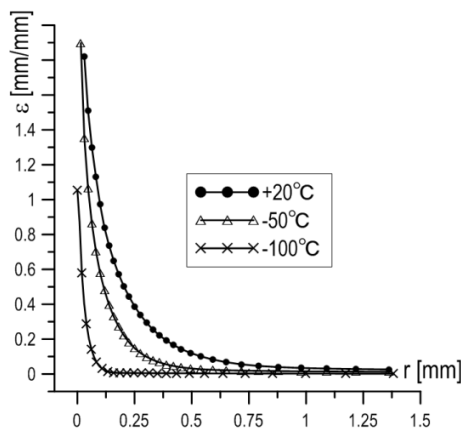**Fig. 7.** The equivalent strain distributions in the axis plane of specimen, FC material, T_{test}= +20°C, -50°C and -100°C

The stress and strain distributions in the crack front were obtained. For example in Fig. 5 presented the components of stress

distribution: σ_{11} – in direction of crack growth; σ_{22} – normal to crack plane; σ_{33} – in direction of specimen thickness. The examples of changes the distributions stress and strain components of temperature influence are shown in Figs 6, 7.

4. RESULTS AND DISCUSION

The stress state factors T_Z and R_{eff} were calculated based on the stress distributions in front of the crack. Stress state factor T_Z was defined above. This quantity is needful for calculation of d_n and secondly J_i. Stress state factor R_{eff} was defined by Rice and Tracey (1969):

$$R_{eff} = \frac{(\sigma_{11} + \sigma_{22} + \sigma_{33})/3}{\sigma_{eff}} \qquad (6)$$

$$\sigma_{eff} = \frac{1}{\sqrt{2}}\sqrt{(\sigma_{11} - \sigma_{22})^2 + (\sigma_{22} - \sigma_{33})^2 + (\sigma_{11} - \sigma_{33})^2} \qquad (7)$$

Stress state factor R_{eff} is used to characterize the material tendency to brittle or ductile fracture. High level of R_{eff} identifies with material tendencies to brittle fracture, while when shown low level of R_{eff} the fracture is realized according to ductile mechanism. The distributions of R_{eff} levels in thickness direction of SENB specimens are shown in Fig. 8. The maximum level of R_{eff} is observed in the middle part of specimen thickness. In the direction to specimen side the level of R_{eff} decreases. The R_{eff} distributions in thickness direction of FP microstructure are presented in Fig. 8a. For the specimens tested at temperature range from 20°C to -80°C, in which sub-critical crack grows according to brittle mechanism, level of R_{eff} is a similar – max values about 2.2 in central plane and 1.6÷1.7 in the side plane of the specimen. Significant increasing of the R_{eff} level takes place if brittle cleavage extension of sub-critical crack occurred, as for specimen tested at -120°C.

The data of R_{eff} distributions with thickness of FC microstructure specimens are shown in Fig. 8b. Full ductile mechanism of sub-critical crack growth in the specimens of FC material was noticed only at 20°C. The R_{eff} distribution for this specimen placed lowermost. At test temperature -50°C sub-critical crack starts by ductile, and after some crack extension takes place change of growth mechanism by cleavage. The R_{eff} distribution for this specimen is located some higher than the previous one. The brittle cleavage mechanism was realized at cracks extension for test temperature lower than -80°C. The dependences for specimens tested at -80°C and -100°C are put close one by one. The maximum level of R_{eff} factor reaches to about 2.5 in the middle part of the specimens and to about 2.0÷2.1 in the side plane of the specimen.

In Fig. 9 are shown the dependences of R_{eff} average values and fracture toughness J_i values with temperature for FP and FC microstructure of S355JR steel. The mean values of the R_{eff} were calculated as the arithmetic mean of the stress state factor values along the specimen thickness, based on the data in Fig. 8. The average values of R_{eff} keep some stable level for ductile sub-crack growth in the zone where J_i belongs to the higher plateau. The R_{eff} level increases with test temperature lowering in the transition region of J_i data, when cleavage cracking is present.

For both types of S355JR steel, the level of strength properties σ_{YS}, σ_{UTS}, E increase, while hardening factor n decreases,

with temperature lowering. The level for all strength characteristics of FP microstructure is some higher compared to FC.
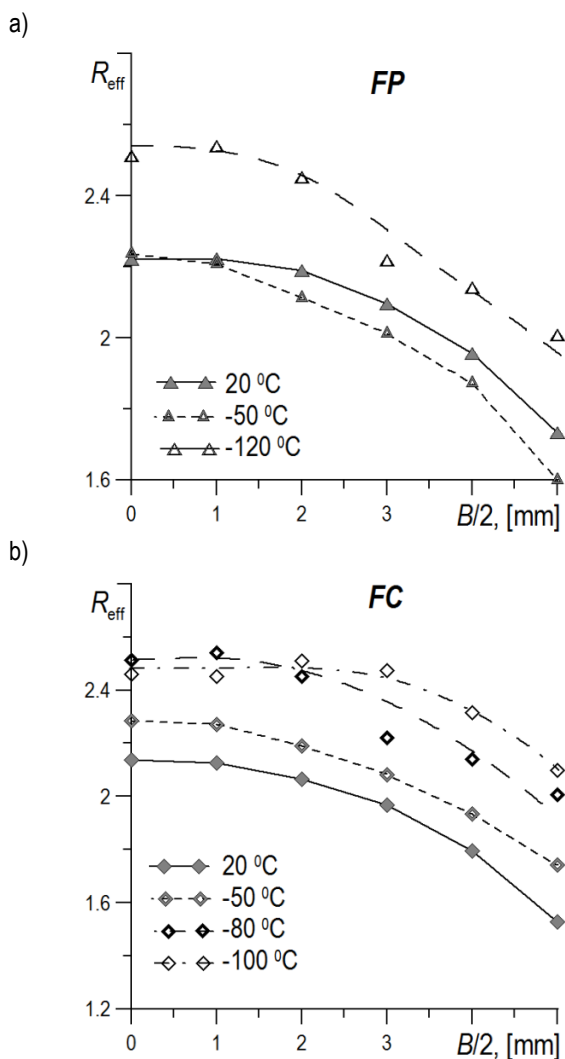
a)

b)

Fig. 8. The R_{eff} distributions in thickness direction of FP (a) and FC (b) material for test temperatures
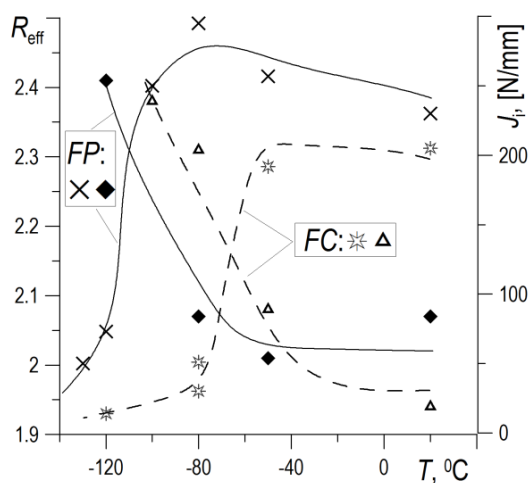

Fig. 9. Relationships between R_{eff} average values, J_i and test temperature

The critical values of fracture toughness of S355JR steel with FP microstructure are higher than of FC in tested temperature interval. The fracture toughness in initiation moment J_i was determined by using results scanning microscope tests of fracture surfaces and numerical calculation of stress components in crack front of the tested specimens. The fracture toughness levels J_i are similar to J_{IC} only for full cleavage mechanism cracking. However, if ductile crack extension is present, J_{IC} is higher than J_i.

FEM calculation of SENB specimens allows to obtain stress and strain distributions in front of the crack. The stress state factors T_Z and R_{eff} in front of the crack were calculated also.

It was shown that fracture mechanism strictly depends on stress state factor R_{eff}. For both types of microstructure, FP and FC, cleavage cracking takes place when the average value of R_{eff} in specimen exceeds the level of 2.1. When the average level of R_{eff} was lower than 2.0 the ductile mechanism of crack extension occurred in the specimens. For specimens in which were observed ductile mechanisms of sub-crack extension, also performed high level of strain in front of the crack (Fig. 7). The high level of strain in front of the crack exactly leads to growth of cavity around particles of carbides and inclusion.

REFERENCES

1. **Abaqus 6.12.** Getting Started with Abaqus, *Interactive Edition*.
2. **Anderson T.L.** (2008), *Fracture Mechanics*, Taylor and Francis Group.
3. **ASTM E1820-09.** (2011*), Standard Test Method for Measurement of Fracture Toughness*. Annual Book of ASTM Standards, 03.01, 1070–1118.
4. **Beremin F.M.** (1983), A local criterion for cleavage fracture of a nuclear pressure vessel steel, *Metallurgical Transaction A*, 14A, 2277–2287.
5. **Boumerzoug Z., Derfouf Ch., Baudin T.** (2010), Effect of welding on microstructure and mechanical properties of an industrial low carbon steel, *Scientific Research Engineering*, 2, 502–506.
6. **Chen J.H., Cao R.** (2015), *Micromechanism of cleavage fracture of metals*, Elsevier.
7. **Dobrzanski L.A.** (1999), *Materials science lexicon, basic settlement of Polish, foreign and international standard, Metals*, Polymers, Ceramics, Composites, Verlag Dshofer (in Polish).
8. **Dymski S., Gietka T., Stawicka Z., Kaczmarek M.** (2005), Testing of influence low temperaturę on cracking a welded joint, *Welded Review*, 4, 99–106 (in Polish).
9. **Dzioba I., Neimitz A.** (2007), Application of the standard options of the FITNET Procedure to the structural integrity assessment of welded specimens containing cracks, *International Journal of Pressure Vessels and Piping*, 84(8), 475–486.
10. **Dzioba I., Skrzypczyk A.** (2006), Properties and microstructure of MAG but-welded joints of 18G2A steel, *Welded Review*, 9–10, 32–35 (in Polish).
11. **Dzioba I., Neimitz A., Gajewski M.** (2010), Studies of fracture process in Cr-Mo-V ferritic steel with various types of microstructure, *International Journal of Pressure Vessels and Piping,* 87, 575–586.
12. **ESIS P2-92**. (1992), Procedure for Determining the Fracture Behaviour of Materials, Appendix 4. A4.1–A4.6.
13. **FITNET.** Fitness for service. Fracture fatigue creep corrosion (2008), In: Kocak M., Webster S., Janosch J.J., Ainsworth R.A., Koers R., editor. GKSS Research Centre, Geesthacht.
14. **Guo W.L.** (1995), Elastoplastic three dimensional crack border field – III. Fracture parameters, *Engineering Fracture Mechanics*, 51, 51–71.
15. **JSME S 001-81**. (1981), Standard Method of Test for Elastic-Plastic Fracture Toughness J_{IC}. JSME Standard, Japan.
16. **Kocanda S.** (1978), Fatigue Destruction of Metals, WNT (in Polish).

17. **McClintok F.A**. (1968), Criterion for ductile fracture by growth of holes, *Journal of Applied Mechanics*, 35, 363-371.
18. **Neimitz A., Galkiewicz J.** (2010), Aproximation of stress-strain curve in front of a crack in a non-linear material, *International Journal of Fracture*, 161(1), 227–232.
19. **Neimitz A., Graba M., Galkiewicz J.** (2007), An alternative formulation of Ritchie-Knott-Rice local fracture criterion, *Engineering Fracture Mechanics*, 74, 1308–1322.
20. **PN-EN 10025-2:2007:** Hot Rolled Products of Structural Steels. Part 2. Technical Delivery Conditions for Non-alloy Structural Steels (in Polish).
21. **PN-EN ISO 6892-1:2010**. Metallic Materials. Tensile Testing. Part 1. Method of Test at Room Temperature (in Polish).
22. **Rice J.R., Tacey, D.M**. (1969), On the ductile enlargement of voids in triaxial stress fields, *Journal of the Mechanics and Physics of Solids*, 17, 201–217.
23. **Ritchie R.O., Knott J.F., Rice J.R**. (1973), On the relationship between critical tensile stress and fracture toughness in mild steel, *Journal of the Mechanics and Physics of Solids*, 21, 395–410.
24. **Seweryn A**. (1993), Brittle fracture criterion for structures with sharp notches, *Engineering Fracture Mechanics*, 45, 673–681.
25. **Seweryn A., Mroz Z**. (1995), A non-local stress and strain energy release rate mixed mode fracture initiation and propagation criteria. *Engineering Fracture Mechanics*, 51, 955–973.
26. **Shih C.F.** (1981), Relationship between the J-integral and crack opening displacement for stationary and extending crack, *Journal of the Mechanics and Physics of Solids*, 29, 305–329.
27. **Zu-Han L., Chang-Xiang M** (1985), Comparison of several methods of J_{IC} determination, Engineering Fracture Mechanics, 22, 1117–1119.